The Rab7-Epg5 and Rab39-ema modules cooperatively position autophagosomes for efficient lysosomal fusions

Attila Boda[1,2] (ORCID: 0000-0003-1811-8595), Villő Balázs[1,2], Anikó Nagy[1,2] (ORCID: 0000-0002-0979-1617), Dávid Hargitai[1,2] (ORCID: 0000-0002-6064-9966), Mónika Lippai[1,2] (ORCID: 0000-0002-7307-4233), Zsófia Simon-Vecsei[1,2] (ORCID: 0000-0001-7909-4895), Márton Molnár[1,2], Fanni Fürstenhoffer[1,2], Gábor Juhász[1,3] (ORCID: 0000-0001-8548-8874), Péter Lőrincz[1,2,✉] (ORCID: 0000-0001-7374-667X)

[1] Department of Anatomy, Cell and Developmental Biology, Eötvös Loránd University, Budapest, Hungary
[2] HAS-ELTE Momentum Vesicular Transport Research Group, Hungarian Academy of Sciences & ELTE Eötvös Loránd University, Budapest, Hungary
[3] Lysosomal Degradation Research Group, Institute of Genetics, HUN-REN BRC Szeged, Szeged, Hungary

✉ Corresponding author: **Péter Lőrincz**
Tel: +36 1 372 2500 / 8636; e-mail: peter.lorincz@ttk.elte.hu

Keywords: autophagosome, dynein, microtubular transport, ncMTOC, fusion, lysosome

Abstract

Macroautophagy, a major self-degradation pathway in eukaryotic cells, utilizes autophagosomes to transport self-material to lysosomes for degradation. While microtubular transport is crucial for the proper function of autophagy, the exact roles of factors responsible for positioning autophagosomes remain incompletely understood. In this study, we performed a loss-of-function genetic screen targeting genes potentially involved in microtubular motility. A genetic background that blocks autophagosome-lysosome fusions was used to accurately analyze autophagosome positioning. We discovered that pre-fusion autophagosomes move towards the non-centrosomal microtubule organizing center (ncMTOC) in *Drosophila* fat cells, which requires a dynein-dynactin complex. This process is regulated by the small GTPases Rab7 and Rab39 together with their adaptors: Epg5 and ema, respectively. The dynein-dependent movement of vesicles toward the nucleus/ncMTOC is essential for efficient autophagosomal fusions with lysosomes and subsequent degradation. Remarkably, altering the balance of kinesin and dynein motors changes the direction of autophagosome movement, indicating a competitive relationship where normally dynein-mediated transport prevails. Since pre-fusion lysosomes were positioned similarly to autophagosomes, it indicates that pre-fusion autophagosomes and lysosomes converge at the ncMTOC, which increases the efficiency of vesicle fusions.

Introduction

Macroautophagy is an essential self-degradation pathway in eukaryotic cells, during which double-membrane-bound autophagosomes transport materials to lysosomes for degradation (Parzych & Klionsky, 2014). Defects in autophagy are associated with multiple pathologies, prompting extensive study of its molecular players over the past decades (Lei & Klionsky, 2021). During macroautophagy, a double-membrane structure called an autophagosome is formed in an *atg* gene-dependent manner. This autophagosome then fuses with a lysosome or late endosome in a process dependent on the small GTPases Rab7, Rab2, and Arl8, the HOPS tethering complex, and the SNARE proteins Syntaxin17, Ubisnap/SNAP29, and Vamp7 (Lőrincz & Juhász, 2020).

Autophagosomes are suggested to form at random locations within the cytoplasm and are subsequently transported toward the cell center (Jahreiss et al., 2008; Kimura et al., 2008). Establishing proper proximity between autophagosomes and lysosomes is essential for their ability to fuse. The microtubular network and associated motor proteins are crucial for most vesicular transport. Thus, the involvement of the microtubular system has been suggested in various aspects of autophagosome dynamics, including biogenesis, transport, amphisome formation (Köchl et al., 2006), and autophagic clearance (Ravikumar et al., 2005). It is proposed that while microtubules are necessary for the maturation of autophagosomes, their fusion capacity is independent of microtubules (Fass et al., 2006). Nevertheless, dynein-regulated autophagosomal motility appears indispensable for efficient lysosomal fusion (Jahreiss et al., 2008; Kimura et al., 2008). How autophagosomes gain the ability to move along microtubules remains unclear. It is suggested that autophagic vesicles acquire dyneins by endosomal fusion (Cheng et al., 2015); however, autophagosomes still appear to be motile upon Syx17 loss (Neisch et al., 2017).

Most of our knowledge about autophagosome positioning and movement comes from studies on neurons, where autophagosomes form in the terminal part of axons and then travel toward the soma by dynein-dynactin-regulated bulk retrograde transport during basal autophagy (Ikenaka et al., 2013; Lee et al., 2011; Maday et al., 2012; Wang et al., 2015). During their route, they fuse with endosomes and lysosomes, resulting in gradual acidification and the acquisition of lysosomal markers (Hill & Colón-Ramos, 2020; Lee et al., 2011). Degradation takes place in the cell body (Maday et al., 2012). Inhibited retrograde transport leads to neurodegeneration and defective removal of synaptic autophagosomes (Fu et al., 2014; Lee et al., 2011; Ravikumar et al., 2005), highlighting the importance of axonal transport in the acidification and degradation processes.

Autophagosomes are suggested to use both dyneins and kinesins in neuronal cells. Initially, they exhibit bidirectional motility at the axon tip, later shifting to dynein-regulated retrograde transport directed toward the soma, where the already mature autolysosomes again show bidirectional motility (Maday et al., 2012). Various scaffolding proteins have been found to regulate autophagosome transport, including CKA as part of the STRIPAK complex (Neisch et al., 2017), JIP1, JIP3, and JIP4 (Cason et al., 2021; Cason & Holzbaur, 2023; Fu et al., 2014), as well as Huntingtin and HAP1 (Cason et al., 2021; Hill & Colón-Ramos, 2020; Wong & Holzbaur, 2014). It is important to note that before autophagosome closure, phagophores are not able to be transported (Fass et al., 2006).

However, most of our knowledge about autophagosome motility comes from experimental methods and tools that do not distinguish between non-acidic autophagosomes and autophagic structures that have already undergone some endolysosomal fusion and acidification. For example, several studies used reporters such as LC3 fused to red fluorescent proteins, which also label post-fusion autolysosomes. Consequently, autophagic organelles that have acidified are sometimes still considered autophagosomes, when in fact they could be autolysosomes.

We and our colleagues have previously identified and characterized several key players in autophagosome-lysosome fusion in starved *Drosophila* fat cells (Boda et al., 2019; Hegedus

et al., 2016; Lorincz et al., 2017; Takáts et al., 2013; Takáts et al., 2014). During these studies, we observed an intriguing phenomenon: despite being generated at random positions in the cytosol, autophagosomes accumulated around the nucleus when either the HOPS tethering complex or the SNARE fusion machinery was inhibited (Boda et al., 2019; Lőrincz et al., 2019; Takáts et al., 2013; Takáts et al., 2014).

This observation led us to employ a novel and unique approach by examining autophagosome positioning in cells where autophagosome-lysosome fusion was inhibited using HOPS RNAi. This method allowed us to exclude the confounding effects of ongoing vesicle fusions, which could otherwise obscure the accurate determination of the roles of different factors in vesicle positioning. These cells were utilized in an RNA interference screen to identify and characterize the molecular participants involved in autophagosome positioning. Our work represents the first comprehensive description of the transport machinery involved in pre-fusion autophagosomes and its significance during autolysosome formation.

Results

We began our investigations by performing an RNA interference screen to identify genes potentially involved in the microtubular positioning of autophagosomes, including MT proteins and motors (such as dynein, dynactin, and kinesin subunits), Rab small GTPases, and their effectors (for the complete list of tested genes and results, see **Supplementary File 1** and **Supplementary Table 1**). We used larval fat cells of the fruit fly (*Drosophila melanogaster*) as a model system, in which bulk macroautophagy was induced by starvation (Scott et al., 2004). The fat tissue contained GFP-positive mosaic cells, in which we silenced the gene of interest together with the Vps16A central subunit of the HOPS complex. This RNAi effectively impairs autophagosomal fusion, leading to the accumulation of autophagosomes (Takáts et al., 2014). Fat cells also expressed an mCherry-Atg8a reporter driven by a *UAS*-independent fat body-specific *R4* promoter. This reporter marks both autophagosomes and autolysosomes in control cells, due to the stability of mCherry in acidic environments (**Fig. 1A**). However, in *vps16a* RNAi cells, which also expressed a control (*luciferase*) RNAi, we observed the accumulation of small mCherry-Atg8a puncta—representing autophagosomes—in the perinuclear region (**Fig. 1A, B, F**), consistent with previous observations (Takáts et al., 2014).

Similar observations were made by endogenous immunostaining against Atg8a (**Figure 1—figure supplement 1A, H**), Rab7 (**Figure 1—figure supplement 1B, I**), and Arl8 (**Figure 1—figure supplement 1C, J**). Endogenous Atg8a immunostaining is specific for autophagosomes (Lőrincz et al., 2017), Rab7 antibody labels late endosomes, lysosomes, and autophagosomes (Hegedus et al., 2016), while Arl8 is a lysosome-specific small GTPase responsible for lysosomal motility and autophagosome-lysosome fusion (Bagshaw et al., 2006; Boda et al., 2019; Hofmann & Munro, 2006). Our results thus indicate that cells with impaired autophagosome-lysosome fusion accumulate not only pre-fusion autophagosomes but also pre-fusion lysosomes or late endosomes around their nuclei. Although Atg8a signal intensity detected by immunohistochemistry is higher in fusion-incompetent cells than in adjacent control cells due to the accumulation of non-degraded Atg8a (**Figure 1—figure supplement 1A**), the signal of the mCherry-Atg8a reporter appears slightly weaker in *vps16a* RNAi cells compared to controls (**Fig. 1B**). This is because the reporter is highly stable and resistant to the acidic environment in autolysosomes (Lőrincz et al., 2017). To confirm that our mCherry-Atg8a reporter labels structures of autophagic origin, we co-expressed an *atg8a* RNAi with *vps16a* RNAi, which effectively removed the signal of mCherry-Atg8a from the mosaic cells (**Figure 1—figure supplement 1D, K**), confirming that this reporter does not label non-autophagic vacuoles in these cells. Furthermore, the mCherry-Atg8a signal was almost completely absent in *atg1*; *vps16a* double RNAi cells (**Figure 1—figure supplement 1E, K**), indicating that this reporter is transported to autolysosomes via autophagosomes. To exclude the possibility that the perinuclear accumulation of autophagosomes and unfused lysosomes is due to the overall disorganization of organelles in Vps16A-depleted cells, we immunostained the cells against Gmap, which revealed that the positions of the Golgi apparatuses remained similar to control upon Vps16A silencing. Additionally, the fluorescent signal of Gmap was increased in Vps16A-depleted cells, which is consistent with the fact that the Golgi apparatus is a substrate of golgiphagy in flies (Rahman et al., 2022) (**Fig. 1C, G, H**).

The transport of autophagosomes is microtubule-dependent and minus-end directed

As microtubule (MT)-associated autophagosome transport has been suggested to be more prominent compared to the actomyosin network (Lőrincz & Juhász, 2020), we first silenced the microtubule subunits α- and β-tubulin in *vps16a* RNAi cells to clarify whether the perinuclear localization of autophagosomes is indeed established by the MT network. As expected, knockdown of tubulins diminished the perinuclear localization of autophagosomes and led to their scattering in the cytoplasm (**Fig. 1D, E, I**). Larval fat body cells have been shown to possess a perinuclear, non-centrosomal MTOC (ncMTOC) (Zheng et al., 2020).

This ncMTOC is stabilized by the Spectraplakin Short stop (Shot), and its depletion translocates the perinuclear ncMTOC to an ectopic, cytosolic location (Sun et al., 2019; Zheng et al., 2020). Therefore, we hypothesized that autophagosomes travel towards this MTOC in starved fat cells, and it is the position of the ncMTOC, rather than the nucleus, that determines their direction. Accordingly, autophagosomes accumulated in a central cytosolic region rather than around the nucleus in *shot*, *vps16a* double RNAi cells (**Fig. 1J, K, Figure 1—figure supplement 1F, G**).

To further confirm that autophagosomes indeed travel towards the ncMTOC, we expressed the MT minus-end reporter Khc-nod-LacZ (a hybrid recombinant kinesin) (Clark et al., 1997) in *vps16a* RNAi cells. Immunolabeling of Atg8a-marked autophagosomes revealed their close proximity to the reporter, which effectively labeled the perinuclear MT network (**Fig. 1L**). Additionally, we performed ultrastructural analysis to further support our findings. Compared to the mostly perinuclear distribution of autophagosomes in Vps16A single knockdown cells (**Fig. 1M**), s*hot, vps16a* double RNAi resulted in the concentration of autophagosomes in large groups adjacent to the nucleus, consistent with our fluorescent data (**Fig. 1N**). Moreover, the groups of Atg8a positive autophagic structures observed upon Shot depletion accumulate around a Khc-nod-LacZ positive region, independently of Vps16A (**Fig. 1O-S**). Taken together, our results indicate that autophagosomes move along the MT network oriented towards the MT minus-end to their final destination near the ncMTOC.

A cytoplasmic dynein-dynactin complex transports autophagosomes

Next, we turned to microtubular motor complex subunits. Dynein complexes consist of motor domain-containing heavy chains (HC), intermediate chains (IC), light intermediate chains (LIC), and light chains (LC), and their functions are regulated by dynactin complexes (Canty et al., 2021; Vaughan & Vallee, 1995). The fruit fly genome contains two genes encoding HCs and LICs, one single IC gene, and several genes encoding LCs. These can form several cytoplasmic dynein complexes; our goal was to find the one(s) responsible for autophagosome transport. Upon silencing Dynein heavy chain 64C (Dhc64C, a HC subunit), short wing (sw, an IC subunit), Dynein light intermediate chain (Dlic, a LIC subunit), and roadblock (robl, a LC subunit) in *vps16a*-silenced cells, we observed an interesting phenomenon: autophagosomes accumulated in the cell periphery, under the plasma membrane, and not around the nucleus (**Fig. 2A-D, K, Figure 2—figure supplement 1A, R**). Similar to the dynein hits, the silencing of DCTN1-p150 (Dynactin 1, p150Glued homolog), DCTN2-p50, and DCTN4-p62 also resulted in the redistribution of autophagosomes to the cell periphery (**Fig. 2E-G, K, Figure 2—figure supplement 1B, C, R**). Our mCherry-Atg8a data were strengthened by endogenous Atg8a and Rab7 immunostainings (**Figure 2—figure supplement 1D-I, T, U**), as Atg8a and Rab7 positive puncta also redistributed to the cell periphery upon co-silencing Vps16A with our dynein or dynactin hits.

We also overexpressed a dominant-negative form of DCTN1-p150, as well as a wild-type DCTN2-p50/dynamitin, which is described to cause dominant-negative effects when overexpressed (Zheng et al., 2020). These reproduced the phenotypes of dynein or dynactin loss, further strengthening our data (**Figure 2—figure supplement 1J, K, R**). In turn, silencing other dynein or dynactin genes did not cause similar effects; these cells were either control-like (*vps16a* single RNAi) (**Supplementary File 1, Supplementary Table 1**) or, in two cases, a mild scattering of autophagosomes were observed (Dlc90F, an LC subunit, and capping protein alpha, cpa, a dynactin subunit) (**Figure 2—figure supplement 1L, M, S, Supplementary File 1, Supplementary Table 1**).

Our results thus suggest that autophagosomes are mainly transported by a cytosolic dynein complex composed of Dhc64 (HC), sw (IC), Dlic (LIC), and roadblock (LC), regulated by a DCTN1-2-4 containing dynactin complex (**Fig. 2J**). However, we cannot exclude the possibility that other dynein and dynactin subunits also contribute to autophagosome motility as this would require confirmation that the RNAi transgenes yielding negative results were

indeed efficient in generating loss-of-function of their target genes. Importantly, the peripheral accumulation of autophagosomes upon the lack of dynein-regulated movement suggests that kinesins can take their place and carry autophagosomes to the positive end of microtubules.

We continued screening by silencing dynein activators and regulators. These proteins, including the Bicaudal-D, Hook, and Ninein families in mammals, are responsible for enhancing processive motility and recruiting cargo to the dynein-dynactin complex (Olenick & Holzbaur, 2019; Redwine et al., 2017). We found that the silencing of a candidate activator, Girdin (Redwine et al., 2017), in a *vps16a* RNAi background led to the dispersal of autophagosomes (**Figure 2—figure supplement 1N, V**), similarly to the loss of Lis-1, a well-studied and essential regulator of dynein motor function (Dix et al., 2013; Siller et al., 2005; Sitaram et al., 2012; Swan et al., 1999) (**Figure 2—figure supplement 1O, V**). This can be explained by the fact that some dynein function is still present without Girdin and Lis-1, and their loss does not completely abolish dynein activity.

Therefore, next our screen focused on kinesin motors. Importantly, none of the kinesin knockdowns inhibited or significantly enhanced the perinuclear positioning of autophagosomes in *vps16a*-depleted cells (Khc and Klc as examples are shown, **Fig. 2H, I, K, Figure 2—figure supplement 1P, Q, T, Supplementary File 1, Supplementary Table 1**). These results suggest that cells predominantly use the dynein complex to transport autophagosomes, rather than kinesins.

A proper dynein/kinesin ratio determines the direction of autophagosome positioning

Since dynein loss leads to the peripheral relocation of autophagosomes, we hypothesized that in this case, kinesins take over the role of transporting autophagosomes, preferring the opposite direction. To examine this possibility, we overexpressed two kinesin motors (Klp67A, Klp98A) in *vps16a* RNAi cells. Strikingly, both resulted in the scattering of autophagosomes, and in some cases, caused the peripheral accumulation of mCherry-Atg8a puncta, resembling dynein loss (**Fig. 3A, B, F**). Moreover, autophagosomes scattered upon co-silencing a dynactin and a kinesin in *vps16a* RNAi cells (**Fig. 3C, F**). This suggests that without MT motors, autophagosomes are unable to move properly.

To further examine the relationship between dyneins and kinesins, we expressed the recombinant kinesin Khc-nod-LacZ in *vps16a* single and dynactin, *vps16a* double RNAi cells. This recombinant kinesin contains the cargo domain of Khc but moves towards the MT minus-end, similar to dyneins. Interestingly, overexpression of Khc-nod-LacZ in *vps16a* single RNAi cells appeared to influence the assembly and/or function of the ncMTOC, as the nuclear envelope was only partly surrounded by autophagosomes, but their distribution remained perinuclear (**Fig. 3D, F**). Strikingly, when we overexpressed this recombinant kinesin in dynactin, Vps16A double knockdown cells, autophagosomes became dispersed (**Fig. 3E, F**), and no longer accumulated at the periphery as seen in *dynactin1-p150*, *vps16a* double RNAi cells. Since kinesins do not require the activity of dynactins, this suggests that this recombinant kinesin could partially rescue the dynein/dynactin function loss and take over the role of the missing minus-end motors, further supporting that a proper dynein/kinesin ratio determines the direction of autophagosome positioning.

Since peripheral autophagosome accumulation upon loss of dyneins and dynactins tended to occur on the side of marginal fat body cells facing the body cavity and in contact with the blood (**Fig. 2A-G**), we asked whether kinesins also follow a similar distribution pattern. To examine this, we performed anti-HA immunostaining on HA-tagged Klp98A-overexpressing cells and found that this reporter is indeed enriched at the fat body margin (**Fig. 3G, H**), supporting the hypothesis that the autophagosome redistribution upon loss of minus end transport is kinesin-dependent.

Rab7 and Rab39 and their effectors Epg5 and ema are required for bidirectional autophagosome transport

Rab small GTPases regulate vesicle transport and fusion by recruiting different effectors in their active, GTP-bound form (Stenmark, 2009). Therefore, we screened all the Rab small GTPases. In Rab7, or subunits of its guanine nucleotide exchange factor complex (Mon1-Ccz1) and its interactor Epg5 (Gillingham et al., 2014) knockdown cells with simultaneous Vps16A silencing, we could no longer observe the perinuclear accumulation of autophagosomes; they were scattered throughout the cytoplasm (**Fig. 4A-D, J**). Other hits were Rab39 and its interactor ema (Gillingham et al., 2014), both suggested to be involved in the regulation of lysosomal degradation (Kim et al., 2012; Kim et al., 2010; Lakatos et al., 2021; Zhang et al., 2023). Their phenotype was very similar (**Fig. 4E, F, J, Figure 4—figure supplement 1A, G**) to the loss of Rab7 and Epg5.

Importantly, no other interaction partners of Rab7 and Rab39 appeared to be required for autophagosome transport (**Supplementary File 1, Supplementary Table 1**; examples shown in **Fig. 4G, H, J**), suggesting that mainly the Rab7-Epg5 and Rab39-ema interactions are required for the bidirectional motility of autophagosomes (**Fig. 4I**). Our results were also strengthened by immunolabelings of Atg8a and Rab7 (**Fig. 5A, B, E, F, Figure 4—figure supplement 1B-F, H, I**). Importantly, autophagosomes were still dispersed in *epg5*, *vps16a* double RNAi cells, even if we overexpressed a YFP-Rab7 transgene, suggesting that Rab7 indeed regulates autophagosome positioning via Epg5 (**Fig. 5C, G**). Interestingly, Arl8 immunolabeling revealed that Epg5 loss does not influence the perinuclear positioning of non-fused lysosomes (**Fig. 5D, H**), suggesting that it exerts its function on autophagosomes.

Therefore, we further analyzed Epg5 functions. We first generated an *Epg5-9xHA* transgene driven by the *epg5* genomic promoter and expressed this reporter in *Drosophila* S2R+ cells. We found that this reporter colocalizes with both endogenous Rab7 and Atg8a (**Fig. 5I, J**). Moreover, we observed Atg8a positive structures that colocalized with Epg5-9xHA, but not with Lamp1-3xmCherry, as well as structures that were triple positive (**Fig. 5K**), indicating that Epg5 is present on both autophagosomes and autolysosomes. Epg5 has been suggested as a Rab7 effector both in fly (Gillingham et al., 2014) and in mammalian cells (Wang et al., 2016), which we could confirm as Epg5-9xHA coprecipitates with Rab7-FLAG in cultured fly cells (**Fig. 5L**). Moreover, Epg5-9xHA also coprecipitates with the endogenous dynein motor Dhc64C (**Fig. 5M**), supporting the idea that Rab7 via Epg5 is required for dynein-dependent autophagosome transport. Taking into consideration that Epg5 was found to regulate the positioning of autophagosomes but not lysosomes, we utilized garland nephrocytes to study its effect on endolysosome maturation. Nephrocytes maintain a constant rate of endocytosis, making them ideal tools to study the endolysosomal system (Lőrincz et al., 2016). We have previously shown that inhibited late endosome to lysosome maturation leads to the enlargement of the late endosomal compartment (Boda et al., 2019; Hargitai et al., 2025; Lőrincz et al., 2019; Lőrincz et al., 2016; Lorincz et al., 2017). However, we found that neither the Rab7 or FYVE-GFP positive endosomal nor the Lamp1 positive lysosomal compartment changed upon the expression of *epg5* RNAi in nephrocytes (**Figure 5—figure supplement 1A-G**). This was strengthened by ultrastructural analyses, which showed no obvious changes in the morphology of the endolysosomal compartment in *epg5* RNAi nephrocytes (**Figure 5—figure supplement 1H, I**). These results suggest that in flies, Epg5 functions primarily in the autophagic pathway, independently from the endosomal system.

Knockdown of other small GTPases that play essential roles in the lysosomal system, such as Rab2 (Lorincz et al., 2017), Rab5 (Poteryaev et al., 2010), Rab14 (Mauvezin et al., 2016), or Arl8 (Boda et al., 2019), did not change the perinuclear pattern of mCherry-Atg8a positive autophagosomes in *vps16a* RNAi cells (**Figure 4—figure supplement 2A-D, G**). Notably, silencing the recycling endosomal Rab11 resulted in the scattering of mCherry-Atg8a puncta and the exceptionally strong accumulation of autophagosomes revealed by endogenous Atg8a staining (**Figure 4—figure supplement 2E-H**). Rab11 has been shown to be involved in autophagosome maturation in flies (Szatmári et al., 2014), but neither Rab11 interactors resulted in any change in the perinuclear autophagosome distribution (**Supplementary File**

1, Supplementary Table 1), suggesting that the effects of Rab11 may be indirect, compared to our Rab7 and Rab39 hits.

Next, we analyzed the effect and localization of overexpressed autophagosomal and endolysosomal Rabs in *vps16a* RNAi cells. Neither the wild type nor the constitutively active forms of the overexpressed Rabs changed the perinuclear distribution of mCherry-Atg8a positive autophagosomes (**Figure 4—figure supplement 3A, B, D-L, N**). Importantly, overexpression of both forms of YFP-tagged Rab7 (**Figure 4—figure supplement 3A, B**) and Rab2 (**Figure 4—figure supplement 3D, E**), as well as endogenous Rab7 immunolabeling (**Figure 4—figure supplement 3C**) showed obvious autophagosomal localization. Moreover, wild type YFP-Rab39 also overlapped with the mCherry-Atg8a puncta (**Figure 4—figure supplement 3F**) in *vps16a* RNAi cells. Our results suggest that Rab2 is exclusively required for autophagosomal fusions, while Rab7 and Rab39 are also required for autophagosome movement (**Figure 4—figure supplement 3M**). The YFP-tagged wild type form of Rab14, which was described as a regulator of autophagic vesicle transport and fusion (Mauvezin et al., 2016), exhibited a punctate pattern, but did not localize to autophagosomes, suggesting that it localizes to other organelles, most likely lysosomes (**Figure 4—figure supplement 3L**). Taken together, Rab7 and Rab39, as well as their effectors, Epg5 and ema, respectively, appear to be the most important regulators responsible for microtubular autophagosome motility in both directions.

Autophagosome transport machinery functions similarly in *snap29* and *vps16a* RNAi cells

While our findings strongly suggest that pre-fusion autophagosomes exhibit default minus-end–directed motility, we could not exclude the possibility that this phenotype specifically results from loss of the HOPS complex. To address this, we aimed to generate a Drosophila line with GFP-positive mosaic fat body cells expressing RNAi against one of the SNARE proteins required for autophagosome-lysosome fusion. Syntaxin17 (Syx17), the autophagosomal SNARE (Lőrincz & Juhász, 2020; Takáts et al., 2013), appeared to be the obvious choice. However, in Syx17 knockdown nephrocytes, we observed a tethering lock that permanently anchors lysosomes and autophagosomes together (Hargitai et al., 2025), making it impossible to study autophagosome motility independently of lysosomes. Therefore, we turned to the SNARE Snap29 as an alternative and generated a Drosophila line with GFP-positive mosaic fat body cells expressing Snap29 RNAi. Like our vps16a RNAi line used in the genetic screen, these flies also expressed an mCherry-Atg8a reporter driven by a UAS-independent, fat body-specific R4 promoter. Snap29 encodes a SNARE protein essential for autophagosome–lysosome fusion (Lőrincz & Juhász, 2020; Takáts et al., 2013).

We crossed this line with a control (luciferase) RNAi and with several key hits from our screen. Similar to *vps16a* RNAi, Snap29 knockdown led to perinuclear accumulation of autophagosomes (**Fig. 6A, I**). In *snap29* RNAi cells, *shot* and *dhc64c* RNAi redistributed autophagosomes to an ectopic MTOC or to the periphery, respectively (**Fig. 6B, C, I**). Knockdown of the kinesin Khc did not affect the perinuclear accumulation of autophagosomes in *snap29* RNAi cells (**Fig. 6D, I**), while RNAi targeting the small GTPases Rab7, Rab39, or their adaptors (Epg5 or ema) caused autophagosomes to become dispersed throughout the cytosol **(Fig. 6E–I)**.

These results indicate that the redistribution of autophagosomes toward the microtubule minus-end is a general consequence of impaired fusion, and further suggest that the autophagosome transport machinery functions independently of Vps16A and the HOPS complex.

The transport of pre-fusion lysosomes is also minus-end directed

Given that *vps16a* RNAi led to the perinuclear distribution of immature lysosomes (**Figure 1—figure supplement 1C**) similar to autophagosomes, we hypothesized that pre-fusion autophagosomes and lysosomes travel in the same orientation, potentially sharing the same

transport machinery. Thus, we stained lysosomes and co-expressed *vps16a* RNAi along with RNAi targeting our hits from the autophagosome positioning screen (**Fig. 7**). Importantly, in most cases, we observed similar phenotypes with Lamp1 staining as we did with Atg8a: spectraplakin (*shot*) RNAi redistributed Lamp1 organelles to an ectopic ncMTOC, dynein inhibition redistributed lysosomes to the periphery, *rab7*, *rab39*, and *ema* RNAi-s resulted in the scattering of lysosomes across the cytosol, and kinesin depletion had no effect on the perinuclear accumulation of lysosomes (**Fig. 7**).

However, there were two important exceptions: Epg5 knockdown left lysosomes perinuclear (**Fig. 7C, L**), suggesting that it is indeed an autophagosomal adaptor. The other exception was *rab2* RNAi, which had no significant effect on autophagosome transport but resulted in dispersed, and sometimes even peripheral, lysosomal distribution in Vps16A-depleted cells (**Fig. 7I, L**). This result suggests that Rab2 is a potential regulator of minus-end directed transport of lysosomes and that pre-fusion organelles (autophagosomes and lysosomes) predominantly travel towards the minus-end of the MTs and share the main molecular components.

Minus-end directed autophagosome and lysosome transport is required for autophagosome-lysosome fusion

We hypothesized that concentrating pre-fusion autophagosomes and lysosomes at the perinuclear region increases the probability of their fusion, thereby promoting autolysosome formation. To test this, we used similar reporters and reagents as above but did not silence Vps16A in the examined cells to allow autophagosome-lysosome fusions. First, we analyzed Epg5 knockdown, which has been described to inhibit autolysosome maturation based on GFP-Atg8a (Byrne et al., 2016). In line with this, 3xmCherry-Atg8a positive autolysosomes were significantly smaller than in control cells, without any obvious change in their distribution (**Fig. 8A, B, E, F**). Since 3xmCherry-Atg8a is transported to the lysosomes via autophagosome-lysosome fusion, and it retains its fluorescence in the lysosomal environment, it can be used to monitor autolysosome maturation. Although we cannot determine the number of lysosomes that fuse with each autophagosome, the overall size of 3xmCherry-Atg8a positive structures correlates with autolysosome maturation efficiency (Lőrincz et al., 2017). Accordingly, the large Rab7 and Arl8 positive autolysosomes were almost completely absent from Epg5 silenced cells, as revealed by immunostainings (**Fig. 8C, D, G, H**), with only small autolysosomes present.

Silencing of the dynein and dynactin hits: Dhc64C, sw, Dlic, and robl, as well as DCTN1-p150, resulted in the redistribution of 3xmCherry-Atg8a positive autolysosomes to the periphery and their size became significantly smaller (**Fig. 9A-E, I, K**), suggesting that loss of minus-end directed transport leads to autolysosome maturation defects. In contrast, *khc* and *klc* RNAi caused the perinuclear accumulation of autolysosomes, which appeared larger than those in the controls, suggesting a trend, although this difference did not reach statistical significance (**Fig. 9F, G, J, L**).

In accordance with its suggested role in autophagosome-lysosome fusion, silencing of Rab7 resulted in significantly smaller and mostly dispersed autolysosomes (**Figure 9—figure supplement 1A, D, E**) (Hegedus et al., 2016; Lorincz et al., 2017). Rab39 knockdown, however, led to mostly peripheral autolysosomes, which were not different in size from those in the control cells (**Figure 9—figure supplement 1B, D, E**), but the localization of the mCherry-Atg8a positive autolysosomes suggests that Rab39 is also required for minus-end directed movement of mature lysosomes. Surprisingly, loss of ema did not influence the size and distribution of autolysosomes (**Figure 9—figure supplement 1C-E**).

Our most important finding came when we silenced the spectraplakin Shot, which caused the accumulation of autolysosomes in the ectopic cytosolic MTOC (**Fig. 9H**). Notably, their size significantly increased (**Fig. 9H, L**). This can be explained by the fact that the volume surrounding the ectopic ncMTOC in Shot-depleted cells is smaller than the volume around

the nuclei, leading to an increased fusion rate in these cells. Taken together, these results demonstrate that minus-end transport is crucial for proper autolysosome maturation.

The observation that dispersing autophagosomes and lysosomes under the plasma membrane in dynein/dynactin-silenced cells leads to insufficient autolysosome maturation, while concentrating autophagosomes and lysosomes to an ectopic ncMTOC in *shot* RNAi results in the enlargement of lysosomes, indicates that the autophagosome-lysosome fusion rate depends on the volume of cytoplasm in which these organelles meet. Several studies have suggested a connection between microtubular transport and the fusion of autophagosomes (Fass et al., 2006; Jahreiss et al., 2008; Kimura et al., 2008; Köchl et al., 2006).

We tested this hypothesis by analyzing the colocalization between the 3xmCherry-Atg8a reporter and the lysosomal membrane protein Lamp1, either by immunostaining or by expressing GFP-Lamp1. Their overlap represents autolysosomes, while 3xmCherry-Atg8a positive, Lamp1 negative structures are considered pre-fusion autophagosomes. Conversely, Lamp1 positive, 3xmCherry-Atg8a negative structures indicate lysosomes of non-autophagic origin. Thus, reduced colocalization indicates a fusion defect. In control cells, Lamp1 or GFP-Lamp1 overlaps with mCherry-Atg8a, indicating that these organelles are indeed autolysosomes (**Fig. 10A, H, Figure 10—figure supplement 1A, G**). In Shot-depleted cells, both signals overlapped in the ectopic ncMTOC, indicating that autophagosomes can effectively fuse with lysosomes in this region (**Fig. 10B, H, Figure 10—figure supplement 1B, G**). Accordingly, the loss of the kinesin heavy chain Khc did not alter the overlap of these markers, proving that autolysosomes could still be formed (**Fig. 10C, H, Figure 10—figure supplement 1C, G**). Importantly, the loss of the dynein motor Dhc64C, as well as the dynactin subunit DCTN1-p150, greatly reduced the overlap of signals, indicating a less effective autophagosome-lysosome fusion (**Fig. 10D, E, H, Figure 10—figure supplement 1D, G**). Since Rab7 and Epg5 have been implicated in autolysosome maturation, their depletion reduced the overlap of autophagic and lysosomal markers (Byrne et al., 2016; Hegedus et al., 2016; Wang et al., 2016) (**Fig. 10F-H, Figure 10—figure supplement 1E-G**). Although loss of minus end directed transport significantly impaired autophagosome-lysosome fusion, the degree of inhibition did not reach the level observed upon Vps16A knockdown (**Figure 10—figure supplement 1H-K**). This indicates that impaired motility alone does not directly block fusion, but rather reduces its probability. Taken together, our results suggest that the role of minus-end directed transport in fat cells is to bring pre-fusion organelles into proximity to increase the likelihood of their fusion.

Discussion

Microtubular transport of different organelles within the lysosomal system is essential for their proper function. Among the small GTPases that regulate late endosome/lysosome positioning, Rab7 (Fujiwara et al., 2016; Jordens et al., 2001; Ma et al., 2018; van der Kant et al., 2013) and Arl8 (Bagshaw et al., 2006; Boda et al., 2019; Hofmann & Munro, 2006; Marwaha et al., 2017; Rosa-Ferreira & Munro, 2011; Rosa-Ferreira et al., 2018) are well-studied. However, the positioning of autophagosomes is less understood. Autophagosome transport has been primarily studied in highly polarized neurons under basal conditions. In neuronal cells, dynein-mediated transport, regulated by several suggested adaptor molecules, has been described. However, most reporters and reagents used for studying autophagosome transport cannot differentiate between pre-fusion and post-fusion autophagic vesicles. Therefore, the regulation of non-fused autophagosome motility remains unclear. We propose that an autophagosome should not be considered as such once its lumen has started to acidify or undergo fusion, transitioning to a maturing autolysosome.

To address this issue, we established a genetic system generating mosaic cells where Vps16A, a central HOPS subunit, is silenced. Without Vps16A, cells are unable to fuse autophagosomes with lysosomes or late endosomes (Takáts et al., 2014), thus preventing

the formation of autolysosomes. This system allowed us to study autophagosome positioning without misidentifying autolysosomes as autophagosomes. Given that fat cells have perinuclear non-centrosomal MTOCs, we hypothesized that non-fused autophagosomes move in a minus-end direction, likely driven by dyneins. This hypothesis was supported by our observation that relocating the ncMTOC using *shot* RNAi also relocated autophagosomes to this region.

Loss of dyneins and dynactins not only blocked perinuclear autophagosome positioning but also redistributed them to the cell periphery, suggesting that kinesin-regulated motility becomes available for starvation-induced autophagosomes in these conditions. Importantly, we showed that not all dyneins or dynactins are required for this transport. A dedicated cytosolic dynein complex, composed of Dhc64 (a heavy chain subunit), sw (an intermediate chain subunit), Dlic (a light intermediate chain subunit), and robl (a light chain subunit), activated by a dynactin complex, is required for autophagosome transport. This is consistent with observations that autophagosomes can move bidirectionally in neurons and that purified autophagosome fractions contain both dyneins and kinesins (Maday et al., 2012). Our results also reinforce findings that microtubule inhibitors block centrosome-directed autophagosome transport in mammalian cells (Fass et al., 2006).

Taking these observations into consideration, we investigated the relationship between dyneins and kinesins in autophagosome transport. Overexpression of kinesin motors blocked minus-end transport, while autophagosomes in kinesin and dynactin double knockdown cells appeared immobile. Moreover, expressing a recombinant minus-end kinesin (Clark et al., 1997) partially rescued the peripheral relocation of autophagosomes upon dynactin silencing, indicating a competitive relationship between minus- and plus-end motors in autophagosome positioning. The possibility of plus-end transport as a secondary mechanism raises questions about its physiological role. Besides enabling bidirectional movement (Jahreiss et al., 2008; Maday et al., 2012), it is possible that autophagosomes transport kinesins to autolysosomes, similar to endosomes, which are suggested to transport dyneins to autophagic vacuoles (Cheng et al., 2015). Therefore, if kinesins are present but are downregulated on autophagosomes, the absence of dyneins could potentially release them from inhibition. Autophagic vesicles are suggested to move towards the plus-end (Mauvezin et al., 2016; Pankiv et al., 2010), and loss of various kinesins leads to autophagosome accumulation in the cell center in mammalian cells (Cardoso et al., 2009; Korolchuk et al., 2011). The plus-end transport of autophagic vesicles by the Klp98A kinesin in *Drosophila* promotes autophagosome-lysosome fusion and degradation (Mauvezin et al., 2016). However, our tests indicated that Rab14 and its interactor Klp98A likely transport autolysosomes, not autophagosomes, as evidenced by the non-autophagosomal localization of YFP-Rab14 and that their RNAi-s had no effect on autophagosome positioning in starved, HOPS-depleted cells. Since neither kinesin RNAi altered the perinuclear accumulation of autophagosomes in Vps16A-depleted cells, we propose that the default direction is towards the MTOC at the minus-ends of microtubules.

Among Rab small GTPases, we identified Rab7 and Rab39 as regulators of autophagosome positioning. Rab7, crucial for autophagosome-lysosome fusion, appears on autophagosomes (Hegedus et al., 2016). Its knockdown resulted in autophagosomes remaining randomly positioned in the cytosol, highlighting its importance in bidirectional motility. Consistent with our findings, Rab7 regulates both minus- and plus-end directed motility of lysosomes or endosomes, involving several adaptors such as Plekhm1 and FYCO1 (Fujiwara et al., 2016; Jordens et al., 2001; Ma et al., 2018; Pankiv et al., 2010; Tabata et al., 2010; van der Kant et al., 2013). However, only one Rab7 interactor, the autophagy adaptor Epg5 (Gillingham et al., 2014; Wang et al., 2016), produced a similar phenotype to Rab7 in our tests. Additionally, we demonstrated that Epg5 coprecipitates with Dhc64C, and localizes to Rab7 and Atg8a-positive vesicles in cultured fruit fly cells. As Epg5 loss did not significantly impact the endolysosomal system, it appears to function in the autophagic pathway. Epg5 interacts with Rab7 and LC3 to mediate autophagosome-lysosome fusion in fly, worm and mammalian

cells (Hori et al., 2017; Wang et al., 2016), and its mutations are linked to Vici syndrome, a severe neurodegenerative disorder in humans (Balasubramaniam et al., 2018; Byrne et al., 2016; Meneghetti et al., 2019). We thus identify a potential new role for Epg5 in autophagosome positioning.

Silencing Rab39 and its interactor ema (Gillingham et al., 2014) produced a phenotype similar to Rab7 or Epg5 loss. Rab39 regulates lysosomal function and interacts with HOPS in mammalian cells (Lakatos et al., 2021; Zhang et al., 2023). Ema promotes autophagosome biogenesis (Kim et al., 2012) and endosomal maturation through HOPS interaction (Kim et al., 2010). Our results suggest that Rab7-Epg5 and Rab39-ema interactions are both necessary for bidirectional autophagosome motility. Further studies are required to clarify their exact roles and interrelations. YFP-tagged Rab7 and Rab39 both colocalized with autophagosomes, supporting their role in motility. Rab2, Rab7, and Arl8 are known lysosomal fusion factors (Boda et al., 2019; Hegedus et al., 2016; Lorincz et al., 2017), but unlike Rab7, neither Rab2 nor Arl8 knockdown affected autophagosome positioning. Since YFP-Rab2 was also found to colocalize with autophagosomes, our results suggest that its sole role on autophagosomes is to regulate maturation. Although our RNAi screen identified a molecular machinery potentially sufficient for autophagosome transport, other small GTPases, adaptors, or motor subunits may also influence this process. Because validating the proper loss-of-function effect for every RNAi line used in the screen was impractical, we cannot exclude the possibility that some negative results were due to inefficient silencing. It is also important to note that Drosophila cells exhibit a wide variety of microtubule-organizing centers (MTOCs) during development, including both centrosomal and non-centrosomal types (Tillery et al., 2018). A key future direction will be to examine autophagosome motility in additional cell types to determine whether the same positioning machinery operates universally, or whether cell type–specific mechanisms exist.

Given the small Arl8-positive lysosomes in the perinuclear region upon Vps16A silencing, we hypothesized that pre-fusion lysosomes might exhibit similar motility to autophagosomes. This was largely confirmed, as minus-end transport of immature lysosomes depended on dyneins, Rab7, Rab39, and ema. However, Epg5 did not influence lysosome positioning, indicating that its function is likely exerted at the surface of autophagosomes. Conversely, Rab2 was identified as a regulator of minus-end directed lysosome transport. These findings suggest similar but distinct regulatory mechanisms for pre-fusion organelle transport, possibly to enhance fusion efficiency by converging them towards the cell center. Rab2's interaction with motor adaptors such as Bicaudal D (Gillingham et al., 2014) likely regulates lysosome motility.

Moreover, mature autolysosomes, but not pre-fusion ones, redistributed to the cell periphery upon Rab39 silencing, similar to dynein-depleted cells, suggesting that Rab39 exclusively regulates minus-end movement at the post-fusion level. Considering that plus-end directed lysosome motility is regulated by Arl8 (Bagshaw et al., 2006; Boda et al., 2019; Hofmann & Munro, 2006; Marwaha et al., 2017; Rosa-Ferreira & Munro, 2011; Rosa-Ferreira et al., 2018), which is dispensable for autophagosome motility, it is plausible that Rab39 promotes bidirectional transport of pre-fusion organelles, while its role post-fusion is restricted to minus-end directed motility.

An important question is why pre-fusion autophagosomes and lysosomes travel to the same destination. It is feasible to think this is because they need to fuse with each other. We found that loss of minus-end directed motility reduced autolysosome maturation; in dynein- or dynactin-depleted cells, only smaller autolysosomes were produced, and autophagosome-lysosome fusion decreased. This aligns with previous observations that dynein-regulated autophagosomal motility is indispensable for efficient lysosomal fusion (Jahreiss et al., 2008; Kimura et al., 2008). Conversely, inhibiting kinesins did not impede autophagosome-lysosome fusion, and concentrating autophagosomes and lysosomes to a smaller ectopic ncMTOC via *shot* RNAi resulted in enlarged lysosomes, allowing autophagosome-lysosome fusion to proceed.

Therefore, we propose a model in which pre-fusion organelles travel towards the MTOC in a cytosolic dynein-dependent manner regulated by small GTPases and their adaptors (Rab7-Epg5 and Rab39-ema on autophagosomes; Rab7, Rab39-ema, and Rab2 on lysosomes) to enhance fusion probability. After fusion, autolysosomes can move to the periphery in an Arl8-dependent manner and back, regulated by Rab39 (**Fig. 11**).

Materials and Methods

Fly work and RNAi based screen

We raised the fly stocks and crosses in glass vials, on standard food at 25°C. Early third instar larvae were starved for 3 hours in 20% sucrose solution. Next fat bodies were dissected in cold PBS, mounted in a 8:2 mixture of glycerol and PBS completed with Hoechst 33342 as nuclear dye (5 µg/ml) (Thermo), then imaged immediately.

For the RNAi based genetic screen, we established the *hs-Flp; Vps16A RNAi, UAS-DCR2; act<CD2<Gal4, UAS-GFPnls, r4-mCherry-Atg8a* stock, in order to generate *vps16a* RNAi expressing fat cells. This was crossed with RNAi or overexpression lines of interest.

All the screened *Drosophila* lines, as well as their sources, identifiers and phenotypes are listed in **Supplementary Table 1**. Representative images of the phenotypes of screened lines are shown in **Supplementary File 1.** The proper genotypes and the fly stocks from the screen that were used in the Figure panels are summarized in **Supplementary Table 2**.

For further experiments, we used the following mosaic cell generating stocks, with or without Vps16A RNAi.:

- *hs-Flp; Vps16A RNAi, UAS-DCR2; act<CD2<Gal4, UAS-GFPnls*,
- *hs-Flp; UAS-DCR2; act<CD2<Gal4, UAS-GFPnls*,
- *hs-Flp; 3xmCherry-Atg8a, UAS-2xEGFP; act<CD2<Gal4, UAS-DCR2*,
- *hs-Flp; 3xmCherry-Atg8a, UAS-GFP-Lamp1; act<CD2<Gal4, UAS-DCR2*.

All of these stocks were described before (Boda et al., 2019; Lorincz et al., 2017; Takáts et al., 2013). The *prospero-Gal4* driver (80572; FlyBase ID: FBst0080572) and the *UAS-GFP-myc-2xFYVE* reporter (42712; FlyBase ID: FBst0042712) used for the garland cell experiments were obtained from Bloomington Drosophila Stock Center.

Immunohistochemistry

For immunohistochemistry experiments, we dissected and fixed the samples in 4% paraformaldehyde (in PBS) for 45 min, washed them in PBS for 2×15 min, permeabilized in PBTX (0.1% Triton X-100 in PBS) for 20 min and blocked in 5% fetal bovine serum (in PBTX) for 30 min. The samples were then incubated with the primary antibodies (diluted in the blocking solution) overnight at 4°C, followed by washing in PBTX containing 4% NaCl for 15 min, washing in PBTX for 2×15 min, blocking in 5% fetal bovine serum (in PBTX) for 30 min and incubating with the secondary antibodies for 3 hours. The samples were then washed in PBTX containing 4% NaCl and 5 µg/ml Hoechst 33342 for 15 min, in PBTX for 2×15min, and in PBS for 2×15 min. All steps, except the incubation with primary antibodies, were performed at room temperature.

In case of garland immunohistochemistry and Lamp1 immunostainings of fat bodies for the 3xmCherry-Atg8a colocalization experiment, samples were dissected in a buffer containing 80 mM PIPES, 5 mM EGTA and 1 mM $MgCl_2$ (pH was adjusted to 6.8 with NaOH) and fixed in this solution containing also 3.7% formaldehyde, 0.25% glutaraldehyde and 0.2% Triton X-100, for 45 min. Following the fixation, the samples were incubated with 2 mg/ml sodium borohydride (in PBS) for 2.5 min, washed in PBS for 2×15 min (once for 10 min in case of garland cells) and permeabilized in PBTX containing ammonium chloride and glycine (both 50 mM) for 20 min. The remaining steps were the same as described above.

For immunostaining S2R+ hemocytes (*Drosophila*), cells were fixed in 4% paraformaldehyde for 20 min, washed in PBS for 15 min, permeabilized in PBTX for 10 min, and blocked in 5% fetal bovine serum (in PBTX) for 30 min. The samples were then incubated with the primary antibodies overnight at 4°C, followed by washing in PBTX containing 4% NaCl for 15 min and in PBTX for 2×10 min, and incubation with the secondary antibodies (solved in the blocking solution) for 3 h. The cells were then washed in PBTX containing 4% NaCl and 5 µg/ml Hoechst 33342 for 15 min, in PBTX for 10 min and in PBS for 15 min. In case of Atg8a immunolabeling, cells were starved in a solution containing 10 mM D(+) glucose, 0.5 mM $MgCl_2$, 4.5 mM KCl, 121 mM NaCl, 0.7 mM Na_2HPO_4, 1.5 mM NaH_2PO_4, and 15 mM $NaHCO_3$ (pH 7.4) (Aguilera-Gomez et al., 2017).

The following primary antibodies were used: rat anti-Atg8a (1:800 or in case of S2R+ cells, 1:300; (Takáts et al., 2013)); rabbit anti-β-galactosidase (1:100; Merck); goat anti-Gmap (1:1000; Developmental Studies Hybridoma Bank [DSHB]); mouse anti-Rab7 (1:10; DSHB; (Riedel et al., 2016)); rabbit anti-Arl8 (1:300; DSHB); rabbit anti-Lamp1 (1:1000; (Chaudhry et al., 2022)), rat anti-mCherry (1:300; (Takáts et al., 2014); guinea pig anti-mCherry (1:500); rabbit anti-HA (1:200; Merck); rabbit anti-HA (1:200; Proteintech) and chicken anti-GFP (1:1500; Invitrogen).

We used the following secondary antibodies: Alexa Fluor 568 goat anti-rat (1:1000); Alexa Fluor 647 donkey anti-rabbit (1:600); Alexa Fluor 568 donkey anti-goat (1:1000); Alexa Fluor 568 donkey anti-mouse (1:1000); Alexa Fluor 647 donkey anti-mouse (1:600); Alexa Fluor 568 donkey anti-rabbit (1:1000); Alexa Fluor 488 goat anti-chicken (1:1000); Alexa Fluor 488 donkey anti-rat (1:1000); Alexa Fluor 488 goat anti-rabbit (1:1000) (all Invitrogen) and DyLight 550 goat anti-guinea pig (1:600; Thermo Fisher).

Electron microscopy

For correlative ultrastructural analysis, fat bodies were dissected in a fixative containing 3.2% paraformaldehyde, 1% glutaraldehyde, 1% sucrose and 0.003 M $CaCl_2$ (in 0.1 N sodium cacodylate buffer, pH 7.4) on poly-L-lysine coated glass slides and fluorescent images were taken to help recognizing GFP and RNAi expressing cells. Then the samples were fixed in the same solution overnight at 4°C, then were post-fixed in 0.5% osmium tetroxide for 1 h, followed by half-saturated aqueous uranyl acetate for 30 min and dehydrated in a graded series of ethanol, followed by embedding into Durcupan ACM (Sigma-Aldrich) on the glass slides. RNAi cells in the embedded samples were identified in semi-thick sections stained with toluidine blue, then ultra-thin sections of 70 nm were cut, then stained with Reynold's lead citrate (8 min, RT).

Preparation of samples for ultrastructural analysis of garland nephrocytes was performed as described before (Lőrincz et al., 2016).

Images were taken by a JEOL JEM-1011 transmission electron microscope operating at 80kV, equipped with a Morada camera (Olympus) and iTEM software (Olympus).

Molecular cloning and biochemistry

Cloning:
To generate *genEpg5-9xHA*, genomic DNA from *w1118 Drosophila* strain was isolated and used as a template. The genomic region containing *Drosophila CG14299* was amplified using primers 5'-CCAAGCTTGCATGCGGCCGCATTTTCTGTGCGCGACTGTTG-3' and 5'-TAAAAGATGCGGCCGGTACCGCCTCCACCCGTGGCCATTAACTTGAATTC-3' and cloned into *pGen-9xHA* (Lőrincz et al., 2016) as a NotI-Acc65I fragment by using Gibson Assembly kit (New England BioLabs, Ipswich, MA).
To obtain N-terminally 3xFLAG-tagged Rab7, the coding region of Rab7 was amplified from Drosophila cDNA (GH03685 (DGRC Stock 7144 ; https://dgrc.bio.indiana.edu//stock/7144 ; RRID:DGRC_7144)) using primers 5'-ACAAGGCGGCCGCAGGTATGTCCGGACGTAAGAAATCC-3' and 5'-

TCTAGAGGTACCTTAGCACTGACAGTTGTCAGGA-3' and cloned into NotI-Acc65I sites of *pUAST-3xFLAG* vector (Takáts et al., 2014).

S2R+ maintenance and transfection:

The S2R+ *Drosophila* cell line (Drosophila Genomics Resource Center; Stock 150; RRID: CVCL_Z831) was maintained in Insect XPress medium (Lonza) containing 10% FBS (EuroClone) and 1% Penicillin-Streptomycin (Lonza) at 26°C. Cells were transfected with *genEpg5-9xHA* plasmid using Calcium phosphate method. DNA was diluted in 240 mM $CaCl_2$, mixed with 2x HEPES-buffered saline (50 mM HEPES, 1.5 mM Na_2HPO_4, 280 mM NaCl, pH 7.1), incubated at 25°C for 30 minutes, and added to the cells. Co-transfection with *genEpg5-9xHA* and *genLamp1-3xmCherry* (Hegedus et al., 2016) was performed using jetOPTIMUS® DNA Transfection Reagent (Polyplus). 24 hours after transfection, cells were used for immunohistochemistry or immunoprecipitation. In experiments, when cells were transfected with *pUAST-3xFLAG-Rab7* and *pGen-Epg5-9xHA* constructs, metallothionein-Gal4 plasmid was also applied. Protein expression was induced 24h after transfection with 500 µM $CuSO_4$ for overnight incubation.

Immunoprecipitation:

Cells were transfected with appropriate plasmid constructs and were collected 24 hours after transfection. They were washed with PBS and lysed on ice in lysis buffer (0.5% Triton X-100, 150 mM NaCl, 5 mM EDTA, and 50 mM Tris-HCl, pH 7.5, complete protease inhibitor cocktail (Roche)) for 20 minutes. Cell lysates were cleared by centrifugation for 10 min at 20.000 g, 4°C, followed by the addition of mouse anti-HA or anti-FLAG agarose (Sigma-Aldrich) to the supernatant. After incubation at 4°C for 2 h, beads were collected by centrifugation at 5.000 g for 2 minutes at 4°C, followed by extensive washes in wash buffer (lysis buffer without protease inhibitors) and finally boiling in Laemmli sample buffer. Samples were analyzed by Western blot using rat anti-HA (1:1000; Roche), mouse anti-FLAG (M2; 1:2000; Sigma-Aldrich) and mouse anti-Dhc (2C11-2; 1:12.5; DSHB) antibodies. It is experimentally demonstrated that the Dhc antibody recognizes a polypeptide at around 260 kDa (Baker et al., 2021).

Imaging, quantification and statistics

We obtained the fluorescent images with an AxioImager M2 microscope (Zeiss), equipped with an ApoTome2 grid confocal unit (Zeiss) and with an Orca Flash 4.0 LT sCMOS camera (Hamamatsu), using Plan-Apochromat 40×/0.95 NA Air and Plan-Apochromat 63×/1.40 NA Oil objectives (Zeiss), and Zeiss Efficient Navigation 2 software. Images from eleven consecutive focal planes (section thickness: 0.35 µm in case of the 40× objective, and 0.25 µm in case of the 63× objective) were merged into one image. In case of S2R+ cells, fluorescent images were obtained with an Olympus IX83 inverted fluorescent microscope, equipped with an Orca FusionBT CMOS camera (Hamamatsu), using a Universal Plan Extended Apochromat 60×/1.42 NA objective (Olympus), and cellSens Dimension 4.1 software (Olympus). Images were taken with full optical sectioning of the cells; the focal planes were merged into one image and deconvolution was applied. Figures were produced in Photoshop CS5 Extended (Adobe).

Fluorescent structures were quantified either using ImageJ software (National Institutes of Health) or, in case of some types of experiment, manually. The signal threshold of the fluorescent channel of interest was set by the same person during quantifying one type of experiment with ImageJ. The fat cells, S2R+ cells and garland nephrocytes were randomly selected for quantification.

Structure distributions were quantified using ImageJ. In all cases, only cells with their nuclei in the focal plane were selected to ensure that both perinuclear and peripheral regions were included in quantifications. To quantify structure distribution, we divided the fat cells into a perinuclear and a peripheral domain that were measured to be equal and calculated the area of the fluorescent signal in both domains. Then the difference of signal areas of the perinuclear and peripheral domain was divided by the signal area of the entire cell, thus obtaining a ratio that represents the distribution of structures (1 – perfectly perinuclear, 0 –

evenly dispersed, -1 – perfectly peripheral). In case of distribution of non-colocalizing 3xmCherry-Atg8a or GFP-Lamp1 positive structures, overlapping dots were removed from each channel using Photoshop CS5 Extended.

The counts of cells with ectopic ncMTOC (*shot* RNAi lines) and the Rab7/Arl8 ring counts (*epg5* RNAi) were determined manually by the same person. For quantifying Gmap or mCherry-Atg8a signal intensities, mean gray values of neighboring control and RNAi cells were calculated by ImageJ. Colocalizations were quantified manually by the same person in case of fat body cells. Dot plots and Pearson's coefficients were calculated by ImageJ for evaluating colocalization in S2R+ cells.

To evaluate data from garland nephrocyte experiments, we used ImageJ to quantify fluorescent structures from unmodified single focal planes. To quantify the size of the Rab7 and FYVE-GFP positive endosomes, we measured the area of individual vesicles in the given focal plane of the cells. After setting the threshold for the fluorescent signal, we used the Watershed function of ImageJ coupled with manual segmentation when it was necessary to properly separate endosomes. For each genotype, we used 5 animals and measured the size of endosomes from a total of 10 cells. To quantify Lamp1 antibody staining signal in nephrocytes, we measured the area fraction of the cells covered by the given fluorescent signal at proper and uniform threshold settings. For each genotype, we used 5 late L3 stage animals and measured 15 cells.

Data were statistically evaluated using Prism 9.4.1 (GraphPad). The distribution of the datasets was determined using the D'Agostino & Pearson normality test. Parametric, unpaired, two-tailed t test or one-way ANOVA (with Dunnett multiple comparisons test) was used to compare two or more samples, respectively, all showing normal distribution. When comparing two or more samples that contained at least one variable showing non-Gaussian distribution, we used non-parametric Mann-Whitney test or Kruskal-Wallis test (with Dunn's multiple comparisons test), respectively. We showed the data as violin plots in the figures and represented p values as asterisks (<0.0001 ****; 0.0001-0.001 ***; 0.001-0.01 **; 0.01-0.05 *; 0.05< non-significant). Samples that are significantly different from the control are marked by green on the violin plots. All experiments were repeated on a different day, with similar results.

Funding and acknowledgments

We thank Sarolta Pálfia for technical assistance, and colleagues and stock centers mentioned in the Materials and Methods section for supporting our work by providing fly stocks and reagents.

This work has been implemented with the support provided by the Ministry of Culture and Innovation of Hungary from the National Research, Development and Innovation Fund (PD142943 to AB; FK138851 to PL; KKP129797 to GJ; New National Excellence Program: ÚNKP-23-3-I-ELTE-724 to DH, ÚNKP-23-3-I-ELTE-706 to MM; Doctoral Excellence Program: DKÖP-2023-ELTE-13 to DH), the Hungarian Academy of Sciences (LP2022-13/2022 to PL, LP2023-6 to GJ) and the Eötvös Loránd University Excellence Fund (EKA 2022/045-P101-2 to PL).

The funders had no role in designing experiments, data collection and analysis, decision to publish, or preparation of the manuscript.

Competing interests

The authors declare that no competing interests exist.

Author Contributions

AB, VB, GJ and PL contributed to the study conception and experiment design. AB, PL, GJ, DH and MM acquired funding. Fly work, preparation of samples and fluorescent microscopy were performed by AB, VB, AN, DH, ML, FF and MM. Biochemistry experiments were performed by ZS. Ultrastructural analysis was performed by PL. Quantification and statistical analysis were performed by AB, VB and DH. The manuscript was written by AB and PL with comments from all authors.

References

Aguilera-Gomez, A., Zacharogianni, M., van Oorschot, M. M., Genau, H., Grond, R., Veenendaal, T.,…Rabouille, C. (2017). Phospho-Rasputin Stabilization by Sec16 Is Required for Stress Granule Formation upon Amino Acid Starvation. *Cell Rep*, *20*(4), 935-948. https://doi.org/10.1016/j.celrep.2017.06.042

Bagshaw, R. D., Callahan, J. W., & Mahuran, D. J. (2006). The Arf-family protein, Arl8b, is involved in the spatial distribution of lysosomes. *Biochem Biophys Res Commun*, *344*(4), 1186-1191. https://doi.org/10.1016/j.bbrc.2006.03.221

Baker, F. C., Neiswender, H., Veeranan-Karmegam, R., & Gonsalvez, G. B. (2021). In vivo proximity biotin ligation identifies the interactome of Egalitarian, a Dynein cargo adaptor. *Development*, *148*(22). https://doi.org/10.1242/dev.199935

Balasubramaniam, S., Riley, L. G., Vasudevan, A., Cowley, M. J., Gayevskiy, V., Sue, C. M.,…Christodoulou, J. (2018). EPG5-Related Vici Syndrome: A Primary Defect of Autophagic Regulation with an Emerging Phenotype Overlapping with Mitochondrial Disorders. *JIMD Rep*, *42*, 19-29. https://doi.org/10.1007/8904_2017_71

Boda, A., Lőrincz, P., Takáts, S., Csizmadia, T., Tóth, S., Kovács, A. L., & Juhász, G. (2019). Drosophila Arl8 is a general positive regulator of lysosomal fusion events. *Biochim Biophys Acta Mol Cell Res*, *1866*(4), 533-544. https://doi.org/10.1016/j.bbamcr.2018.12.011

Byrne, S., Jansen, L., U-King-Im, J. M., Siddiqui, A., Lidov, H. G., Bodi, I.,…Jungbluth, H. (2016). EPG5-related Vici syndrome: a paradigm of neurodevelopmental disorders with defective autophagy. *Brain*, *139*(Pt 3), 765-781. https://doi.org/10.1093/brain/awv393

Canty, J. T., Tan, R., Kusakci, E., Fernandes, J., & Yildiz, A. (2021). Structure and Mechanics of Dynein Motors. *Annu Rev Biophys*, *50*, 549-574. https://doi.org/10.1146/annurev-biophys-111020-101511

Cardoso, C. M., Groth-Pedersen, L., Høyer-Hansen, M., Kirkegaard, T., Corcelle, E., Andersen, J. S.,…Nylandsted, J. (2009). Depletion of kinesin 5B affects lysosomal distribution and stability and induces peri-nuclear accumulation of autophagosomes in cancer cells. *PLoS One*, *4*(2), e4424. https://doi.org/10.1371/journal.pone.0004424

Cason, S. E., Carman, P. J., Van Duyne, C., Goldsmith, J., Dominguez, R., & Holzbaur, E. L. F. (2021). Sequential dynein effectors regulate axonal autophagosome motility in a maturation-dependent pathway. *J Cell Biol*, *220*(7). https://doi.org/10.1083/jcb.202010179

Cason, S. E., & Holzbaur, E. L. F. (2023). Axonal transport of autophagosomes is regulated by dynein activators JIP3/JIP4 and ARF/RAB GTPases. *J Cell Biol*, *222*(12). https://doi.org/10.1083/jcb.202301084

Chaudhry, N., Sica, M., Surabhi, S., Hernandez, D. S., Mesquita, A., Selimovic, A.,…Jenny, A. (2022). Lamp1 mediates lipid transport, but is dispensable for autophagy in Drosophila. *Autophagy*, *18*(10), 2443-2458. https://doi.org/10.1080/15548627.2022.2038999

Cheng, X. T., Zhou, B., Lin, M. Y., Cai, Q., & Sheng, Z. H. (2015). Axonal autophagosomes recruit dynein for retrograde transport through fusion with late endosomes. *J Cell Biol*, *209*(3), 377-386. https://doi.org/10.1083/jcb.201412046

Clark, I. E., Jan, L. Y., & Jan, Y. N. (1997). Reciprocal localization of Nod and kinesin fusion proteins indicates microtubule polarity in the Drosophila oocyte, epithelium, neuron and muscle. *Development*, *124*(2), 461-470. https://doi.org/10.1242/dev.124.2.461

Dix, C. I., Soundararajan, H. C., Dzhindzhev, N. S., Begum, F., Suter, B., Ohkura, H.,…Bullock, S. L. (2013). Lissencephaly-1 promotes the recruitment of dynein and dynactin to transported mRNAs. *J Cell Biol*, *202*(3), 479-494. https://doi.org/10.1083/jcb.201211052

Fass, E., Shvets, E., Degani, I., Hirschberg, K., & Elazar, Z. (2006). Microtubules support production of starvation-induced autophagosomes but not their targeting and fusion with lysosomes. *J Biol Chem*, *281*(47), 36303-36316. https://doi.org/10.1074/jbc.M607031200

Fu, M. M., Nirschl, J. J., & Holzbaur, E. L. F. (2014). LC3 binding to the scaffolding protein JIP1 regulates processive dynein-driven transport of autophagosomes. *Dev Cell*, *29*(5), 577-590. https://doi.org/10.1016/j.devcel.2014.04.015

Fujiwara, T., Ye, S., Castro-Gomes, T., Winchell, C. G., Andrews, N. W., Voth, D. E.,…Zhao, H. (2016). PLEKHM1/DEF8/RAB7 complex regulates lysosome positioning and bone homeostasis. *JCI Insight*, *1*(17), e86330. https://doi.org/10.1172/jci.insight.86330

Gillingham, A. K., Sinka, R., Torres, I. L., Lilley, K. S., & Munro, S. (2014). Toward a comprehensive map of the effectors of rab GTPases. *Dev Cell*, *31*(3), 358-373. https://doi.org/10.1016/j.devcel.2014.10.007

Hargitai, D., Nagy, A., Bodor, I., Szenci, G., Laczkó-Dobos, H., Bhattacharjee, A.,…Lőrincz, P. (2025). HOPS-dependent vesicle tethering lock inhibits endolysosomal fusions and autophagosome secretion upon the loss of Syntaxin17. *Sci Adv*, *11*(23), eadu9605. https://doi.org/10.1126/sciadv.adu9605

Hegedus, K., Takats, S., Boda, A., Jipa, A., Nagy, P., Varga, K.,…Juhasz, G. (2016). The Ccz1-Mon1-Rab7 module and Rab5 control distinct steps of autophagy. *Mol Biol Cell*, *27*(20), 3132-3142. https://doi.org/10.1091/mbc.E16-03-0205

Hill, S. E., & Colón-Ramos, D. A. (2020). The Journey of the Synaptic Autophagosome: A Cell Biological Perspective. *Neuron*, *105*(6), 961-973. https://doi.org/10.1016/j.neuron.2020.01.018

Hofmann, I., & Munro, S. (2006). An N-terminally acetylated Arf-like GTPase is localised to lysosomes and affects their motility. *J Cell Sci*, *119*(Pt 8), 1494-1503. https://doi.org/10.1242/jcs.02958

Hori, I., Otomo, T., Nakashima, M., Miya, F., Negishi, Y., Shiraishi, H.,…Saitoh, S. (2017). Defects in autophagosome-lysosome fusion underlie Vici syndrome, a neurodevelopmental disorder with multisystem involvement. *Sci Rep*, *7*(1), 3552. https://doi.org/10.1038/s41598-017-02840-8

Ikenaka, K., Kawai, K., Katsuno, M., Huang, Z., Jiang, Y. M., Iguchi, Y.,…Sobue, G. (2013). dnc-1/dynactin 1 knockdown disrupts transport of autophagosomes and induces motor neuron degeneration. *PLoS One*, *8*(2), e54511. https://doi.org/10.1371/journal.pone.0054511

Jahreiss, L., Menzies, F. M., & Rubinsztein, D. C. (2008). The itinerary of autophagosomes: from peripheral formation to kiss-and-run fusion with lysosomes. *Traffic*, *9*(4), 574-587. https://doi.org/10.1111/j.1600-0854.2008.00701.x

Jordens, I., Fernandez-Borja, M., Marsman, M., Dusseljee, S., Janssen, L., Calafat, J.,…Neefjes, J. (2001). The Rab7 effector protein RILP controls lysosomal transport by inducing the recruitment of dynein-dynactin motors. *Curr Biol*, *11*(21), 1680-1685. https://doi.org/10.1016/s0960-9822(01)00531-0

Kim, S., Naylor, S. A., & DiAntonio, A. (2012). Drosophila Golgi membrane protein Ema promotes autophagosomal growth and function. *Proc Natl Acad Sci U S A*, *109*(18), E1072-1081. https://doi.org/10.1073/pnas.1120320109

Kim, S., Wairkar, Y. P., Daniels, R. W., & DiAntonio, A. (2010). The novel endosomal membrane protein Ema interacts with the class C Vps-HOPS complex to promote endosomal maturation. *J Cell Biol*, *188*(5), 717-734. https://doi.org/10.1083/jcb.200911126

Kimura, S., Noda, T., & Yoshimori, T. (2008). Dynein-dependent movement of autophagosomes mediates efficient encounters with lysosomes. *Cell Struct Funct*, *33*(1), 109-122.
Köchl, R., Hu, X. W., Chan, E. Y., & Tooze, S. A. (2006). Microtubules facilitate autophagosome formation and fusion of autophagosomes with endosomes. *Traffic*, *7*(2), 129-145. https://doi.org/10.1111/j.1600-0854.2005.00368.x
Korolchuk, V. I., Saiki, S., Lichtenberg, M., Siddiqi, F. H., Roberts, E. A., Imarisio, S.,…Rubinsztein, D. C. (2011). Lysosomal positioning coordinates cellular nutrient responses. *Nat Cell Biol*, *13*(4), 453-460. https://doi.org/10.1038/ncb2204
Lakatos, Z., Benkő, P., Juhász, G., & Lőrincz, P. (2021). Drosophila Rab39 Attenuates Lysosomal Degradation. *Int J Mol Sci*, *22*(19). https://doi.org/10.3390/ijms221910635
Lee, S., Sato, Y., & Nixon, R. A. (2011). Lysosomal proteolysis inhibition selectively disrupts axonal transport of degradative organelles and causes an Alzheimer's-like axonal dystrophy. *J Neurosci*, *31*(21), 7817-7830. https://doi.org/10.1523/JNEUROSCI.6412-10.2011
Lei, Y., & Klionsky, D. J. (2021). The Emerging Roles of Autophagy in Human Diseases. *Biomedicines*, *9*(11). https://doi.org/10.3390/biomedicines9111651
Lőrincz, P., & Juhász, G. (2020). Autophagosome-Lysosome Fusion. *J Mol Biol*, *432*(8), 2462-2482. https://doi.org/10.1016/j.jmb.2019.10.028
Lőrincz, P., Kenéz, L. A., Tóth, S., Kiss, V., Varga, Á., Csizmadia, T.,…Juhász, G. (2019). Vps8 overexpression inhibits HOPS-dependent trafficking routes by outcompeting Vps41/Lt. *Elife*, *8*. https://doi.org/10.7554/eLife.45631
Lőrincz, P., Lakatos, Z., Varga, Á., Maruzs, T., Simon-Vecsei, Z., Darula, Z.,…Juhász, G. (2016). MiniCORVET is a Vps8-containing early endosomal tether in Drosophila. *Elife*, *5*. https://doi.org/10.7554/eLife.14226
Lőrincz, P., Mauvezin, C., & Juhász, G. (2017). Exploring Autophagy in Drosophila. *Cells*, *6*(3). https://doi.org/10.3390/cells6030022
Lorincz, P., Toth, S., Benko, P., Lakatos, Z., Boda, A., Glatz, G.,…Juhasz, G. (2017). Rab2 promotes autophagic and endocytic lysosomal degradation. *J Cell Biol*, *216*(7), 1937-1947. https://doi.org/10.1083/jcb.201611027
Ma, X., Liu, K., Li, J., Li, H., Liu, Y., Yang, C., & Liang, H. (2018). A non-canonical GTPase interaction enables ORP1L-Rab7-RILP complex formation and late endosome positioning. *J Biol Chem*, *293*(36), 14155-14164. https://doi.org/10.1074/jbc.RA118.001854
Maday, S., Wallace, K. E., & Holzbaur, E. L. (2012). Autophagosomes initiate distally and mature during transport toward the cell soma in primary neurons. *J Cell Biol*, *196*(4), 407-417. https://doi.org/10.1083/jcb.201106120
Marwaha, R., Arya, S. B., Jagga, D., Kaur, H., Tuli, A., & Sharma, M. (2017). The Rab7 effector PLEKHM1 binds Arl8b to promote cargo traffic to lysosomes. *J Cell Biol*, *216*(4), 1051-1070. https://doi.org/10.1083/jcb.201607085
Mauvezin, C., Neisch, A. L., Ayala, C. I., Kim, J., Beltrame, A., Braden, C. R.,…Neufeld, T. P. (2016). Coordination of autophagosome-lysosome fusion and transport by a Klp98A-Rab14 complex in Drosophila. *J Cell Sci*, *129*(5), 971-982. https://doi.org/10.1242/jcs.175224
Meneghetti, G., Skobo, T., Chrisam, M., Facchinello, N., Fontana, C. M., Bellesso, S.,…Dalla Valle, L. (2019). The epg5 knockout zebrafish line: a model to study Vici syndrome. *Autophagy*, *15*(8), 1438-1454. https://doi.org/10.1080/15548627.2019.1586247
Neisch, A. L., Neufeld, T. P., & Hays, T. S. (2017). A STRIPAK complex mediates axonal transport of autophagosomes and dense core vesicles through PP2A regulation. *J Cell Biol*, *216*(2), 441-461. https://doi.org/10.1083/jcb.201606082
Olenick, M. A., & Holzbaur, E. L. F. (2019). Dynein activators and adaptors at a glance. *J Cell Sci*, *132*(6). https://doi.org/10.1242/jcs.227132
Pankiv, S., Alemu, E. A., Brech, A., Bruun, J. A., Lamark, T., Overvatn, A.,…Johansen, T. (2010). FYCO1 is a Rab7 effector that binds to LC3 and PI3P to mediate microtubule

plus end-directed vesicle transport. *J Cell Biol*, *188*(2), 253-269. https://doi.org/10.1083/jcb.200907015
Parzych, K. R., & Klionsky, D. J. (2014). An overview of autophagy: morphology, mechanism, and regulation. *Antioxid Redox Signal*, *20*(3), 460-473. https://doi.org/10.1089/ars.2013.5371
Poteryaev, D., Datta, S., Ackema, K., Zerial, M., & Spang, A. (2010). Identification of the switch in early-to-late endosome transition. *Cell*, *141*(3), 497-508. https://doi.org/10.1016/j.cell.2010.03.011
Rahman, A., Lőrincz, P., Gohel, R., Nagy, A., Csordás, G., Zhang, Y.,…Nezis, I. P. (2022). GMAP is an Atg8a-interacting protein that regulates Golgi turnover in Drosophila. *Cell Rep*, *39*(9), 110903. https://doi.org/10.1016/j.celrep.2022.110903
Ravikumar, B., Acevedo-Arozena, A., Imarisio, S., Berger, Z., Vacher, C., O'Kane, C. J.,…Rubinsztein, D. C. (2005). Dynein mutations impair autophagic clearance of aggregate-prone proteins. *Nat Genet*, *37*(7), 771-776. https://doi.org/10.1038/ng1591
Redwine, W. B., DeSantis, M. E., Hollyer, I., Htet, Z. M., Tran, P. T., Swanson, S. K.,…Reck-Peterson, S. L. (2017). The human cytoplasmic dynein interactome reveals novel activators of motility. *Elife*, *6*. https://doi.org/10.7554/eLife.28257
Riedel, F., Gillingham, A. K., Rosa-Ferreira, C., Galindo, A., & Munro, S. (2016). An antibody toolkit for the study of membrane traffic in Drosophila melanogaster. *Biol Open*, *5*(7), 987-992. https://doi.org/10.1242/bio.018937
Rosa-Ferreira, C., & Munro, S. (2011). Arl8 and SKIP act together to link lysosomes to kinesin-1. *Dev Cell*, *21*(6), 1171-1178. https://doi.org/10.1016/j.devcel.2011.10.007
Rosa-Ferreira, C., Sweeney, S. T., & Munro, S. (2018). The small G protein Arl8 contributes to lysosomal function and long-range axonal transport in. *Biol Open*, *7*(9). https://doi.org/10.1242/bio.035964
Scott, R. C., Schuldiner, O., & Neufeld, T. P. (2004). Role and regulation of starvation-induced autophagy in the Drosophila fat body. *Dev Cell*, *7*(2), 167-178. https://doi.org/10.1016/j.devcel.2004.07.009
Siller, K. H., Serr, M., Steward, R., Hays, T. S., & Doe, C. Q. (2005). Live imaging of Drosophila brain neuroblasts reveals a role for Lis1/dynactin in spindle assembly and mitotic checkpoint control. *Mol Biol Cell*, *16*(11), 5127-5140. https://doi.org/10.1091/mbc.e05-04-0338
Sitaram, P., Anderson, M. A., Jodoin, J. N., Lee, E., & Lee, L. A. (2012). Regulation of dynein localization and centrosome positioning by Lis-1 and asunder during Drosophila spermatogenesis. *Development*, *139*(16), 2945-2954. https://doi.org/10.1242/dev.077511
Stenmark, H. (2009). Rab GTPases as coordinators of vesicle traffic. *Nat Rev Mol Cell Biol*, *10*(8), 513-525. https://doi.org/10.1038/nrm2728
Sun, T., Song, Y., Dai, J., Mao, D., Ma, M., Ni, J. Q.,…Pastor-Pareja, J. C. (2019). Spectraplakin Shot Maintains Perinuclear Microtubule Organization in Drosophila Polyploid Cells. *Dev Cell*, *49*(5), 731-747.e737. https://doi.org/10.1016/j.devcel.2019.03.027
Swan, A., Nguyen, T., & Suter, B. (1999). Drosophila Lissencephaly-1 functions with Bic-D and dynein in oocyte determination and nuclear positioning. *Nat Cell Biol*, *1*(7), 444-449. https://doi.org/10.1038/15680
Szatmári, Z., Kis, V., Lippai, M., Hegedus, K., Faragó, T., Lorincz, P.,…Sass, M. (2014). Rab11 facilitates cross-talk between autophagy and endosomal pathway through regulation of Hook localization. *Mol Biol Cell*, *25*(4), 522-531. https://doi.org/10.1091/mbc.E13-10-0574
Tabata, K., Matsunaga, K., Sakane, A., Sasaki, T., Noda, T., & Yoshimori, T. (2010). Rubicon and PLEKHM1 negatively regulate the endocytic/autophagic pathway via a novel Rab7-binding domain. *Mol Biol Cell*, *21*(23), 4162-4172. https://doi.org/10.1091/mbc.E10-06-0495
Takáts, S., Nagy, P., Varga, Á., Pircs, K., Kárpáti, M., Varga, K.,…Juhász, G. (2013). Autophagosomal Syntaxin17-dependent lysosomal degradation maintains neuronal

function in Drosophila. *J Cell Biol*, *201*(4), 531-539. https://doi.org/10.1083/jcb.201211160

Takáts, S., Pircs, K., Nagy, P., Varga, Á., Kárpáti, M., Hegedűs, K.,…Juhász, G. (2014). Interaction of the HOPS complex with Syntaxin 17 mediates autophagosome clearance in Drosophila. *Mol Biol Cell*, *25*(8), 1338-1354. https://doi.org/10.1091/mbc.E13-08-0449

Tillery, M. M. L., Blake-Hedges, C., Zheng, Y., Buchwalter, R. A., & Megraw, T. L. (2018). Centrosomal and Non-Centrosomal Microtubule-Organizing Centers (MTOCs) in Drosophila melanogaster. *Cells*, *7*(9), 121.

van der Kant, R., Fish, A., Janssen, L., Janssen, H., Krom, S., Ho, N.,…Neefjes, J. (2013). Late endosomal transport and tethering are coupled processes controlled by RILP and the cholesterol sensor ORP1L. *J Cell Sci*, *126*(Pt 15), 3462-3474. https://doi.org/10.1242/jcs.129270

Vaughan, K. T., & Vallee, R. B. (1995). Cytoplasmic dynein binds dynactin through a direct interaction between the intermediate chains and p150Glued. *J Cell Biol*, *131*(6 Pt 1), 1507-1516. https://doi.org/10.1083/jcb.131.6.1507

Wang, T., Martin, S., Papadopulos, A., Harper, C. B., Mavlyutov, T. A., Niranjan, D.,…Meunier, F. A. (2015). Control of autophagosome axonal retrograde flux by presynaptic activity unveiled using botulinum neurotoxin type a. *J Neurosci*, *35*(15), 6179-6194. https://doi.org/10.1523/JNEUROSCI.3757-14.2015

Wang, Z., Miao, G., Xue, X., Guo, X., Yuan, C., Zhang, G.,…Zhang, H. (2016). The Vici Syndrome Protein EPG5 Is a Rab7 Effector that Determines the Fusion Specificity of Autophagosomes with Late Endosomes/Lysosomes. *Mol Cell*, *63*(5), 781-795. https://doi.org/10.1016/j.molcel.2016.08.021

Wong, Y. C., & Holzbaur, E. L. (2014). The regulation of autophagosome dynamics by huntingtin and HAP1 is disrupted by expression of mutant huntingtin, leading to defective cargo degradation. *J Neurosci*, *34*(4), 1293-1305. https://doi.org/10.1523/JNEUROSCI.1870-13.2014

Zhang, S., Tong, M., Zheng, D., Huang, H., Li, L., Ungermann, C.,…Zhong, Q. (2023). C9orf72-catalyzed GTP loading of Rab39A enables HOPS-mediated membrane tethering and fusion in mammalian autophagy. *Nat Commun*, *14*(1), 6360. https://doi.org/10.1038/s41467-023-42003-0

Zheng, Y., Buchwalter, R. A., Zheng, C., Wight, E. M., Chen, J. V., & Megraw, T. L. (2020). A perinuclear microtubule-organizing centre controls nuclear positioning and basement membrane secretion. *Nat Cell Biol*, *22*(3), 297-309. https://doi.org/10.1038/s41556-020-0470-7

Figure legends

Figure 1. Autophagosomes move towards the ncMTOC in fat cells. A: Schematic drawing of the experimental design for screening. **B:** Non-fused autophagosomes accumulate in the perinuclear region upon Vps16A silencing. **C:** The cis-Golgi compartment remains unchanged upon the expression of *vps16a* RNAi. **D, E:** The accumulation of autophagosomes is not perinuclear in *α* or *β tubulin*; *vps16a* double RNAi cells. The boxed areas in the main panels, marked by cyan, are enlarged in the insets (D' and E'). **F-I:** Quantification of data shown in B-E; n=10 cells. **J, K:** Autophagosomes position at an ectopic MTOC (yellow arrows) formed upon Shot silencing. (29 out of 41 cells exhibited an ectopic MTOC = 70.73%). **L:** Autophagosomes are near microtubule minus-ends, marked by Khc-nod-LacZ. The boxed area in the main panels, marked by cyan, is enlarged in L''' (proximity sites indicated by cyan arrowheads). **M, N:** Correlative ultrastructural analysis shows autophagosomes accumulating near the nucleus upon Vps16A silencing (border of control and silencing cells marked by green) (M). Shot knockdown causes aggregation of autophagosomes in ectopic foci in *vps16a* RNAi cells (N). An ectopic cleavage furrow (hallmark of Shot depletion (Sun et al., 2019)) is also visible (cyan arrows in N'). Note: the magnification of N is higher to better show this structure. **O, P:** Atg8a positive autophagosomes are clustered around the ectopic MTOC (yellow arrows) which is encircled by the signal of the minus-end marker Khc-nod-LacZ in *shot* RNAi (O) and *vps16a; shot* double RNAi cells (P). The boxed areas in the main panels, marked by cyan, are enlarged in O', O", P' and P". Nuclei are outlined in blue in J', L'-L''', O', O", P' and P". The GFP signal of RNAi and Khc-nod-LacZ expressing cells is false-colored blue in composite images. **Q-S:** Quantification of data shown in L, O, P; n=10 cells. The boundaries of RNAi cells are highlighted in magenta in the grayscale panels.

Figure 2. A dynein-dynactin complex is required for minus-end directed autophagosome transport. A-G: Knockdown of dynein (A-D) and dynactin subunits (E-G) results in the peripheral redistribution of autophagosomes in *vps16a* RNAi cells (red arrows). **H, I:** Kinesin silencing does not affect the perinuclear accumulation of autophagosomes in *vps16a* RNAi cells. **J:** Proposed model of the suggested dynein-dynactin complex responsible for autophagosome positioning in fat cells. DHC: dynein heavy chain; DIC: dynein intermediate chain; DLIC: dynein light intermediate chain; DLC: dynein light chain. **K:** Quantification of data shown in A-I; n=10 cells. The boundaries of RNAi cells are highlighted in magenta in the grayscale panels.

Figure 3. The proper dynein/kinesin ratio determines the directionality of autophagosome transport. A, B: Overexpression of kinesin motors blocks the minus-end transport of autophagosomes, leading to their accumulation in the cell periphery in *vps16a* RNAi cells (red arrows). **C:** In dynactin-kinesin-*vps16a* triple RNAi cells, autophagosomes are distributed throughout the cytoplasm. **D:** Overexpression of the recombinant minus-end motor Khc-nod-LacZ does not affect minus-end directed autophagosome transport in *vps16a* RNAi cells. **E:** Khc-nod-LacZ expression partially rescues the dynactin KD-induced peripheral redistribution of autophagosomes in *vps16a* RNAi cells. **F:** Quantification of data shown in A-E; n=10. Data for *dctn1-p150* RNAi is included as a positive control for peripheral distribution (shown in Figure 2E, K). **G, H:** Overexpressed Klp98A-3xHA accumulates at the periphery of marginal fat body cells, specifically on the side facing the body cavity and in contact with the hemolymph (red arrows), in both control (G) and fusion-inhibited (*vps16a* RNAi) cells (H). The boundaries of RNAi or kinesin overexpressing cells are highlighted in magenta in the grayscale panels. Fat body edges are outlined in white in G' and H'.

Figure 4. Rab7 and Rab39 small GTPases and their interactors are responsible for bidirectional movement of autophagosomes. A-H: Knockdown of Rab7 (A), its interactor Epg5 (B), the subunits of its guanine nucleotide exchange factor Mon1 (C) and Ccz1 (D), as well as Rab39 (E) and its interactor ema (F), inhibits the perinuclear positioning of autophagosomes in *vps16a* RNAi cells. In contrast, other factors such as Plekhm1 (G) and prd1 (H) do not affect autophagosome positioning. **I**: Proposed model of Rab small GTPases

with their adaptors involved in autophagosome positioning. **J**: Quantification of data shown in A-H; n=10 cells. The boundaries of RNAi cells are highlighted in magenta in the grayscale panels.

Figure 5. Epg5 is responsible for bidirectional movement of autophagosomes. A-B: The distribution of Atg8a (A) or Rab7 (B) positive autophagosomes becomes dispersed upon the expression of *epg5* and *vps16a* RNAi. **C:** Overexpression of YFP-tagged Rab7 does not rescue the scattered distribution of mCherry-Atg8a positive autophagosomes in the absence of Epg5 in *vps16a* RNAi cells, even though the colocalization of YFP-Rab7 with mCherry-Atg8a remains unaffected. Cyan arrowheads in the grayscale panels point to YFP-Rab7 and mCherry-Atg8a double positive dots. **D:** The localization of Arl8 positive lysosomes remains perinuclear in *epg5*, *vps16a* double RNAi cells. The boundaries of RNAi and YFP-Rab7 expressing cells are highlighted in magenta in the grayscale panels. **E-H:** Quantification of data shown in A-D; n=10 cells. **I, J:** Epg5-9xHA colocalizes with endogenous Rab7 (I) or Atg8a (J) positive structures in S2R+ cells. Cyan arrowheads within insets (marked by cyan boxes in panels I and J) point to Epg5-9xHA and Rab7 or Atg8a double positive structures, respectively. I' and J' show scatter plots generated from the images of cells in panels I and J, respectively, depicting the intensity correlation profiles of Epg5-9xHA with Rab7 or Atg8a. Pearson correlation coefficients (R) are indicated, with the average R (n=10 cells) also shown, indicating colocalization in both cases. **K:** Epg5-9xHA colocalizes with Atg8a positive, Lamp1-3xmCherry negative (pre-fusion) autophagosomes, as well as with Atg8a and Lamp1-3xmCherry double positive autolysosomes in S2R+ cells. Cyan arrowheads in insets (marked by a cyan box in panel K) point to Epg5-9xHA, Atg8a double positive, Lamp1-3xmCherry negative structures, while a yellow arrowhead marks a triple positive autolysosome. K' and K": Scatter plots based on the cell in panel K, show intensity correlations of Epg5-9xHA with Lamp1-3xmCherry and Atg8a, respectively. Pearson correlation coefficients indicate partial colocalizations. **L, M:** Coimmunoprecipitation experiments show that Epg5-9xHA binds to Rab7-FLAG (L) and endogenous Dhc64C (M) in cultured *Drosophila* cells. The asterisk in L marks immunoglobulin light chain. The smeared input bands of Dhc64C in panel M are due to the large size of Dhc64C, which affects its migration characteristics.

Figure 6. A-H: Knockdown of key regulators of autophagosome transport in a Snap29 RNAi background results in autophagosome localization patterns similar to those observed with Vps16A RNAi. A-H: In luciferase; Snap29 double knockdown cells, non-fused autophagosomes accumulate in the perinuclear region, marked by mCherry-Atg8a (A). Shot; Snap29 double knockdown causes autophagosomes to accumulate around an ectopic MTOC (B), marked by yellow arrows in B'. Nuclear outlines are shown in blue. Dhc64C knockdown in Snap29 RNAi cells causes autophagosomes to redistribute to the cell periphery (C, red arrows in C'). Khc knockdown does not alter the perinuclear distribution of autophagosomes seen in Snap29 RNAi cells (D). Co-knockdown of Snap29 with Rab7 (E), Epg5 (F), Rab39 (G), or ema (H) results in scattered autophagosome distribution throughout the cytoplasm. In grayscale panels, the boundaries of RNAi-expressing cells are highlighted in magenta. **I:** Quantification of the data shown in panels A and C–H. n = 10 cells.

Figure 7. The positioning of pre-fusion, immature autolysosomes is very similar to autophagosomes in *vps16a* RNAi cells. A-J: Lamp1 positive lysosomes accumulate around the nuclei in cells co-expressing a control (*luciferase*) RNAi (A). This positioning remains unaffected by the co-expression of *khc* (E) or *arl8* RNAi (J). Depletion of Shot (B) or Dhc64C (C) in *vps16a* RNAi cells redistributes Lamp1 positive lysosomes from the perinuclear cytoplasm to an ectopic MTOC (yellow arrows) or to the periphery, respectively. Lamp1 positive lysosomes are scattered throughout the cytosol in *vps16a* RNAi cells upon the co-expression of *rab7* (F), *rab39* (G), and *ema* (H) RNAi-s. In contrast, Lamp1 positive lysosomes retain their perinuclear distribution in *epg5, vps16a* double RNAi cells (D). Similar to Rab7 or Rab39, the expression of *rab2* RNAi in Vps16A KD cells results in the scattering of Lamp1 positive lysosomes, with a trend observed that lysosomes tend to accumulate near the periphery (red arrows) (I). The boundaries of RNAi-expressing cells are highlighted in

magenta in the grayscale panels. The outlines of nuclei are drawn in blue in B'. **K, L:** Quantification of data shown in A, C-J; n=10 cells.

Figure 8. Epg5 regulates autolysosome maturation. A, B: Epg5 knockdown results in a significant reduction in the size of 3xmCherry-Atg8a positive autolysosomes (B) compared to control RNAi (*luciferase* RNAi) expressing cells (A). **C, D**: *epg5* RNAi cells lack large Rab7 (C) and Arl8 (D) positive autolysosomes, which are present in surrounding control cells (cyan arrowheads in insets point to Rab7 and Arl8 positive autolysosomes in control cells). The boundaries of RNAi cells are highlighted in magenta in the grayscale panels. **E-H:** Quantification of data shown in A-D; n=10 cells.

Figure 9. Minus-end directed transport is required for autolysosome maturation. A-E: Autolysosome size is significantly reduced upon the loss of dynein (A-D) or dynactin (E) function. Red arrows point to autolysosomes at the cell periphery in A'-E' and in the inset of E. **F, G:** Kinesin knockdowns do not significantly influence autolysosome size. **H:** Autolysosome size increases at ectopic foci (yellow arrows) in *shot* RNAi cells. The boundaries of RNAi-expressing cells are highlighted in magenta in the grayscale panels. The outlines of nuclei are drawn in blue in the inset of E' and in H'. **I-L:** Quantification of data shown in A-H; n=10 cells.

Figure 10. Loss of the autophagosome positioning machinery decreases autophagosome-lysosome fusion. A-G: In starved control RNAi (*luciferase*) expressing cells, mCherry-Atg8a overlaps with endogenous Lamp1 (A), indicating normal autophagosome-lysosome fusion and autolysosome formation. Autolysosomes still form in *shot* (B) or *khc* RNAi (C) cells, as mCherry-Atg8a colocalizes with endogenous Lamp1 similar to controls, but these are found in ectopic foci (yellow arrows) in *shot* RNAi cells. The outlines of nuclei are drawn in blue in B' and B''. Conversely, RNAi-s targeting factors responsible for minus-end directed autophagosome transport (D-G) decrease this overlap, suggesting less effective autophagosome-lysosome fusion. The GFP signal of RNAi-expressing cells is false-colored blue in composite images. The boundaries of RNAi-expressing cells are highlighted in magenta. The boxed areas in the main panels, marked by cyan, are enlarged in the insets (M, merged image; A8, 3xmCherry-Atg8a; L1, Lamp1). Cyan arrowheads point to mCherry-Atg8a/Lamp1 double-positive structures, while magenta and green arrows indicate mCherry-Atg8a or Lamp1 single-positive dots, respectively. **H:** Quantification of data shown in A-G; n=10 cells.

Figure 11. Model of the transport of autophagosomes and lysosomes in starved fat cells. Before fusion, autophagosomes and lysosomes are transported towards the perinuclear ncMTOC by a cytosolic dynein complex in starved fat cells to ensure proper fusion and effective degradation. This process requires Rab7, Rab39, and their interactors Epg5 and ema on autophagosomes, and Rab2, Rab7, Rab39, and the Rab39 interactor ema, but not Epg5, on lysosomes. After fusion, Arl8 mediates the plus-end transport of autolysosomes, while Rab39 promotes dynein-regulated minus-end directed transport. Thus, the motility of pre-fusion and post-fusion organelles is differently regulated: pre-fusion organelles generally move towards the MTOC, while post-fusion organelles exhibit bidirectional motility. This spatial regulation ensures proper fusion rates and degradation efficiency.

Supplementary Figures and Files

Figure 1—figure supplement 1. A-C: Immunostainings for Atg8a (A), Rab7 (B), and Arl8 (C) show that pre-fusion autophagosomes (Atg8a and Rab7 positive) and pre-fusion lysosomes (Arl8 positive) accumulate in the perinuclear region in *vps16a* RNAi cells. **D, E:** Atg8a (D) or Atg1 (E) knockdown eliminates the mCherry-Atg8a signal from *vps16a* RNAi cells. **F, G:** Silencing of Shot using two additional independent RNAi lines also results in the formation of an ectopic MTOC (marked by yellow arrows) in Vps16A depleted cells, around which autophagosomes accumulate. An ectopic MTOC was present in 29 out of 38 cells (RNAi/2) and 23 out of 29 cells (RNAi/3), representing 76.32% and 79.31%, respectively. **H-K:** Quantification of data shown in A-E; n=10 cells. The boundaries of RNAi-expressing cells are highlighted in magenta in the grayscale panels. The outlines of nuclei are drawn in blue in F' and G'.

Figure 2—figure supplement 1. A-C: Silencing of dynein and dynactin subunits (Dhc64C in A, DCTN1-p150 in B, and DCTN2-p50 in C) using independent RNAi lines also leads to the peripheral redistribution of mCherry-Atg8a positive autophagosomes in *vps16a* RNAi cells (red arrows). **D-I:** Peripheral accumulation (red arrows) of Atg8a (D-F) or Rab7 (G-I) positive autophagosomes can be seen in *dhc64c, vps16a* (D, G), *dlic, vps16a* (E, H), or *dctn1-p150, vps16a* (F, I) double RNAi cells. **J, K:** Overexpression of a dominant negative form of DCTN1-p150 or wild type DCTN2-p50 (which exhibits a dominant-negative effect) in Vps16A depleted cells also results in the peripheral redistribution of mCherry-Atg8a positive autophagosomes (red arrows). **L, M:** Silencing of the dynein light chain Dlc90F and the dynactin subunit cpa in Vps16A KD cells results in a weaker phenotype, with mCherry-Atg8a positive autophagosomes scattered in the cytosol. **N, O:** Knockdown of Girdin (N), a suggested dynein activator, and the dynein regulator Lis-1 (O) results in a generally dispersed distribution of mCherry-Atg8a positive autophagosomes in *vps16a* RNAi cells. **P, Q:** The perinuclear distribution of autophagosomes in *vps16a* RNAi cells remains unaffected by the co-expression of *khc* (P) or *klc* (Q) RNAi. The boundaries of RNAi-expressing cells are highlighted in magenta in the grayscale panels. **R-V:** Quantification of data shown in A-Q; n=10 cells.

Figure 4—figure supplement 1. A: Expression of an independent *rab39* RNAi in *vps16a* RNAi cells results in the scattering of mCherry-Atg8a positive autophagosomes. **B:** Atg8a positive autophagosomes accumulate throughout the cytoplasm in *rab7, vps16a* double RNAi cells. **C-D:** Atg8a positive autophagosomes are scattered throughout the cytosol in *rab39, vps16a* (C) or *ema, vps16a* (D) double RNAi cells. **E:** Expression of *rab7* RNAi in Vps16A KD cells eliminates the Rab7 signal, indicating effective RNA interference. **F:** Rab7 positive structures (autophagosomes) are scattered throughout the cytosol in *rab39, vps16a* double RNAi cells. The boundaries of RNAi-expressing cells are highlighted in magenta in the grayscale panels. **G-I:** Quantification of data shown in A-D, F; n=10 cells.

Figure 4—figure supplement 2. A-D: Silencing the endolysosomal small GTPases Rab2 (A), Rab5 (B), Rab14 (C), and Arl8 (D) does not alter the perinuclear positioning of mCherry-Atg8a positive autophagosomes in *vps16a* RNAi cells. **E, F:** Rab11 knockdown leads to the scattering of mCherry-Atg8a positive autophagosomes in *vps16a* RNAi cells (E), which appears to be due to the extreme accumulation of autophagosomes, as indicated by endogenous Atg8a immunostaining (F). The boundaries of RNAi-expressing cells are highlighted in magenta in the grayscale panels. **G, H:** Quantification of data shown in A-F; n=10 cells.

Figure 4—figure supplement 3. A-L: Overexpressing the wild-type (WT) and constitutively active (CA) YFP or GFP-tagged forms of selected endolysosomal/autophagosomal Rab GTPases (Rab7-WT: A, Rab7-CA: B, Rab2-WT: D, Rab2-CA: E, Rab39-WT: F, Rab39-CA: G, Rab11-WT: H, Rab11-CA: I, Rab5-WT: J, Rab5-CA: K, Rab14-WT: L) had no effect on the perinuclear distribution of mCherry-Atg8a positive autophagosomes in *vps16a* RNAi cells. The signals of both WT and CA forms of YFP-Rab7 and YFP-Rab2 strongly overlapped

with mCherry-Atg8a positive autophagosomes in *vps16a* RNAi cells (A, B, D, E), similar to endogenous Rab7 as evidenced by Rab7 immunostaining (C). The GFP signal of RNAi-expressing cells is false-colored blue in C. In contrast, the YFP-tagged WT form of Rab39 showed weak but apparent colocalization (cyan arrowheads) (F), while Rab11 did not colocalize with mCherry-Atg8a even when its CA form was expressed (H, I). Neither form of Rab5 overlapped with mCherry-Atg8a puncta (J, K), similar to Rab14 (L), indicating that these structures are either endosomes or lysosomes (magenta arrowheads point to autophagosomes in the grayscale panels of L). The boundaries of YFP/GFP-tagged Rab or GFP expressing cells are highlighted in magenta in the grayscale panels showing mCherry-Atg8a or Rab channels. The boxed areas in the main panels, marked by cyan, are enlarged in the insets. **M:** Potential roles of Rab GTPases in autophagosome transport and fusion. **N:** Quantification of data shown in A, B, D-L; n=10 cells.

Figure 5—figure supplement 1. A-D: The size, number and distribution of Rab7 (A, B) or FYVE-GFP positive endosomes (C, D) and Lamp1 positive lysosomes (C, D) remain unaffected by *epg5* RNAi expression (B, D) in nephrocytes, compared to controls (A, C). **E-K:** Quantification of data shown in A-D; E: n=512 (control) and 461 (*epg5* RNAi) endosomes from 10 cells. F: n=10 cells. G: n=496 (control) and 461 (*epg5* RNAi) endosomes from 10 cells. H: n=10 cells. I: n=15 cells. J: n=422 (control) and 397 (*epg5* RNAi) lysosomes from 10 cells. K: n=10 cells. **L, M:** Ultrastructural analysis reveals no significant difference in the endolysosomal compartment between control (L) and *epg5* RNAi (M) nephrocytes. α: late endosomes; β: lysosomes; m: mitochondria; LD: lipid droplets.

Figure 9—figure supplement 1. A: Silencing of Rab7 decreases mCherry-Atg8a positive autolysosome size as expected, and they remain generally dispersed. **B, C:** Knockdown of Rab39 (B), but not ema (C), relocates mCherry-Atg8a positive autolysosomes to the periphery (red arrows). Importantly, neither knockdown decreases the size of autolysosomes. The boundaries of RNAi-expressing cells are highlighted in magenta in the grayscale panels. **D, E:** Quantification of data shown in A-C; n=10 cells.

Figure 10—figure supplement 1. A-F: Partial inhibition of autophagosome-lysosome fusion is observed upon knockdown of factors responsible for minus-end transport, based on 3xmCherry-Atg8a and GFP-Lamp1 colocalization experiments. In starved control RNAi (*luciferase*) expressing cells, mCherry-Atg8a overlaps with GFP-Lamp1 (A), indicating normal autophagosome-lysosome fusion and autolysosome formation. Autolysosomes still form in *shot* (B) or *khc* RNAi cells (C), as mCherry-Atg8a colocalizes with GFP-Lamp1, but these are found in ectopic foci (yellow arrows) in the former case. The outlines of nuclei are drawn in blue in B', B". Conversely, RNAi-s targeting factors responsible for minus-end directed autophagosome transport (D-F), including *epg5* RNAi, decrease this overlap, suggesting less effective autophagosome-lysosome fusion. **G:** Quantification of data shown in A-F; n=10 cells. **H:** Silencing of Vps16A, used as a positive control, almost completely blocks autophagosome-lysosome fusion as indicated by the minimal overlap of the two signals. **I-K:** Quantification of data shown in H; n=10 cells. The boundaries of RNAi-expressing cells are highlighted in magenta in the grayscale panels. The boxed areas in the main panels, marked by cyan, are enlarged in the insets (M, merged image; A8, 3xmCherry-Atg8a; L1, GFP-Lamp1). Cyan arrowheads show overlapping dots, while magenta and green arrows point to non-colocalizing 3xmCherry-Atg8a positive and GFP-Lamp1 positive dots, respectively.

Supplementary File 1. Representative images of the phenotypes from all screened lines. The boundaries of silenced or overexpressing cells are highlighted in magenta, while positive hits are marked with green frames and captions.

Supplementary Table 1. Detailed information about the screened lines, including their sources, identifiers, and phenotypes. The autophagosome distribution phenotypes are presented graphically for enhanced visibility (see the legend included in the table).

Supplementary Table 2. Genotypes of the larvae and cells, along with a list of stocks from the screen used for the experiments shown in the figure panels.

Appendix 1

Key Resources Table

All the screened *Drosophila* lines, as well as their sources, identifiers and phenotypes are listed in **Supplementary Table 1**.

Key Resources Table				
Reagent type (species) or resource	**Designation**	**Source or reference**	**Identifiers**	**Additional information**
strain, strain background (*D. melanogaster*)	"*hs-Flp; UAS-DCR2; act<CD2<Gal4, UAS-GFPnls*"; "*hs-Flp; 3xmCherry-Atg8a, UAS-2xEGFP; act<CD2<Gal4, UAS-DCR2*"; "*hs-Flp; 3xmCherry-Atg8a, UAS-GFP-Lamp1; act<CD2<Gal4, UAS-DCR2*"	(Boda et al., 2019) doi: 10.1016/j.bbamcr.2018.12.011; (Lorincz et al., 2017) doi: 10.1083/jcb.201611027; (Takáts et al., 2013) doi: 10.1083/jcb.201211160		
genetic reagent (*D. melanogaster*)	*Vps16A RNAi GD*	Vienna Drosophila Resource Center (VDRC)	VDRC:23769; FLYB:FBst0455191	
genetic reagent (*D. melanogaster*)	*prospero-Gal4*	Bloomington Drosophila Stock Center (BDSC)	BDSC:80572; FLYB:FBst0080572	
genetic reagent (*D. melanogaster*)	*UAS-GFP-myc-2xFYVE*	BDSC	BDSC:42712; FLYB:FBst0042712	
cell line (*D. melanogaster*)	S2R+	Drosophila Genomics Resource Center (Stock 150)	RRID:CVCL_Z831	

transfected construct (*D. melanogaster*)	*genEpg5-9xHA*	this paper		transfected construct (*D. melanogaster*)
transfected construct (*D. melanogaster*)	*genLamp1-3xmCherry*	(Hegedus et al., 2016) doi: 10.1091/mbc.E16-03-0205	FLYB:FBtp0116217	transfected construct (*D. melanogaster*)
antibody	anti-Atg8a (Rat monoclonal)	(Takáts et al., 2013) doi: 10.1083/jcb.201211160		IF(1:800); IF in case of S2R+ cells(1:300)
antibody	anti-β-galactosidase (Rabbit monoclonal)	ZooMAb® (Sigma-Aldrich)	Cat# ZRB1700	IF(1:100)
antibody	anti-Gmap (Goat polyclonal)	Developmental Studies Hybridoma Bank (DSHB)	Cat# GMAP; RRID:AB_2618259	IF(1:1000)
antibody	anti-Rab7 (Mouse monoclonal)	DSHB; (Riedel et al., 2016) doi: 10.1242/bio.018937	Cat# Rab7; RRID:AB_2722471	IF(1:10)
antibody	anti-Arl8 (Rabbit polyclonal)	DSHB	Cat# Arl8; RRID:AB_2618258	IF(1:300)
antibody	anti-Lamp1 (Rabbit polyclonal)	(Chaudhry et al., 2022) doi: 10.1080/15548627.2022.2038999		IF(1:1000); Andreas Jenny
antibody	anti-mCherry (Rat polyclonal)	(Takáts et al., 2014) doi: 10.1091/mbc.E13-08-0449		IF(1:300)

antibody	anti-mCherry (Guinea pig polyclonal)	(Hegedus et al., 2016)		IF(1:500); Gábor Juhász
antibody	anti-HA (Rabbit polyclonal)	Sigma-Aldrich	Cat# H6908	IF(1:100)
antibody	anti-HA (Rabbit polyclonal)	Proteintech	Cat# 51064-2-AP	IF(1:200)
antibody	anti-HA (Rat monoclonal)	Roche	Cat# 3F10	WB(1:1000)
antibody	anti-GFP (Chicken polyclonal)	Invitrogen	Cat# A10262	IF(1:1500)
antibody	anti-FLAG M2 (Mouse monoclonal)	Sigma-Aldrich	Cat# F1804	WB(1:2000)
antibody	anti-Dhc (Mouse monoclonal)	DSHB	Cat# 2C11-2; RRID:AB_2091523	WB(1:12.5)
antibody	Alexa Fluor 568 anti-Rat (Goat polyclonal)	Invitrogen	Cat# A-11077	IF(1:1000)
antibody	Alexa Fluor 647 anti-Rabbit (Donkey polyclonal)	Invitrogen	Cat# A-31573	IF(1:600)
antibody	Alexa Fluor 568 anti-Goat (Donkey polyclonal)	Invitrogen	Cat# A-11057	IF(1:1000)

antibody	Alexa Fluor 568 anti-Mouse (Donkey polyclonal)	Invitrogen	Cat# A10037	IF(1:1000)
antibody	Alexa Fluor 647 anti-Mouse (Donkey polyclonal)	Invitrogen	Cat# A-31571	IF(1:600)
antibody	Alexa Fluor 568 anti-Rabbit (Donkey polyclonal)	Invitrogen	Cat# A10042	IF(1:1000)
antibody	Alexa Fluor 488 anti-Chicken (Goat polyclonal)	Invitrogen	Cat# A-11039	IF(1:1000)
antibody	Alexa Fluor 488 anti-Rat (Donkey polyclonal)	Invitrogen	Cat# A-21208	IF(1:1000)
antibody	Alexa Fluor 488 anti-Rabbit (Goat polyclonal)	Abcam	Cat# ab150077	IF(1:1000)
antibody	DyLight 550 anti-Guinea pig (Goat polyclonal)	Thermo Fisher	Cat# SA5-10095	IF(1:600)
antibody	anti-Rat-HRP (Goat polyclonal)	Sigma-Aldrich	Cat# A9037	
antibody	anti-Mouse-HRP (Rabbit polyclonal)	Sigma-Aldrich	Cat# A9044	
recombinant DNA reagent	*pGen-9xHA*	(Lőrincz et al., 2016) doi: 10.7554/eLife.14226		plasmid

recombinant DNA reagent	*pUAST-3xFLAG*	(Takáts et al., 2014) doi: 10.1091/mbc.E13-08-0449		plasmid
recombinant DNA reagent	*metallothionein-Gal4*	(Takáts et al., 2013) doi: 10.1083/jcb.201211160		plasmid
recombinant DNA reagent (*D. melanogaster*)	Rab7 cDNA clone	Drosophila Genomics Resource Center (DGRC)	DGRC Stock Number: 7144; RRID: RRID:DGRC_7144	cDNA
sequence-based reagent	genEpg5_F	this paper	PCR primers	CCAAGCTTGCATGCGGCCGCATTTTCTGTGCGCGACTGTTG
sequence-based reagent	genEpg5_R	this paper	PCR primers	TAAAAGATGCGGCCGGTACCGCCTCCACCCGTGGCCATTAACTTGAATTC
sequence-based reagent	Rab7CDS_F	this paper	PCR primers	ACAAGGCGGCCGCAGGTATGTCCGGACGTAAGAAATCC
sequence-based reagent	Rab7CDS_R	this paper	PCR primers	TCTAGAGGTACCTTAGCACTGACAGTTGTCAGGA
commercial assay or kit	Gibson Assembly kit	New England BioLabs	Cat# E5510S	
commercial assay or kit	Durcupan ACM	Sigma-Aldrich	Cat# 44610	
software, algorithm	Photoshop CS5 Extended 12.1 x64	Adobe	RRID:SCR_014199	

software, algorithm	Prism 9.4.1	GraphPad	RRID:SCR_002798	
software, algorithm	Zeiss Efficient Navigation 2	Zeiss	RRID:SCR_021725	
software, algorithm	cellSens Dimension 4.1	Olympus	RRID:SCR_014551	
software, algorithm	ImageJ 1.50b Fiji	National Institutes of Health, USA	RRID:SCR_003070	
software, algorithm	iTEM	Olympus		
other	Hoechst 33342	Thermo Fisher	Cat# 62249	(5 µg/ml)
other	jetOPTIMUS ® DNA Transfection Reagent	Polyplus	Cat# 101000051	
other	Insect-XPRESS™ Protein-free Insect Cell Medium with L-glutamine	Lonza	Cat# 12-730Q	
other	complete protease inhibitor cocktail	Roche	Cat# COEDTAF-RO	
other	anti-HA agarose (Mouse monoclonal)	Millipore	Cat# A2095	
other	anti-FLAG agarose (Mouse monoclonal)	Millipore	Cat# A2220	

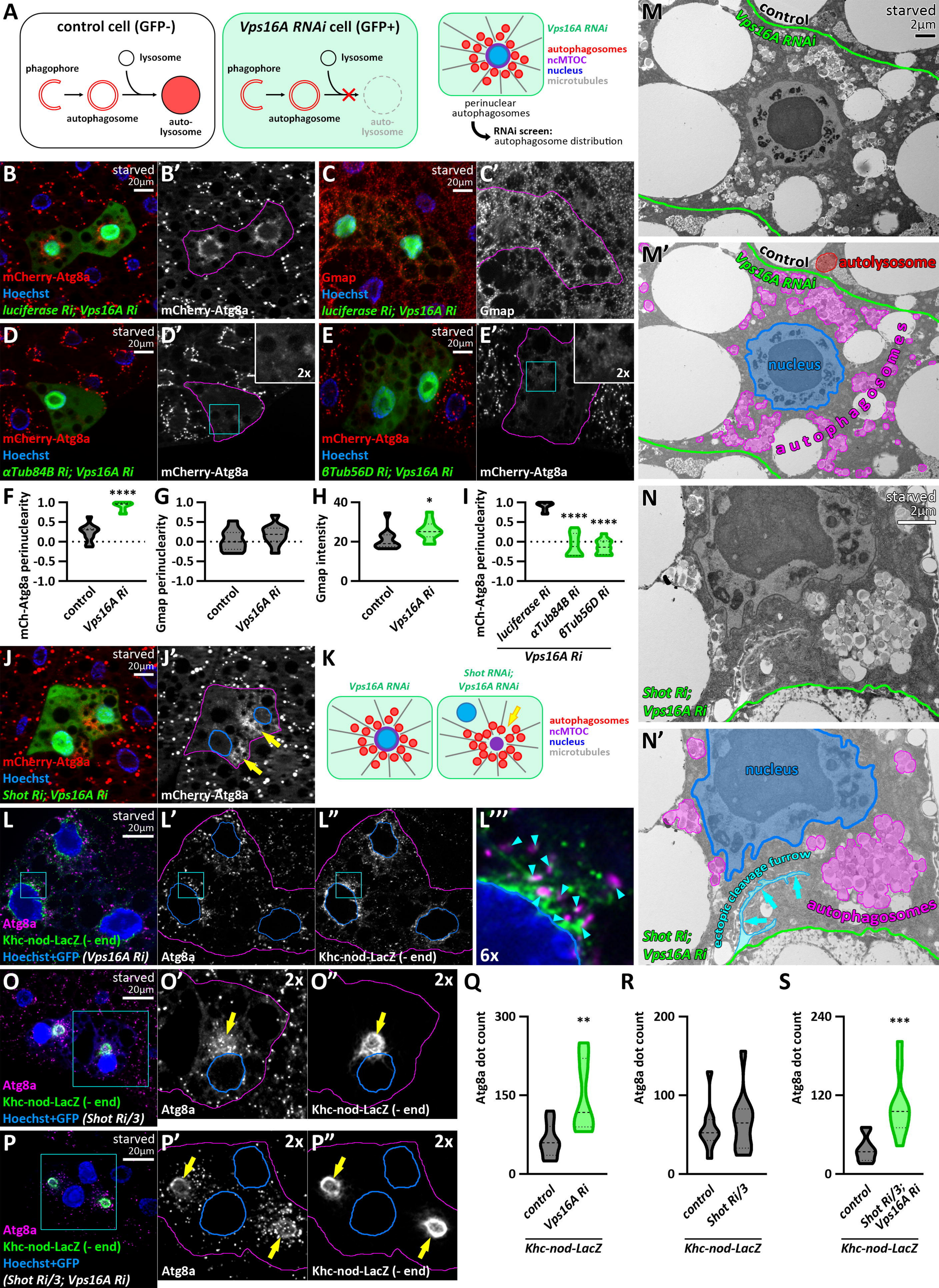
A
control cell (GFP-)
phagophore
lysosome
autophagosome
auto-lysosome
Vps16A RNAi cell (GFP+)
phagophore
lysosome
autophagosome
auto-lysosome
Vps16A RNAi
autophagosomes
ncMTOC
nucleus
microtubules
perinuclear autophagosomes
RNAi screen: autophagosome distribution
B starved 20µm mCherry-Atg8a Hoechst luciferase Ri; Vps16A Ri
B' mCherry-Atg8a
C starved 20µm Gmap Hoechst luciferase Ri; Vps16A Ri
C' Gmap
D starved 20µm mCherry-Atg8a Hoechst αTub84B Ri; Vps16A Ri
D' 2x mCherry-Atg8a
E starved 20µm mCherry-Atg8a Hoechst βTub56D Ri; Vps16A Ri
E' 2x mCherry-Atg8a
F mCh-Atg8a perinuclearity **** control Vps16A Ri
G Gmap perinuclearity control Vps16A Ri
H Gmap intensity * control Vps16A Ri
I mCh-Atg8a perinuclearity **** **** luciferase Ri αTub84B Ri βTub56D Ri Vps16A Ri
J starved 20µm mCherry-Atg8a Hoechst Shot Ri; Vps16A Ri
J' mCherry-Atg8a
K Vps16A RNAi Shot RNAi; Vps16A RNAi autophagosomes ncMTOC nucleus microtubules
L starved 20µm Atg8a Khc-nod-LacZ (- end) Hoechst+GFP (Vps16A Ri)
L' Atg8a
L'' Khc-nod-LacZ (- end)
L''' 6x
M control Vps16A RNAi starved 2µm
M' control Vps16A RNAi autolysosome nucleus autophagosomes
N starved 2µm Shot Ri; Vps16A Ri
N' nucleus ectopic cleavage furrow autophagosomes Shot Ri; Vps16A Ri
O starved 20µm Atg8a Khc-nod-LacZ (- end) Hoechst+GFP (Shot Ri/3)
O' 2x Atg8a
O'' 2x Khc-nod-LacZ (- end)
P starved 20µm Atg8a Khc-nod-LacZ (- end) Hoechst+GFP (Shot Ri/3; Vps16A Ri)
P' 2x Atg8a
P'' 2x Khc-nod-LacZ (- end)
Q Atg8a dot count ** control Vps16A Ri Khc-nod-LacZ
R Atg8a dot count control Shot Ri/3 Khc-nod-LacZ
S Atg8a dot count *** control Shot Ri/3; Vps16A Ri Khc-nod-LacZ

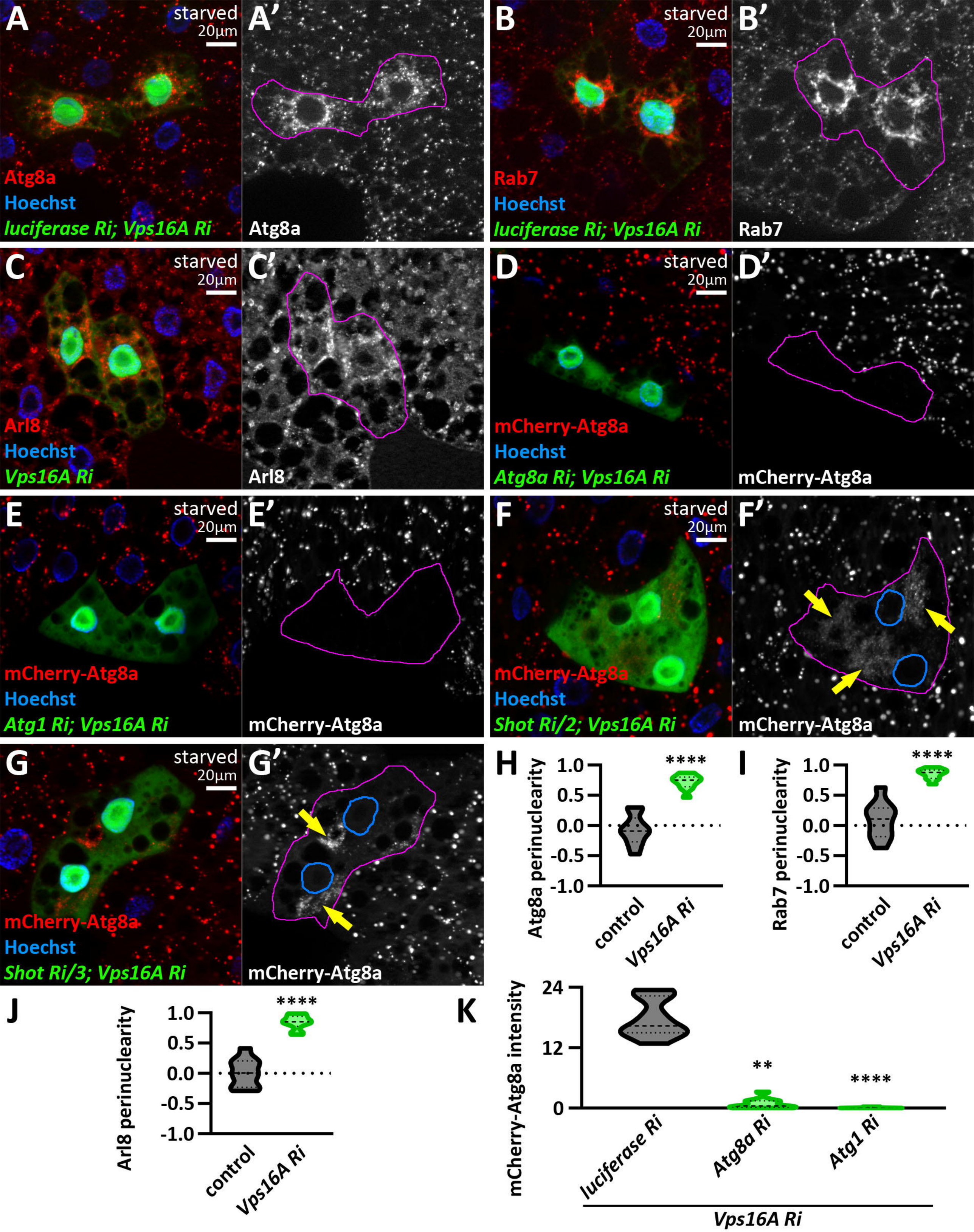
A
starved
20µm
Atg8a
Hoechst
luciferase Ri; Vps16A Ri
A'
Atg8a
B
starved
20µm
Rab7
Hoechst
luciferase Ri; Vps16A Ri
B'
Rab7
C
starved
20µm
Arl8
Hoechst
Vps16A Ri
C'
Arl8
D
starved
20µm
mCherry-Atg8a
Hoechst
Atg8a Ri; Vps16A Ri
D'
mCherry-Atg8a
E
starved
20µm
mCherry-Atg8a
Hoechst
Atg1 Ri; Vps16A Ri
E'
mCherry-Atg8a
F
starved
20µm
mCherry-Atg8a
Hoechst
Shot Ri/2; Vps16A Ri
F'
mCherry-Atg8a
G
starved
20µm
mCherry-Atg8a
Hoechst
Shot Ri/3; Vps16A Ri
G'
mCherry-Atg8a
H
Atg8a perinuclearity
1.0
0.5
0.0
-0.5
-1.0
****
control
Vps16A Ri
I
Rab7 perinuclearity
1.0
0.5
0.0
-0.5
-1.0
****
control
Vps16A Ri
J
Arl8 perinuclearity
1.0
0.5
0.0
-0.5
-1.0
****
control
Vps16A Ri
K
mCherry-Atg8a intensity
24
12
0
**
****
luciferase Ri
Atg8a Ri
Atg1 Ri
Vps16A Ri

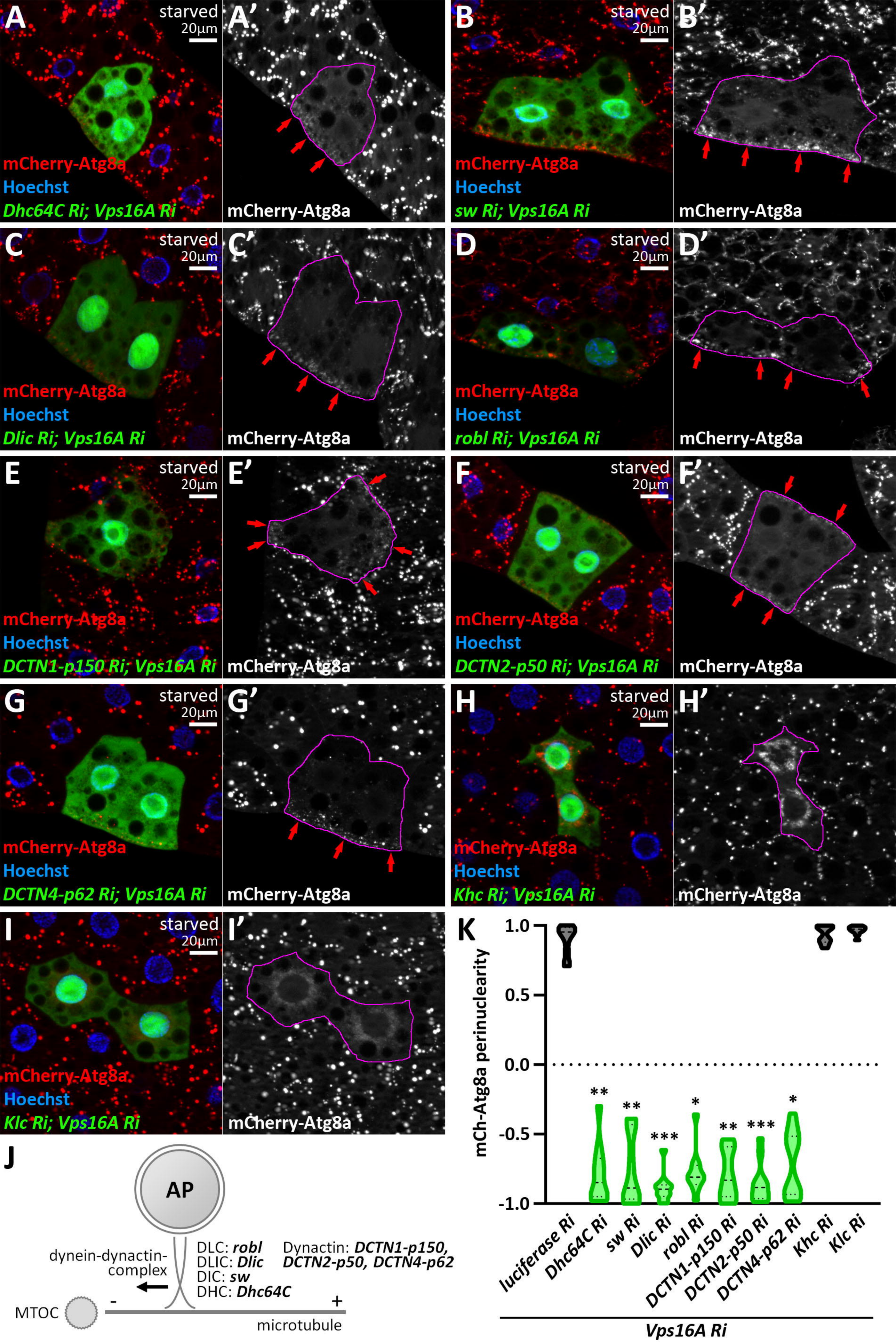
A
starved
20µm
mCherry-Atg8a
Hoechst
Dhc64C Ri; Vps16A Ri
A'
mCherry-Atg8a
B
starved
20µm
mCherry-Atg8a
Hoechst
sw Ri; Vps16A Ri
B'
mCherry-Atg8a
C
starved
20µm
mCherry-Atg8a
Hoechst
Dlic Ri; Vps16A Ri
C'
mCherry-Atg8a
D
starved
20µm
mCherry-Atg8a
Hoechst
robl Ri; Vps16A Ri
D'
mCherry-Atg8a
E
starved
20µm
mCherry-Atg8a
Hoechst
DCTN1-p150 Ri; Vps16A Ri
E'
mCherry-Atg8a
F
starved
20µm
mCherry-Atg8a
Hoechst
DCTN2-p50 Ri; Vps16A Ri
F'
mCherry-Atg8a
G
starved
20µm
mCherry-Atg8a
Hoechst
DCTN4-p62 Ri; Vps16A Ri
G'
mCherry-Atg8a
H
starved
20µm
mCherry-Atg8a
Hoechst
Khc Ri; Vps16A Ri
H'
mCherry-Atg8a
I
starved
20µm
mCherry-Atg8a
Hoechst
Klc Ri; Vps16A Ri
I'
mCherry-Atg8a
J
AP
dynein-dynactin-complex
DLC: robl
DLIC: Dlic
DIC: sw
DHC: Dhc64C
Dynactin: DCTN1-p150, DCTN2-p50, DCTN4-p62
MTOC
-
+
microtubule
K
mCh-Atg8a perinuclearity
1.0
0.5
0.0
-0.5
-1.0
**
**
***
*
**
***
*
luciferase Ri
Dhc64C Ri
sw Ri
Dlic Ri
robl Ri
DCTN1-p150 Ri
DCTN2-p50 Ri
DCTN4-p62 Ri
Khc Ri
Klc Ri
Vps16A Ri

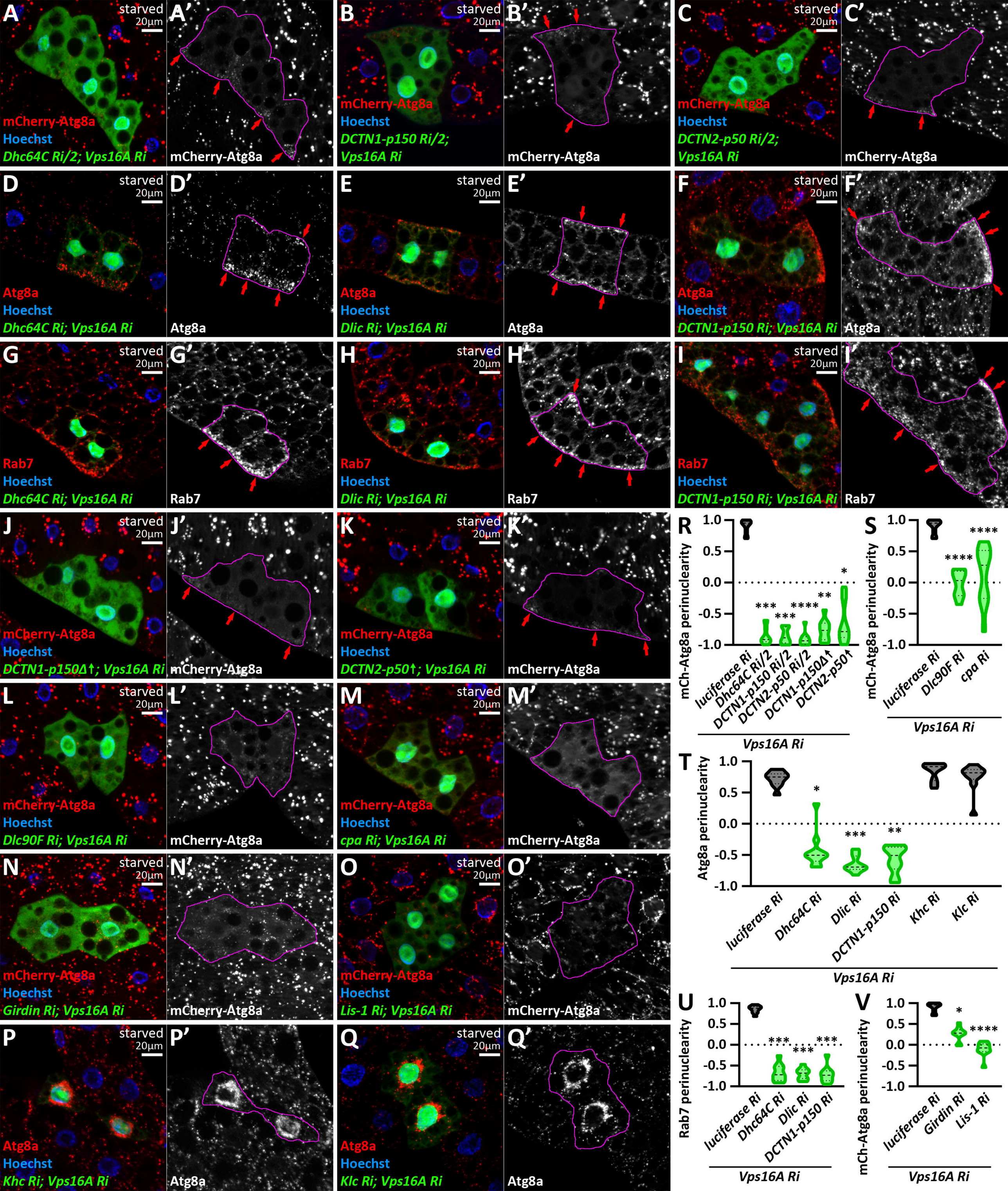
A
starved
20µm
mCherry-Atg8a
Hoechst
Dhc64C Ri/2; Vps16A Ri
A'
mCherry-Atg8a
B
starved
20µm
mCherry-Atg8a
Hoechst
DCTN1-p150 Ri/2;
Vps16A Ri
B'
mCherry-Atg8a
C
starved
20µm
mCherry-Atg8a
Hoechst
DCTN2-p50 Ri/2;
Vps16A Ri
C'
mCherry-Atg8a
D
starved
20µm
Atg8a
Hoechst
Dhc64C Ri; Vps16A Ri
D'
Atg8a
E
starved
20µm
Atg8a
Hoechst
Dlic Ri; Vps16A Ri
E'
Atg8a
F
starved
20µm
Atg8a
Hoechst
DCTN1-p150 Ri; Vps16A Ri
F'
Atg8a
G
starved
20µm
Rab7
Hoechst
Dhc64C Ri; Vps16A Ri
G'
Rab7
H
starved
20µm
Rab7
Hoechst
Dlic Ri; Vps16A Ri
H'
Rab7
I
starved
20µm
Rab7
Hoechst
DCTN1-p150 Ri; Vps16A Ri
I'
Rab7
J
starved
20µm
mCherry-Atg8a
Hoechst
DCTN1-p150Δ↑; Vps16A Ri
J'
mCherry-Atg8a
K
starved
20µm
mCherry-Atg8a
Hoechst
DCTN2-p50↑; Vps16A Ri
K'
mCherry-Atg8a
L
starved
20µm
mCherry-Atg8a
Hoechst
Dlc90F Ri; Vps16A Ri
L'
mCherry-Atg8a
M
starved
20µm
mCherry-Atg8a
Hoechst
cpa Ri; Vps16A Ri
M'
mCherry-Atg8a
N
starved
20µm
mCherry-Atg8a
Hoechst
Girdin Ri; Vps16A Ri
N'
mCherry-Atg8a
O
starved
20µm
mCherry-Atg8a
Hoechst
Lis-1 Ri; Vps16A Ri
O'
mCherry-Atg8a
P
starved
20µm
Atg8a
Hoechst
Khc Ri; Vps16A Ri
P'
Atg8a
Q
starved
20µm
Atg8a
Hoechst
Klc Ri; Vps16A Ri
Q'
Atg8a
R
mCh-Atg8a perinuclearity
1.0
0.5
0.0
-0.5
-1.0
luciferase Ri
Dhc64C Ri/2
DCTN1-p150 Ri/2
DCTN2-p50 Ri/2
DCTN1-p150Δ↑
DCTN2-p50↑
Vps16A Ri
S
mCh-Atg8a perinuclearity
luciferase Ri
Dlc90F Ri
cpa Ri
Vps16A Ri
T
Atg8a perinuclearity
luciferase Ri
Dhc64C Ri
Dlic Ri
DCTN1-p150 Ri
Khc Ri
Klc Ri
Vps16A Ri
U
Rab7 perinuclearity
luciferase Ri
Dhc64C Ri
Dlic Ri
DCTN1-p150 Ri
Vps16A Ri
V
mCh-Atg8a perinuclearity
luciferase Ri
Girdin Ri
Lis-1 Ri
Vps16A Ri

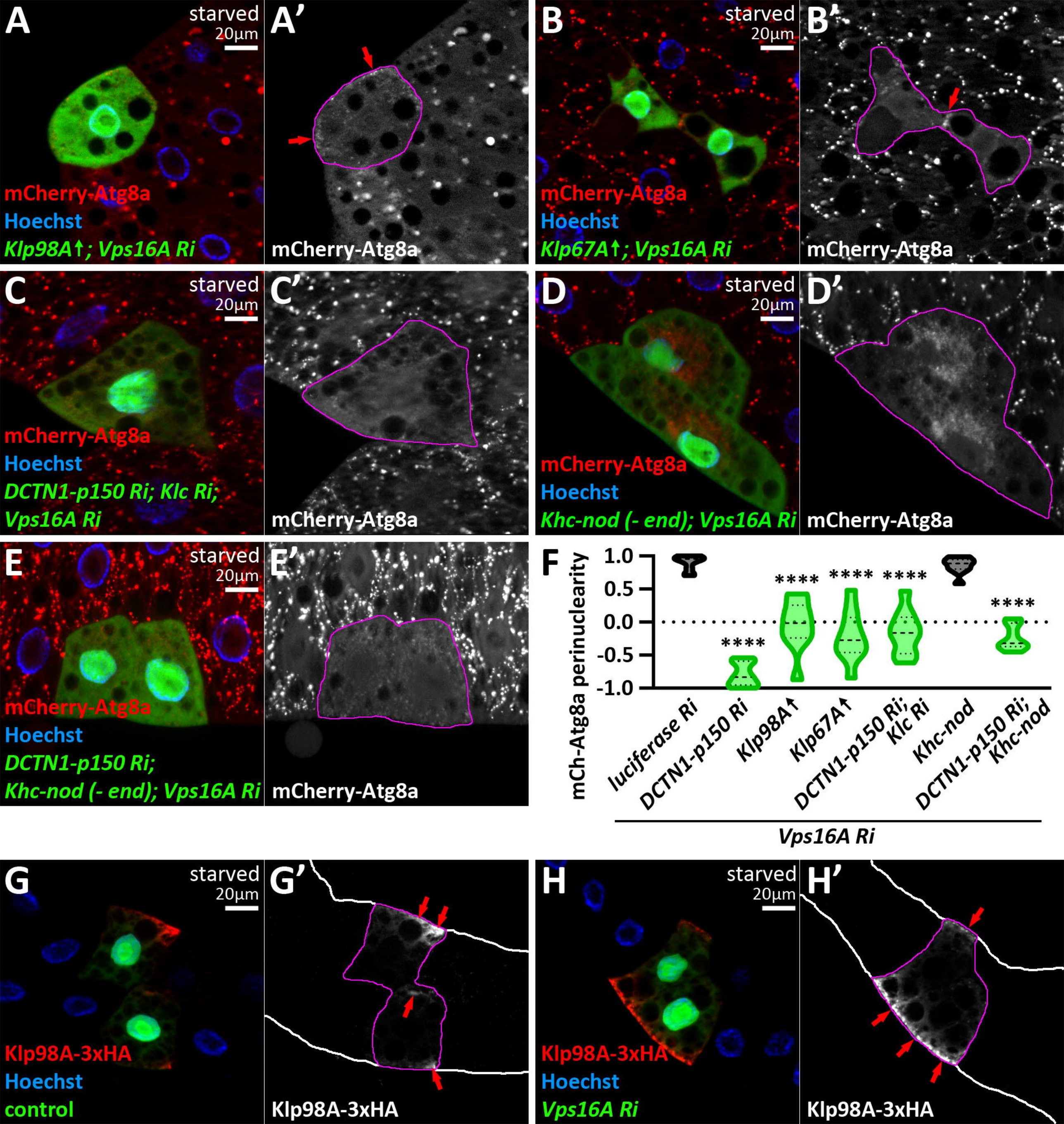
A
starved
20µm
mCherry-Atg8a
Hoechst
Klp98A↑; Vps16A Ri
A'
mCherry-Atg8a
B
starved
20µm
mCherry-Atg8a
Hoechst
Klp67A↑; Vps16A Ri
B'
mCherry-Atg8a
C
starved
20µm
mCherry-Atg8a
Hoechst
DCTN1-p150 Ri; Klc Ri;
Vps16A Ri
C'
mCherry-Atg8a
D
starved
20µm
mCherry-Atg8a
Hoechst
Khc-nod (- end); Vps16A Ri
D'
mCherry-Atg8a
E
starved
20µm
mCherry-Atg8a
Hoechst
DCTN1-p150 Ri;
Khc-nod (- end); Vps16A Ri
E'
mCherry-Atg8a
F
mCh-Atg8a perinuclearity
1.0
0.5
0.0
-0.5
-1.0
****
****
****
****
****
luciferase Ri
DCTN1-p150 Ri
Klp98A↑
Klp67A↑
DCTN1-p150 Ri; Klc Ri
Khc-nod
DCTN1-p150 Ri; Khc-nod
Vps16A Ri
G
starved
20µm
Klp98A-3xHA
Hoechst
control
G'
Klp98A-3xHA
H
starved
20µm
Klp98A-3xHA
Hoechst
Vps16A Ri
H'
Klp98A-3xHA

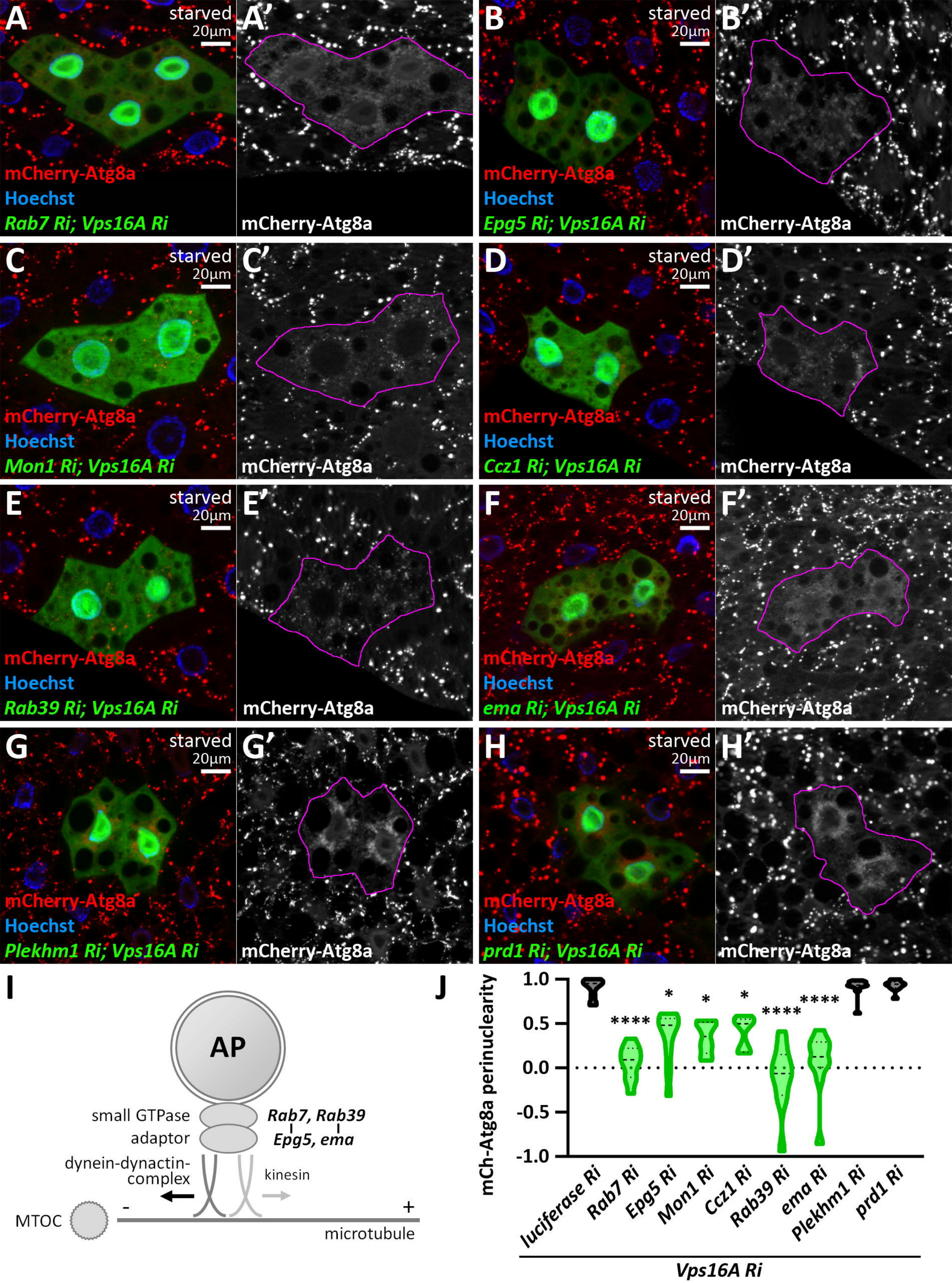
A
starved
20µm
mCherry-Atg8a
Hoechst
Rab7 Ri; Vps16A Ri
A'
mCherry-Atg8a
B
starved
20µm
mCherry-Atg8a
Hoechst
Epg5 Ri; Vps16A Ri
B'
mCherry-Atg8a
C
starved
20µm
mCherry-Atg8a
Hoechst
Mon1 Ri; Vps16A Ri
C'
mCherry-Atg8a
D
starved
20µm
mCherry-Atg8a
Hoechst
Ccz1 Ri; Vps16A Ri
D'
mCherry-Atg8a
E
starved
20µm
mCherry-Atg8a
Hoechst
Rab39 Ri; Vps16A Ri
E'
mCherry-Atg8a
F
starved
20µm
mCherry-Atg8a
Hoechst
ema Ri; Vps16A Ri
F'
mCherry-Atg8a
G
starved
20µm
mCherry-Atg8a
Hoechst
Plekhm1 Ri; Vps16A Ri
G'
mCherry-Atg8a
H
starved
20µm
mCherry-Atg8a
Hoechst
prd1 Ri; Vps16A Ri
H'
mCherry-Atg8a
I
AP
small GTPase
adaptor
Rab7, Rab39
Epg5, ema
dynein-dynactin-complex
kinesin
MTOC
-
+
microtubule
J
mCh-Atg8a perinuclearity
1.0
0.5
0.0
-0.5
-1.0
****
*
*
*
****
****
luciferase Ri
Rab7 Ri
Epg5 Ri
Mon1 Ri
Ccz1 Ri
Rab39 Ri
ema Ri
Plekhm1 Ri
prd1 Ri
Vps16A Ri

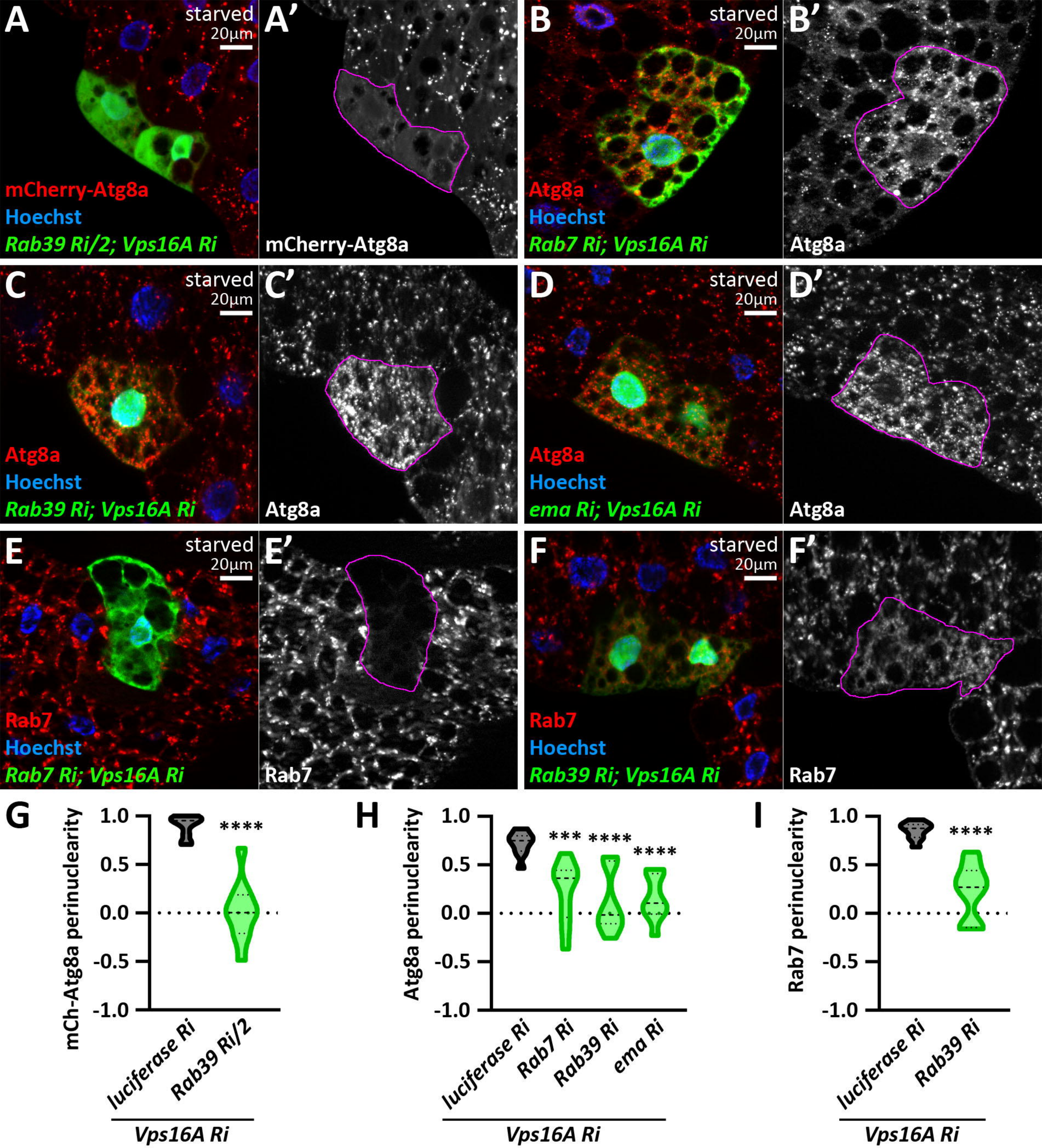
A
starved
20µm
mCherry-Atg8a
Hoechst
Rab39 Ri/2; Vps16A Ri
A'
mCherry-Atg8a
B
starved
20µm
Atg8a
Hoechst
Rab7 Ri; Vps16A Ri
B'
Atg8a
C
starved
20µm
Atg8a
Hoechst
Rab39 Ri; Vps16A Ri
C'
Atg8a
D
starved
20µm
Atg8a
Hoechst
ema Ri; Vps16A Ri
D'
Atg8a
E
starved
20µm
Rab7
Hoechst
Rab7 Ri; Vps16A Ri
E'
Rab7
F
starved
20µm
Rab7
Hoechst
Rab39 Ri; Vps16A Ri
F'
Rab7
G
mCh-Atg8a perinuclearity
1.0
0.5
0.0
-0.5
-1.0
****
luciferase Ri
Rab39 Ri/2
Vps16A Ri
H
Atg8a perinuclearity
1.0
0.5
0.0
-0.5
-1.0
***
****
****
luciferase Ri
Rab7 Ri
Rab39 Ri
ema Ri
Vps16A Ri
I
Rab7 perinuclearity
1.0
0.5
0.0
-0.5
-1.0
****
luciferase Ri
Rab39 Ri
Vps16A Ri

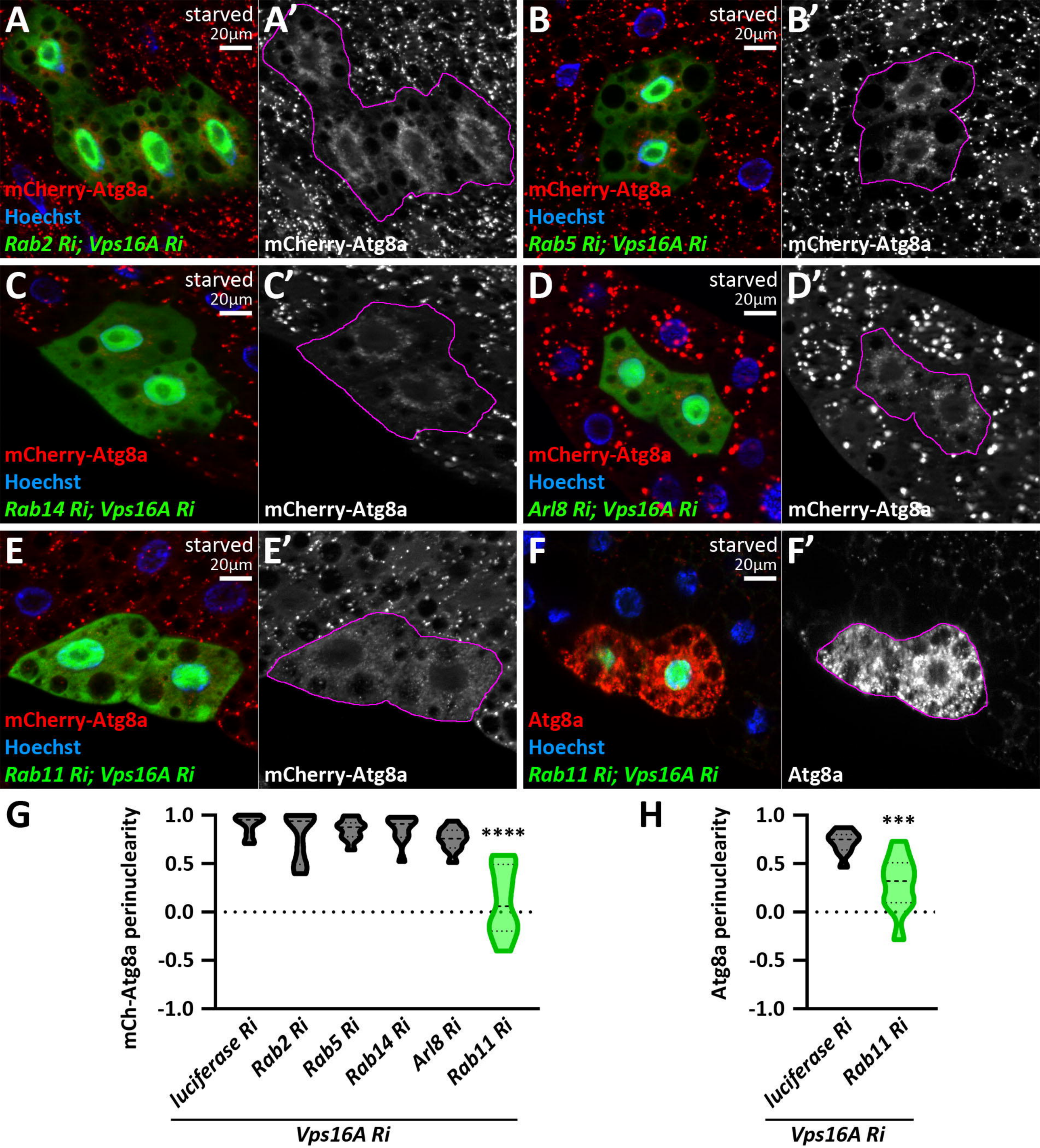
A
starved
20µm
mCherry-Atg8a
Hoechst
Rab2 Ri; Vps16A Ri
A'
mCherry-Atg8a
B
starved
20µm
mCherry-Atg8a
Hoechst
Rab5 Ri; Vps16A Ri
B'
mCherry-Atg8a
C
starved
20µm
mCherry-Atg8a
Hoechst
Rab14 Ri; Vps16A Ri
C'
mCherry-Atg8a
D
starved
20µm
mCherry-Atg8a
Hoechst
Arl8 Ri; Vps16A Ri
D'
mCherry-Atg8a
E
starved
20µm
mCherry-Atg8a
Hoechst
Rab11 Ri; Vps16A Ri
E'
mCherry-Atg8a
F
starved
20µm
Atg8a
Hoechst
Rab11 Ri; Vps16A Ri
F'
Atg8a
G
mCh-Atg8a perinuclearity
1.0
0.5
0.0
-0.5
-1.0
****
luciferase Ri
Rab2 Ri
Rab5 Ri
Rab14 Ri
Arl8 Ri
Rab11 Ri
Vps16A Ri
H
Atg8a perinuclearity
1.0
0.5
0.0
-0.5
-1.0
***
luciferase Ri
Rab11 Ri
Vps16A Ri

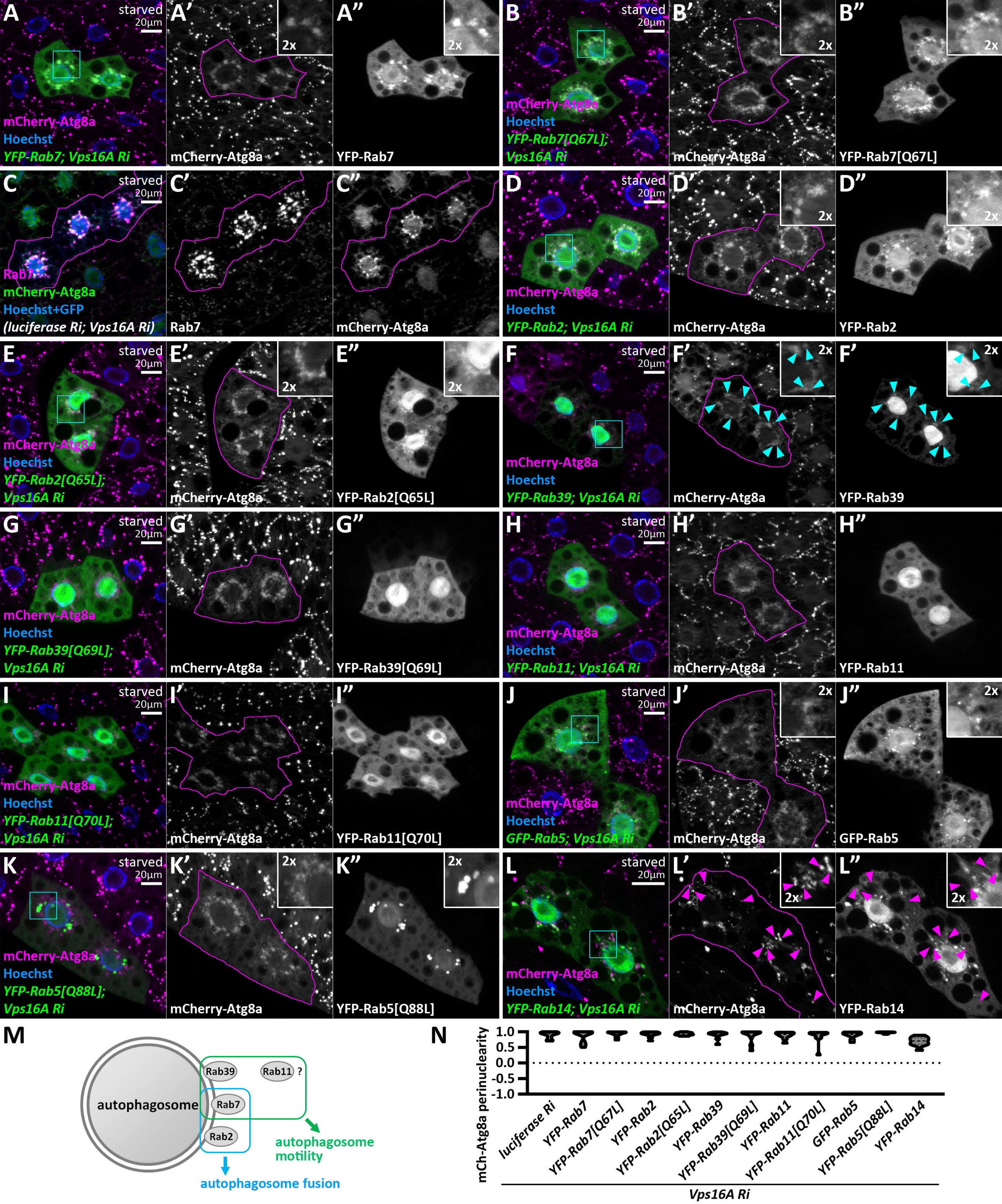
A
starved
20µm
mCherry-Atg8a
Hoechst
YFP-Rab7; Vps16A Ri
A'
2x
mCherry-Atg8a
A''
2x
YFP-Rab7
B
starved
20µm
mCherry-Atg8a
Hoechst
YFP-Rab7[Q67L];
Vps16A Ri
B'
2x
mCherry-Atg8a
B''
2x
YFP-Rab7[Q67L]
C
starved
20µm
Rab7
mCherry-Atg8a
Hoechst+GFP
(luciferase Ri; Vps16A Ri)
C'
Rab7
C''
mCherry-Atg8a
D
starved
20µm
mCherry-Atg8a
Hoechst
YFP-Rab2; Vps16A Ri
D'
2x
mCherry-Atg8a
D''
2x
YFP-Rab2
E
starved
20µm
mCherry-Atg8a
Hoechst
YFP-Rab2[Q65L];
Vps16A Ri
E'
2x
mCherry-Atg8a
E''
2x
YFP-Rab2[Q65L]
F
starved
20µm
mCherry-Atg8a
Hoechst
YFP-Rab39; Vps16A Ri
F'
2x
mCherry-Atg8a
F'
2x
YFP-Rab39
G
starved
20µm
mCherry-Atg8a
Hoechst
YFP-Rab39[Q69L];
Vps16A Ri
G'
mCherry-Atg8a
G''
YFP-Rab39[Q69L]
H
starved
20µm
mCherry-Atg8a
Hoechst
YFP-Rab11; Vps16A Ri
H'
mCherry-Atg8a
H''
YFP-Rab11
I
starved
20µm
mCherry-Atg8a
Hoechst
YFP-Rab11[Q70L];
Vps16A Ri
I'
mCherry-Atg8a
I''
YFP-Rab11[Q70L]
J
starved
20µm
mCherry-Atg8a
Hoechst
GFP-Rab5; Vps16A Ri
J'
2x
mCherry-Atg8a
J''
2x
GFP-Rab5
K
starved
20µm
mCherry-Atg8a
Hoechst
YFP-Rab5[Q88L];
Vps16A Ri
K'
2x
mCherry-Atg8a
K''
2x
YFP-Rab5[Q88L]
L
starved
20µm
mCherry-Atg8a
Hoechst
YFP-Rab14; Vps16A Ri
L'
2x
mCherry-Atg8a
L''
2x
YFP-Rab14
M
autophagosome
Rab39
Rab11 ?
Rab7
Rab2
autophagosome motility
autophagosome fusion
N
mCh-Atg8a perinuclearity
1.0
0.5
0.0
-0.5
-1.0
luciferase Ri
YFP-Rab7
YFP-Rab7[Q67L]
YFP-Rab2
YFP-Rab2[Q65L]
YFP-Rab39
YFP-Rab39[Q69L]
YFP-Rab11
YFP-Rab11[Q70L]
GFP-Rab5
YFP-Rab5[Q88L]
YFP-Rab14
Vps16A Ri

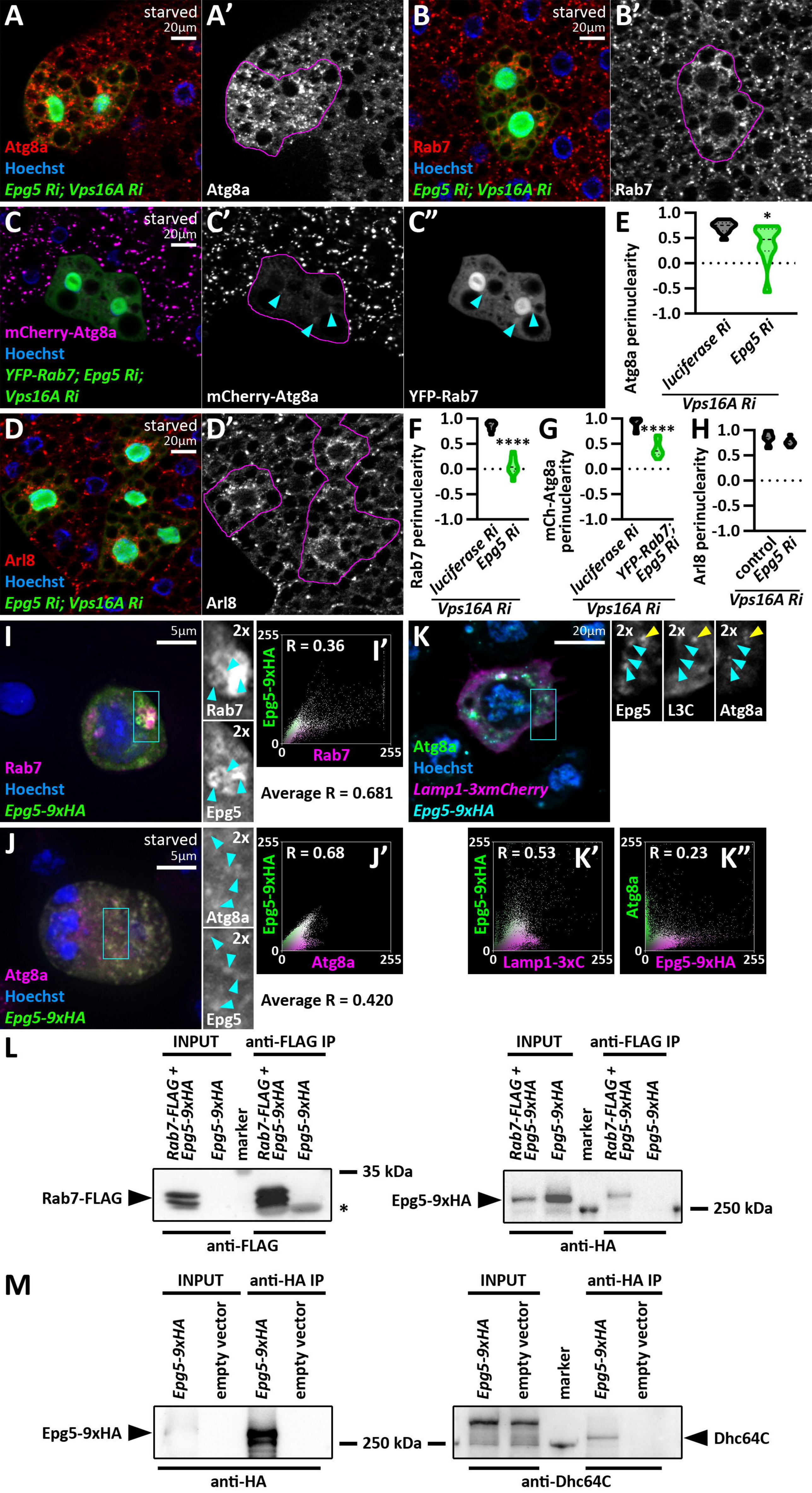
A
starved
20µm
Atg8a
Hoechst
Epg5 Ri; Vps16A Ri
A'
Atg8a
B
starved
20µm
Rab7
Hoechst
Epg5 Ri; Vps16A Ri
B'
Rab7
C
starved
20µm
mCherry-Atg8a
Hoechst
YFP-Rab7; Epg5 Ri;
Vps16A Ri
C'
mCherry-Atg8a
C''
YFP-Rab7
E
Atg8a perinuclearity
1.0
0.5
0.0
-0.5
-1.0
*
luciferase Ri
Epg5 Ri
Vps16A Ri
D
starved
20µm
Arl8
Hoechst
Epg5 Ri; Vps16A Ri
D'
Arl8
F
Rab7 perinuclearity
****
luciferase Ri
Epg5 Ri
Vps16A Ri
G
mCh-Atg8a perinuclearity
****
luciferase Ri
YFP-Rab7; Epg5 Ri
Vps16A Ri
H
Arl8 perinuclearity
control
Epg5 Ri
Vps16A Ri
I
5µm
Rab7
Hoechst
Epg5-9xHA
2x
Rab7
2x
Epg5
I'
R = 0.36
Epg5-9xHA
Rab7
255
0
Average R = 0.681
K
20µm
Atg8a
Hoechst
Lamp1-3xmCherry
Epg5-9xHA
2x
Epg5
2x
L3C
2x
Atg8a
J
starved
5µm
Atg8a
Hoechst
Epg5-9xHA
2x
Atg8a
2x
Epg5
J'
R = 0.68
Epg5-9xHA
Atg8a
255
0
Average R = 0.420
K'
R = 0.53
Epg5-9xHA
Lamp1-3xC
K''
R = 0.23
Atg8a
Epg5-9xHA
L
INPUT
anti-FLAG IP
Rab7-FLAG + Epg5-9xHA
Epg5-9xHA
marker
Rab7-FLAG + Epg5-9xHA
Epg5-9xHA
Rab7-FLAG
35 kDa
*
anti-FLAG
INPUT
anti-FLAG IP
Rab7-FLAG + Epg5-9xHA
Epg5-9xHA
marker
Rab7-FLAG + Epg5-9xHA
Epg5-9xHA
Epg5-9xHA
250 kDa
anti-HA
M
INPUT
anti-HA IP
Epg5-9xHA
empty vector
Epg5-9xHA
empty vector
Epg5-9xHA
250 kDa
anti-HA
INPUT
anti-HA IP
Epg5-9xHA
empty vector
marker
Epg5-9xHA
empty vector
Dhc64C
anti-Dhc64C

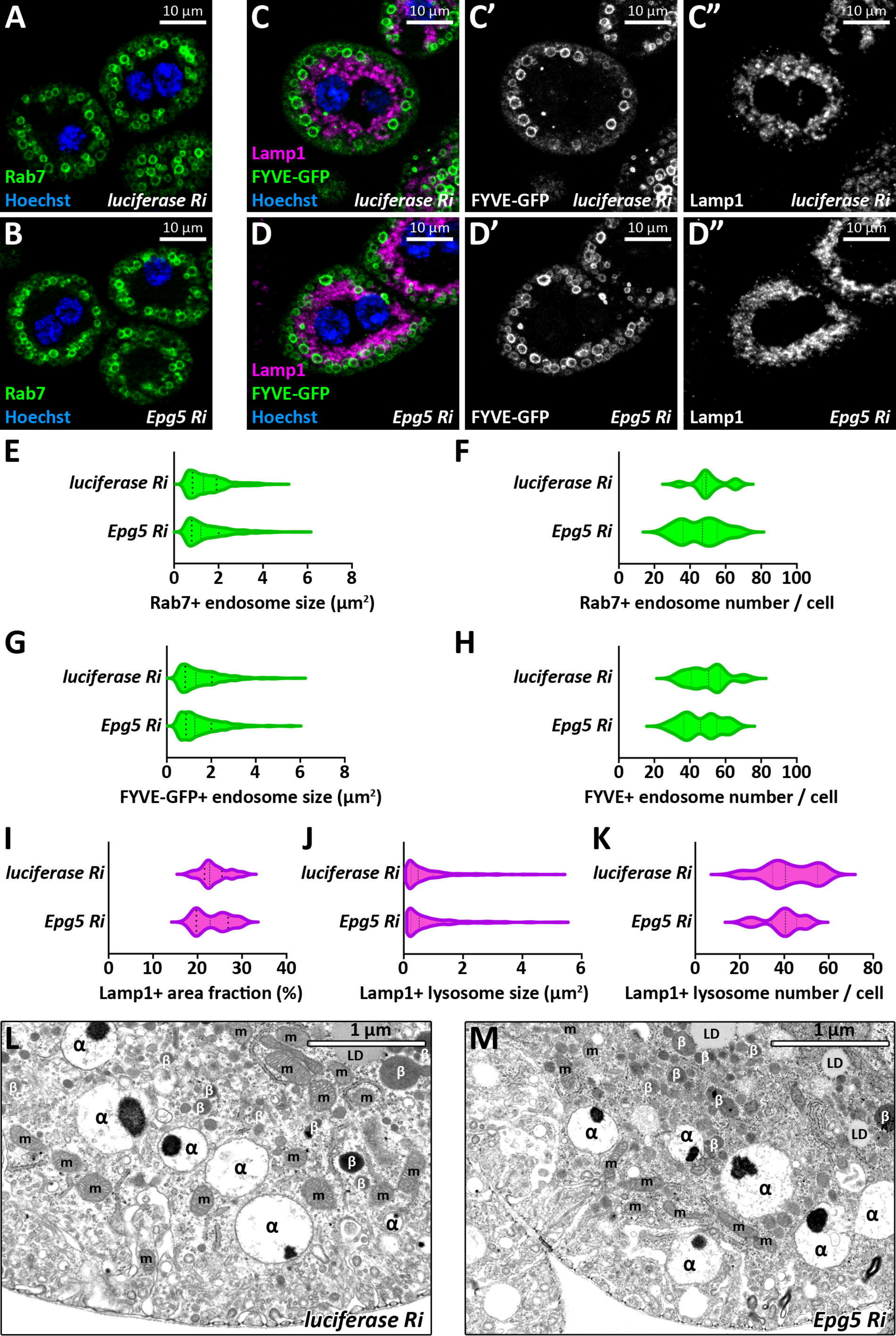
A
10 µm
Rab7
Hoechst
luciferase Ri
B
10 µm
Rab7
Hoechst
Epg5 Ri
C
10 µm
Lamp1
FYVE-GFP
Hoechst
luciferase Ri
C'
10 µm
FYVE-GFP
luciferase Ri
C''
10 µm
Lamp1
luciferase Ri
D
10 µm
Lamp1
FYVE-GFP
Hoechst
Epg5 Ri
D'
10 µm
FYVE-GFP
Epg5 Ri
D''
10 µm
Lamp1
Epg5 Ri
E
luciferase Ri
Epg5 Ri
0 2 4 6 8
Rab7+ endosome size (µm²)
F
luciferase Ri
Epg5 Ri
0 20 40 60 80 100
Rab7+ endosome number / cell
G
luciferase Ri
Epg5 Ri
0 2 4 6 8
FYVE-GFP+ endosome size (µm²)
H
luciferase Ri
Epg5 Ri
0 20 40 60 80 100
FYVE+ endosome number / cell
I
luciferase Ri
Epg5 Ri
0 10 20 30 40
Lamp1+ area fraction (%)
J
luciferase Ri
Epg5 Ri
0 2 4 6
Lamp1+ lysosome size (µm²)
K
luciferase Ri
Epg5 Ri
0 20 40 60 80
Lamp1+ lysosome number / cell
L
1 µm
α
β
m
LD
luciferase Ri
M
1 µm
α
β
m
LD
Epg5 Ri

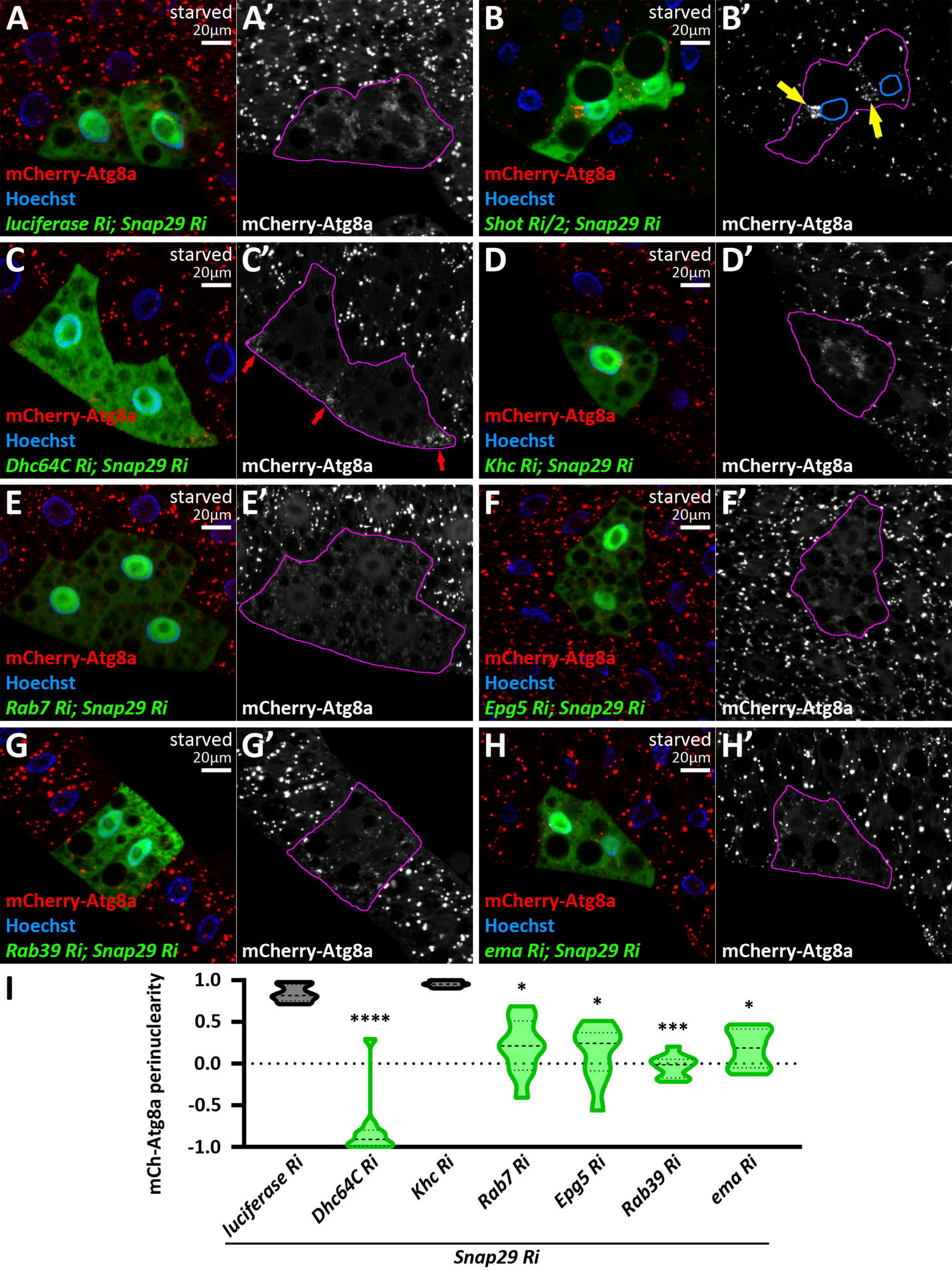
A
starved
20µm
mCherry-Atg8a
Hoechst
luciferase Ri; Snap29 Ri
A'
mCherry-Atg8a
B
starved
20µm
mCherry-Atg8a
Hoechst
Shot Ri/2; Snap29 Ri
B'
mCherry-Atg8a
C
starved
20µm
mCherry-Atg8a
Hoechst
Dhc64C Ri; Snap29 Ri
C'
mCherry-Atg8a
D
starved
20µm
mCherry-Atg8a
Hoechst
Khc Ri; Snap29 Ri
D'
mCherry-Atg8a
E
starved
20µm
mCherry-Atg8a
Hoechst
Rab7 Ri; Snap29 Ri
E'
mCherry-Atg8a
F
starved
20µm
mCherry-Atg8a
Hoechst
Epg5 Ri; Snap29 Ri
F'
mCherry-Atg8a
G
starved
20µm
mCherry-Atg8a
Hoechst
Rab39 Ri; Snap29 Ri
G'
mCherry-Atg8a
H
starved
20µm
mCherry-Atg8a
Hoechst
ema Ri; Snap29 Ri
H'
mCherry-Atg8a
I
mCh-Atg8a perinuclearity
1.0
0.5
0.0
-0.5
-1.0
****
*
*
***
*
luciferase Ri
Dhc64C Ri
Khc Ri
Rab7 Ri
Epg5 Ri
Rab39 Ri
ema Ri
Snap29 Ri

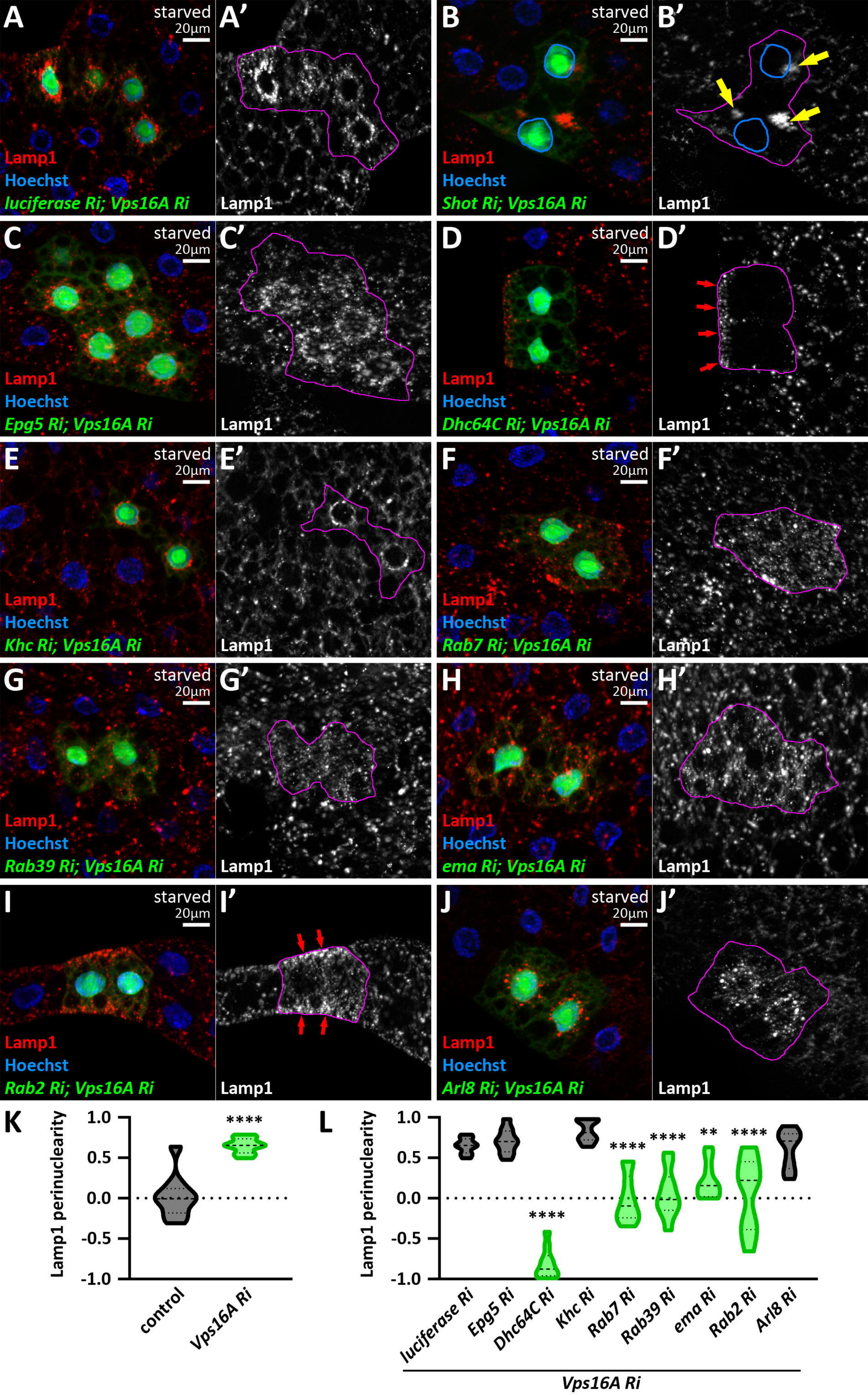
A
starved
20µm
Lamp1
Hoechst
luciferase Ri; Vps16A Ri
A'
Lamp1
B
starved
20µm
Lamp1
Hoechst
Shot Ri; Vps16A Ri
B'
Lamp1
C
starved
20µm
Lamp1
Hoechst
Epg5 Ri; Vps16A Ri
C'
Lamp1
D
starved
20µm
Lamp1
Hoechst
Dhc64C Ri; Vps16A Ri
D'
Lamp1
E
starved
20µm
Lamp1
Hoechst
Khc Ri; Vps16A Ri
E'
Lamp1
F
starved
20µm
Lamp1
Hoechst
Rab7 Ri; Vps16A Ri
F'
Lamp1
G
starved
20µm
Lamp1
Hoechst
Rab39 Ri; Vps16A Ri
G'
Lamp1
H
starved
20µm
Lamp1
Hoechst
ema Ri; Vps16A Ri
H'
Lamp1
I
starved
20µm
Lamp1
Hoechst
Rab2 Ri; Vps16A Ri
I'
Lamp1
J
starved
20µm
Lamp1
Hoechst
Arl8 Ri; Vps16A Ri
J'
Lamp1
K
Lamp1 perinuclearity
1.0
0.5
0.0
-0.5
-1.0
****
control
Vps16A Ri
L
Lamp1 perinuclearity
1.0
0.5
0.0
-0.5
-1.0
****
****
****
**
****
luciferase Ri
Epg5 Ri
Dhc64C Ri
Khc Ri
Rab7 Ri
Rab39 Ri
ema Ri
Rab2 Ri
Arl8 Ri
Vps16A Ri

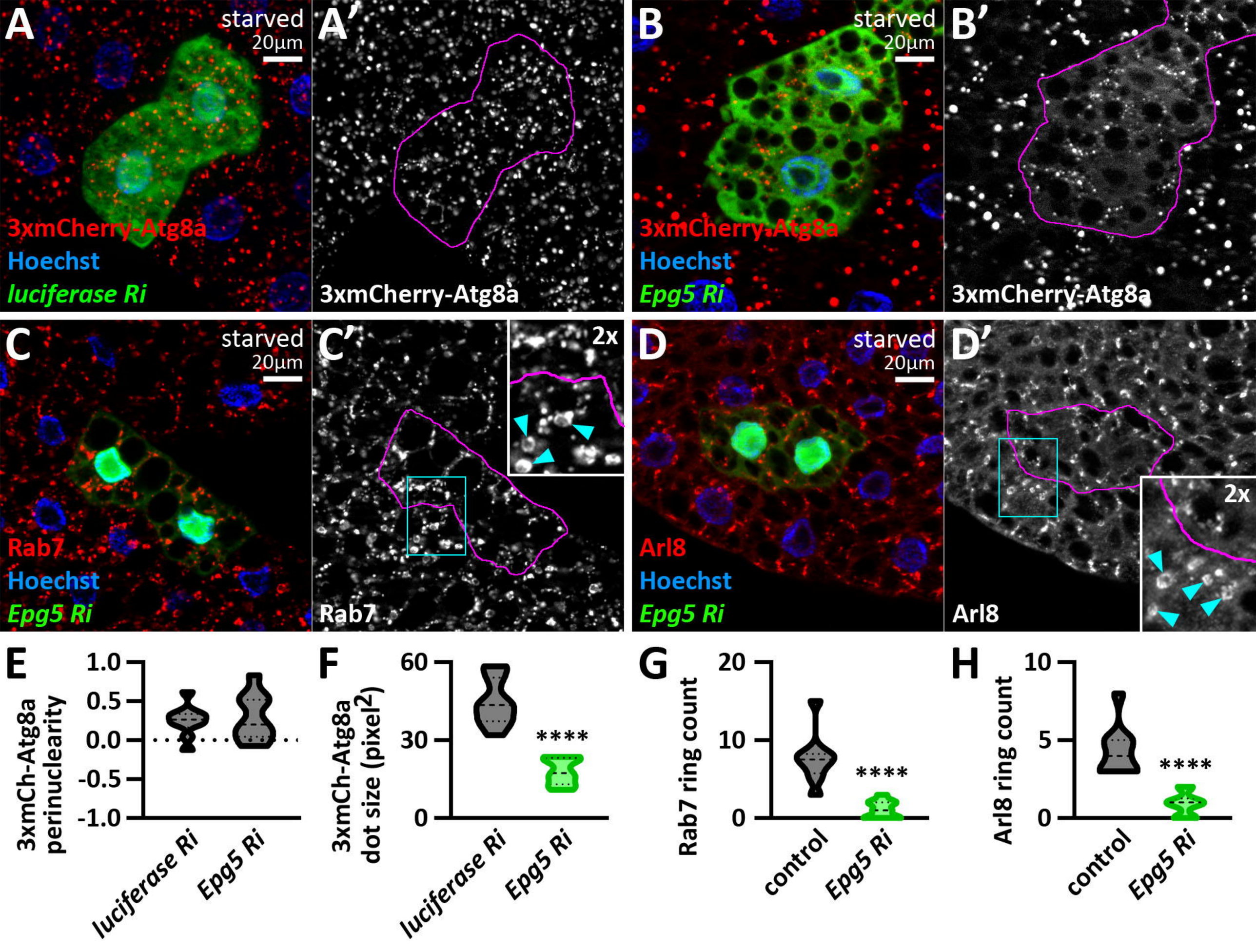
A
starved
20µm
3xmCherry-Atg8a
Hoechst
luciferase Ri
A'
3xmCherry-Atg8a
B
starved
20µm
3xmCherry-Atg8a
Hoechst
Epg5 Ri
B'
3xmCherry-Atg8a
C
starved
20µm
Rab7
Hoechst
Epg5 Ri
C'
2x
Rab7
D
starved
20µm
Arl8
Hoechst
Epg5 Ri
D'
2x
Arl8
E
3xmCh-Atg8a perinuclearity
1.0
0.5
0.0
-0.5
-1.0
luciferase Ri
Epg5 Ri
F
3xmCh-Atg8a dot size (pixel²)
60
30
0
****
luciferase Ri
Epg5 Ri
G
Rab7 ring count
20
10
0
****
control
Epg5 Ri
H
Arl8 ring count
10
5
0
****
control
Epg5 Ri

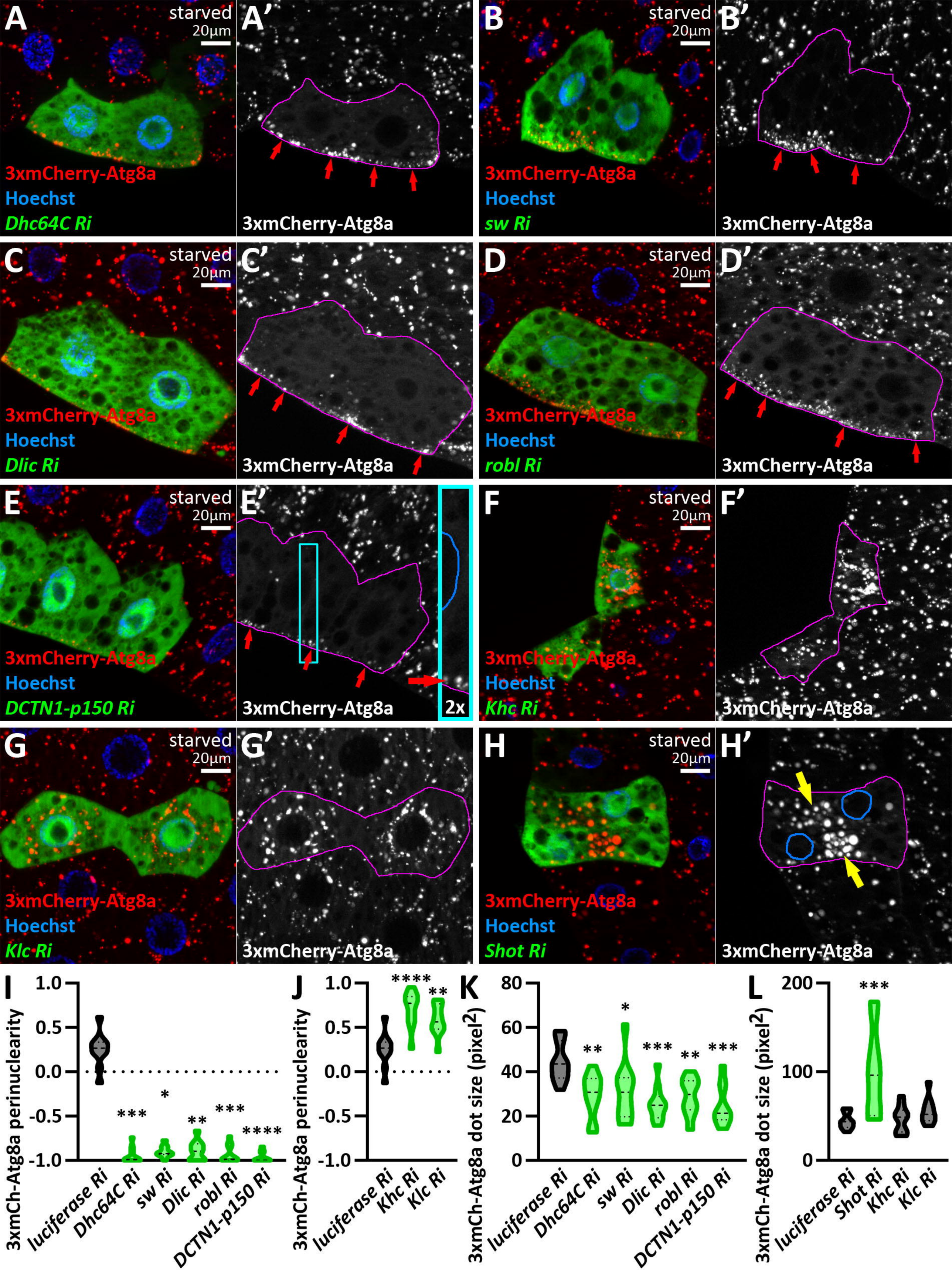
A
starved
20µm
3xmCherry-Atg8a
Hoechst
Dhc64C Ri
A'
3xmCherry-Atg8a
B
starved
20µm
3xmCherry-Atg8a
Hoechst
sw Ri
B'
3xmCherry-Atg8a
C
starved
20µm
3xmCherry-Atg8a
Hoechst
Dlic Ri
C'
3xmCherry-Atg8a
D
starved
20µm
3xmCherry-Atg8a
Hoechst
robl Ri
D'
3xmCherry-Atg8a
E
starved
20µm
3xmCherry-Atg8a
Hoechst
DCTN1-p150 Ri
E'
3xmCherry-Atg8a
2x
F
starved
20µm
3xmCherry-Atg8a
Hoechst
Khc Ri
F'
3xmCherry-Atg8a
G
starved
20µm
3xmCherry-Atg8a
Hoechst
Klc Ri
G'
3xmCherry-Atg8a
H
starved
20µm
3xmCherry-Atg8a
Hoechst
Shot Ri
H'
3xmCherry-Atg8a
I
3xmCh-Atg8a perinuclearity
1.0
0.5
0.0
-0.5
-1.0
***
*
**
***
****
luciferase Ri
Dhc64C Ri
sw Ri
Dlic Ri
robl Ri
DCTN1-p150 Ri
J
3xmCh-Atg8a perinuclearity
1.0
0.5
0.0
-0.5
-1.0
****
**
luciferase Ri
Khc Ri
Klc Ri
K
3xmCh-Atg8a dot size (pixel²)
80
60
40
20
0
**
*
***
**
***
luciferase Ri
Dhc64C Ri
sw Ri
Dlic Ri
robl Ri
DCTN1-p150 Ri
L
3xmCh-Atg8a dot size (pixel²)
200
100
0
***
luciferase Ri
Shot Ri
Khc Ri
Klc Ri

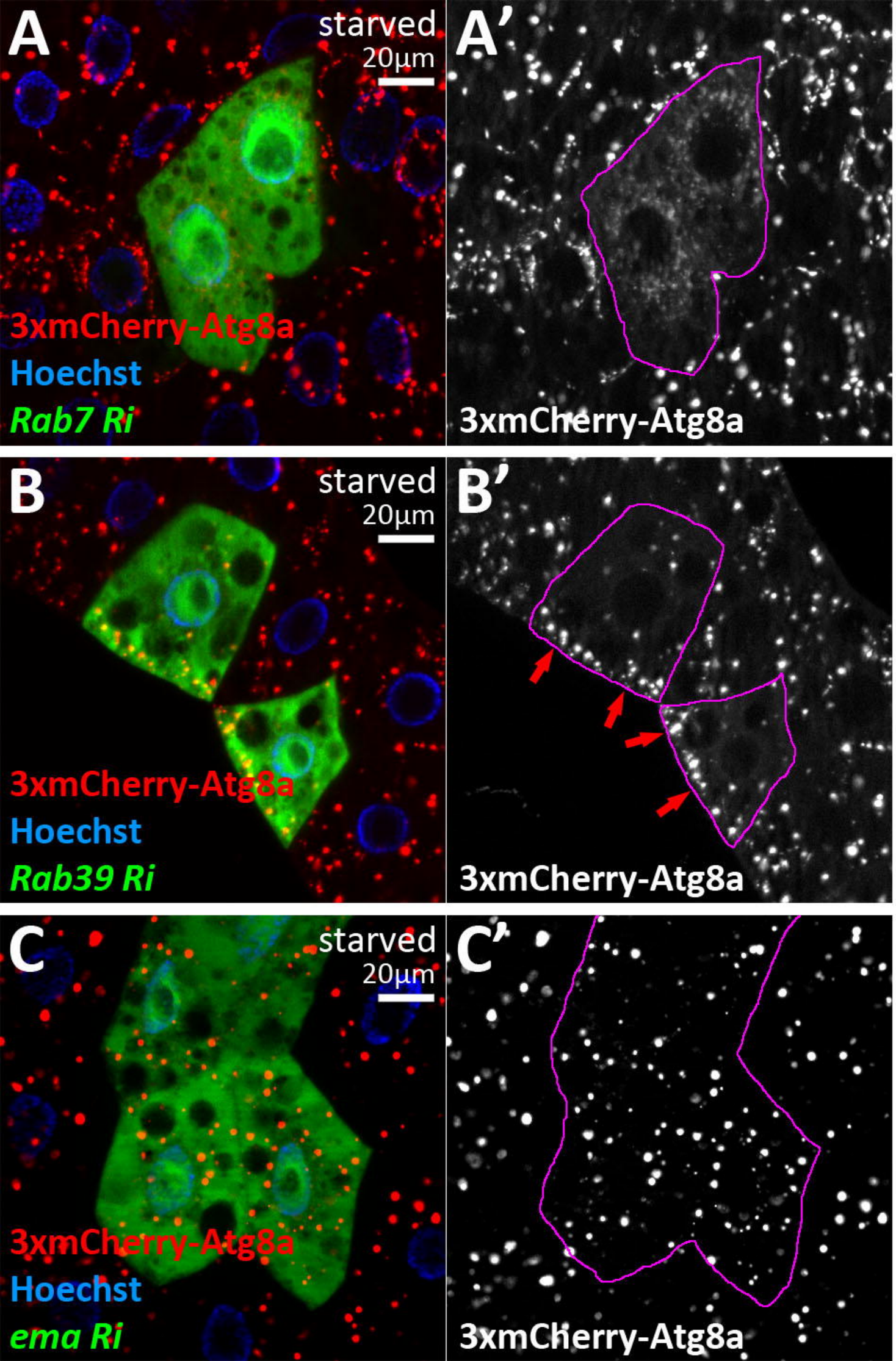
A
starved
20µm
3xmCherry-Atg8a
Hoechst
Rab7 Ri
A'
3xmCherry-Atg8a
B
starved
20µm
3xmCherry-Atg8a
Hoechst
Rab39 Ri
B'
3xmCherry-Atg8a
C
starved
20µm
3xmCherry-Atg8a
Hoechst
ema Ri
C'
3xmCherry-Atg8a

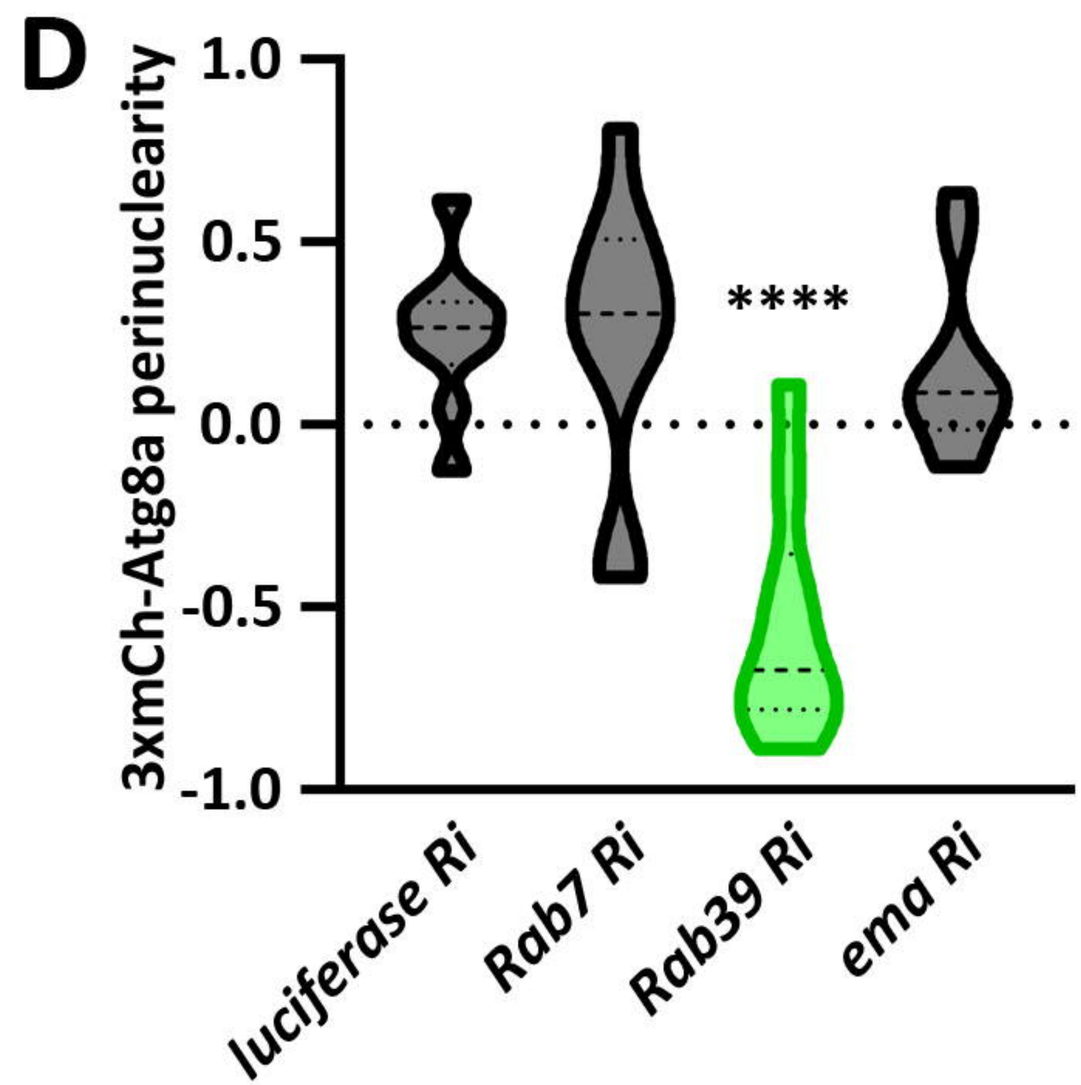
D
3xmCh-Atg8a perinuclearity
1.0
0.5
0.0
-0.5
-1.0
****
luciferase Ri
Rab7 Ri
Rab39 Ri
ema Ri

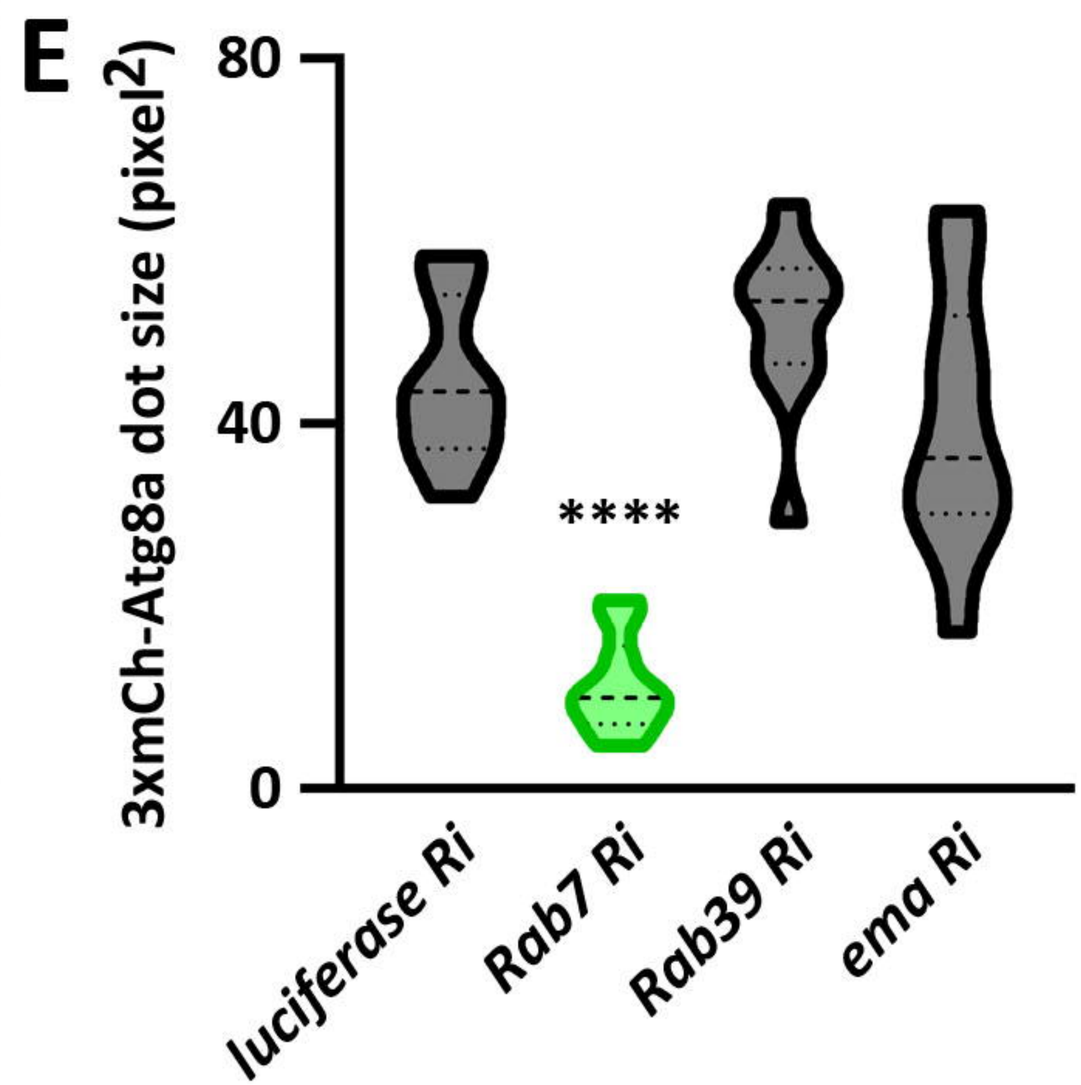
E
3xmCh-Atg8a dot size (pixel²)
80
40
0
****
luciferase Ri
Rab7 Ri
Rab39 Ri
ema Ri

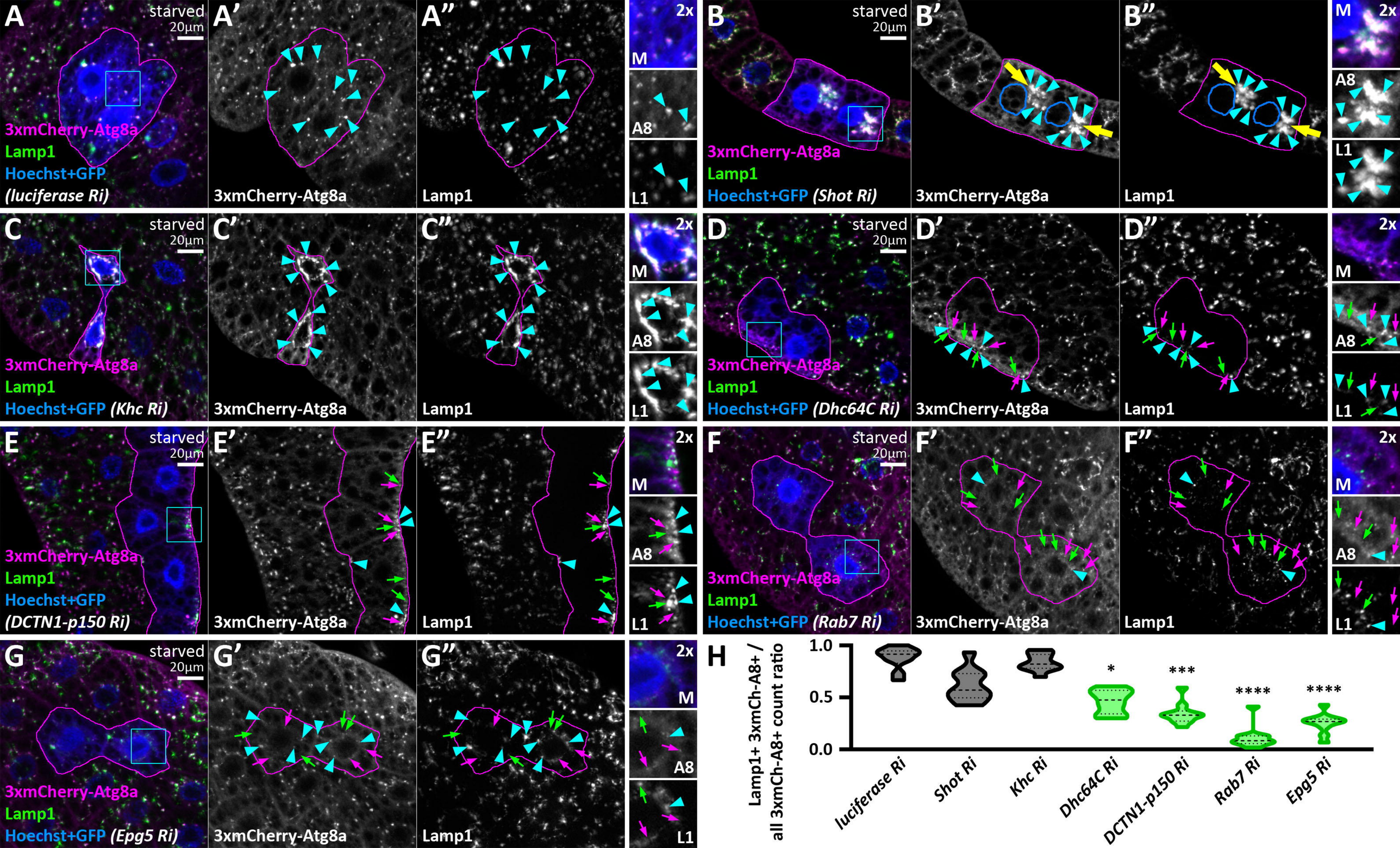
A
starved
20µm
3xmCherry-Atg8a
Lamp1
Hoechst+GFP
(luciferase Ri)
A'
3xmCherry-Atg8a
A''
Lamp1
2x
M
A8
L1
B
starved
20µm
3xmCherry-Atg8a
Lamp1
Hoechst+GFP (Shot Ri)
B'
3xmCherry-Atg8a
B''
Lamp1
C
starved
20µm
3xmCherry-Atg8a
Lamp1
Hoechst+GFP (Khc Ri)
C'
3xmCherry-Atg8a
C''
Lamp1
D
starved
20µm
3xmCherry-Atg8a
Lamp1
Hoechst+GFP (Dhc64C Ri)
D'
3xmCherry-Atg8a
D''
Lamp1
E
starved
20µm
3xmCherry-Atg8a
Lamp1
Hoechst+GFP
(DCTN1-p150 Ri)
E'
3xmCherry-Atg8a
E''
Lamp1
F
starved
20µm
3xmCherry-Atg8a
Lamp1
Hoechst+GFP (Rab7 Ri)
F'
3xmCherry-Atg8a
F''
Lamp1
G
starved
20µm
3xmCherry-Atg8a
Lamp1
Hoechst+GFP (Epg5 Ri)
G'
3xmCherry-Atg8a
G''
Lamp1
H
Lamp1+ 3xmCh-A8+ / all 3xmCh-A8+ count ratio
1.0
0.5
0.0
*
***
****
****
luciferase Ri
Shot Ri
Khc Ri
Dhc64C Ri
DCTN1-p150 Ri
Rab7 Ri
Epg5 Ri

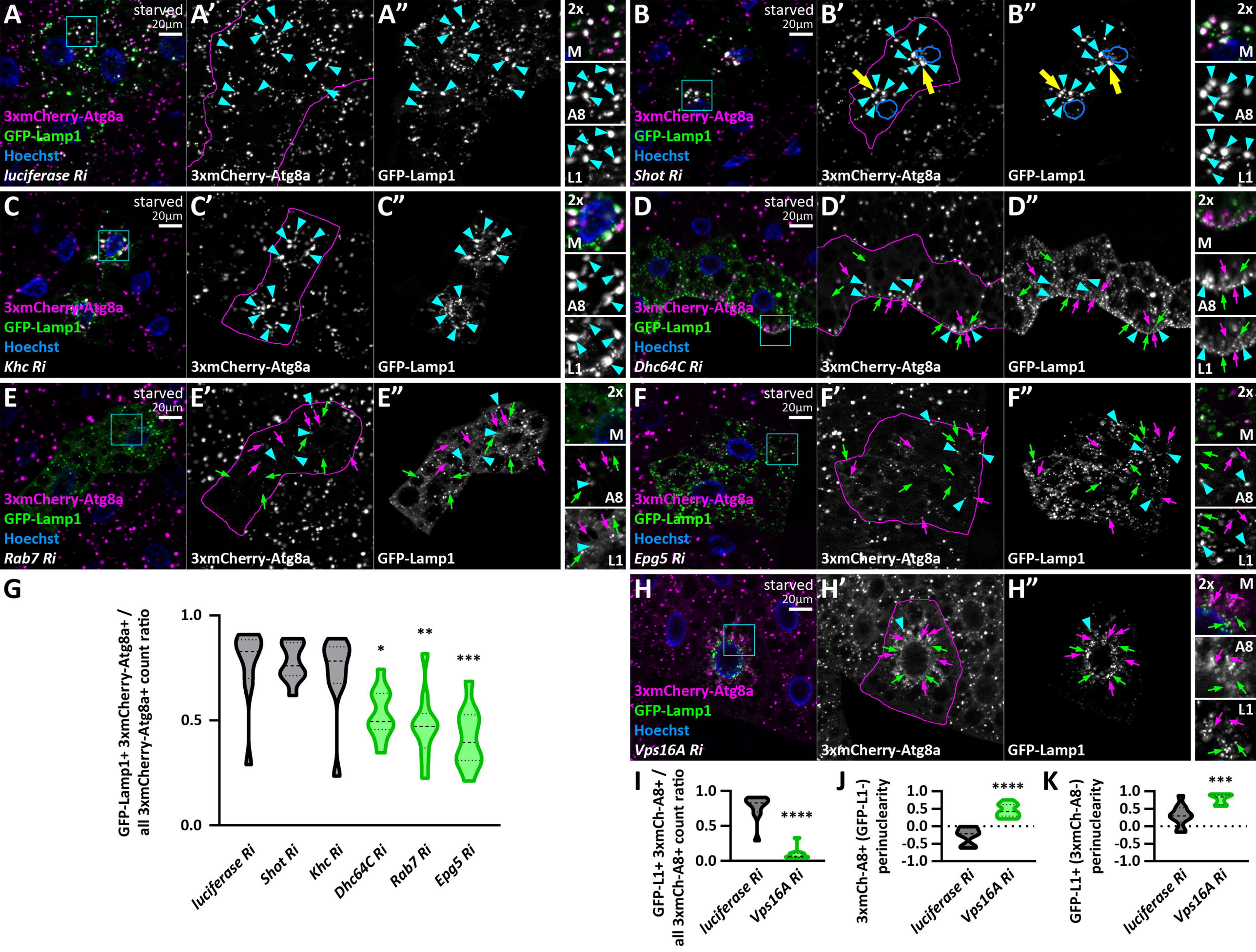
A
starved
20µm
3xmCherry-Atg8a
GFP-Lamp1
Hoechst
luciferase Ri
A'
3xmCherry-Atg8a
A''
GFP-Lamp1
2x
M
A8
L1
B
starved
20µm
3xmCherry-Atg8a
GFP-Lamp1
Hoechst
Shot Ri
B'
3xmCherry-Atg8a
B''
GFP-Lamp1
C
starved
20µm
3xmCherry-Atg8a
GFP-Lamp1
Hoechst
Khc Ri
C'
3xmCherry-Atg8a
C''
GFP-Lamp1
D
starved
20µm
3xmCherry-Atg8a
GFP-Lamp1
Hoechst
Dhc64C Ri
D'
3xmCherry-Atg8a
D''
GFP-Lamp1
E
starved
20µm
3xmCherry-Atg8a
GFP-Lamp1
Hoechst
Rab7 Ri
E'
3xmCherry-Atg8a
E''
GFP-Lamp1
F
starved
20µm
3xmCherry-Atg8a
GFP-Lamp1
Hoechst
Epg5 Ri
F'
3xmCherry-Atg8a
F''
GFP-Lamp1
G
GFP-Lamp1+ 3xmCherry-Atg8a+ / all 3xmCherry-Atg8a+ count ratio
1.0
0.5
0.0
*
**
***
luciferase Ri
Shot Ri
Khc Ri
Dhc64C Ri
Rab7 Ri
Epg5 Ri
H
starved
20µm
3xmCherry-Atg8a
GFP-Lamp1
Hoechst
Vps16A Ri
H'
3xmCherry-Atg8a
H''
GFP-Lamp1
I
GFP-L1+ 3xmCh-A8+ / all 3xmCh-A8+ count ratio
1.0
0.5
0.0
****
luciferase Ri
Vps16A Ri
J
3xmCh-A8+ (GFP-L1-) perinuclearity
1.0
0.5
0.0
-0.5
-1.0
****
luciferase Ri
Vps16A Ri
K
GFP-L1+ (3xmCh-A8-) perinuclearity
1.0
0.5
0.0
-0.5
-1.0
***
luciferase Ri
Vps16A Ri

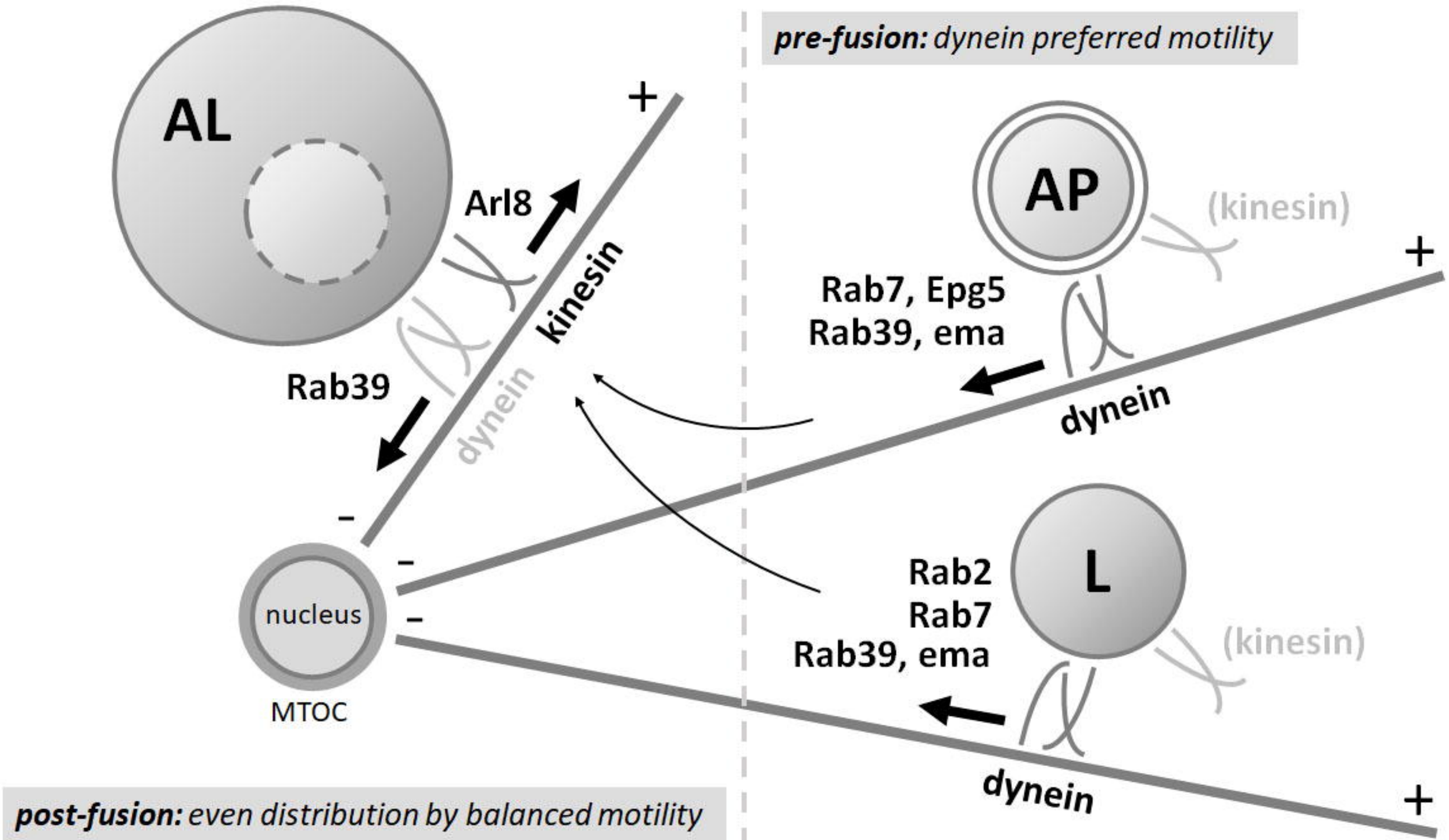
pre-fusion: dynein preferred motility
AL
Arl8
kinesin
dynein
Rab39
+
–
–
–
nucleus
MTOC
AP
(kinesin)
Rab7, Epg5
Rab39, ema
dynein
+
Rab2
Rab7
Rab39, ema
L
(kinesin)
dynein
+
post-fusion: even distribution by balanced motility